ABSTRACT

EXPERIMENTS AND MODELING OF THE CHEMO-MECHANICALLY COUPLED BEHAVIOR OF POLYMERIC GELS

by
Nikola Bosnjak

Polymeric materials consist of mutually entangled or chemically crosslinked long molecular chains which form a polymer network. Due to their molecular structure, the polymeric materials are known to undergo large deformation in response to various environmental stimuli, such as temperature, chemical potential and light.

When a polymer network is exposed to a suitable chemical solvent, the solvent molecules are able to diffuse inside the network, causing it to undergo a large volumetric deformation, known as swelling. In addition to volumetric deformation, this process involves the chemical mixing of the polymer network and solvent molecules, and is typically environmentally responsive. A polymeric material in this mixed and swollen state is known as a polymeric gel.

Swollen polymers, or polymeric gels, find their application in the oil industry, soft robotics, drug delivery and microfluidic channels. Moreover, most of the organs inside our body are gel-like in structure, which makes this class of materials important for biomedical applications and tissue engineering.

An important distinction between biological tissues and much of the previous literature on the mechanics of polymeric gels is that most biological tissues contain fibers. The existence of these fibers embedded in the material, causes the properties to be significantly different along the fiber direction.

Recent years have seen the development of a vast number of large deformation continuum-level constitutive models aimed to capture the coupled diffusion-deformation behavior of polymeric gels. However, there is an insufficient amount of experimental data to complement such theoretical research. Thus, despite numerous

potential applications, many aspects of polymeric gel behavior remain elusive. In addition, the diffusion-deformation behavior is known to be affected by the external stimuli. In the current state of the art there is a lack of theoretical models and robust simulation capabilities to account for the influence of such stimuli, hindering further advances in technologies involving polymeric gels.

The purpose of this research is to bridge the gap between the experimental and theoretical studies, and provide reliable finite element simulation capabilities for polymeric gels. More specifically, the aim is to (i) experimentally characterize the behavior of polymeric gels, (ii) develop new experimentally motivated constitutive models and (iii) implement the models numerically for use in a finite element software. The final result of this research is a robust finite element method (FEM) code that can be used for simulations in the commercial software package Abaqus.

Towards the goal, an experimental procedure is designed to thoroughly investigate the behavior of polymeric gels, and provide a direction for the development of novel constitutive models. The procedure involves mechanical testing of dry polymeric material, free swelling with suitable solvents, and mechanical testing when fully swollen. The experimental observations provide transformational insights in the mechanical behavior of polymeric gels, and are utilized to develop a continuum-level constitutive model.

Further, the presence of embedded fibers in a swellable polymer matrix leads to anisotropy in the overall behavior. In order to capture this response, a constitutive model for fiber-reinforced polymeric gels is developed, that explicitly takes into account anisotropy in both the mechanical and diffusive behavior. The constitutive model is implemented as user element subroutine (UEL) in the commercial finite element software package Abaqus/Standard. Numerical simulations are performed to show the behavior of the model, and qualitative comparisons are made to experiments of a soft robotic gripper.

In addition, many polymeric gels are known to respond or activate when exposed to a light stimulus. This light-driven alteration of the behavior is known to be caused by the photochemical reactions occurring inside the polymer network. Thus, the overall response of light-activated polymeric gels is affected by the mechanical stress, solvent content, and the extent of photochemical reaction caused by light irradiation. To account for such response of a polymeric gel, a continuum level constitutive model is developed and numerically implemented in Abaqus/Standard as a user element (UEL) subroutine.

EXPERIMENTS AND MODELING OF THE CHEMO-MECHANICALLY COUPLED BEHAVIOR OF POLYMERIC GELS

by
Nikola Bosnjak

A Dissertation
Submitted to the Faculty of
New Jersey Institute of Technology
in Partial Fulfillment of the Requirements for the Degree of
Doctor of Philosophy in Mechanical Engineering

Department of Mechanical Engineering

December 2020

APPROVAL PAGE

EXPERIMENTS AND MODELING OF THE CHEMO-MECHANICALLY COUPLED BEHAVIOR OF POLYMERIC GELS

Nikola Bosnjak

Shawn A. Chester, Dissertation Advisor — Date
Associate Professor of Mechanical Engineering, New Jersey Institute of Technology

---

Pushpendra Singh, Committee Member — Date
Professor of Mechanical Engineering, New Jersey Institute of Technology

---

Siva Nadimpalli, Committee Member — Date
Associate Professor of Mechanical Engineering, Michigan State University

---

James Hanson, Committee Member — Date
Professor of Chemistry and Biochemistry, Seton Hall University, NJ

Brittany Froese Hamfeldt, Committee Member — Date
Assistant Professor of Mathematical Sciences, New Jersey Institute of Technology

---

Howon Lee, Committee Member — Date
Assistant Professor of Mechanical Engineering, Rutgers University - New Brunswick, NJ

BIOGRAPHICAL SKETCH

Author: Nikola Bosnjak

Degree: Doctor of Philosophy

Date: December 2020

Undergraduate and Graduate Education:

- Doctor of Philosophy in Mechanical Engineering
  New Jersey Institute of Technology, Newark, NJ, 2020
- Master of Science in Mechanical Engineering
  University of Belgrade, Belgrade, Serbia, 2015
- Bachelor of Science in Mechanical Engineering
  University of Belgrade, Belgrade, Serbia, 2013

Major: Mechanical Engineering

Presentations and Publications:

Nikola Bosnjak, Siva Nadimpalli, Dai Okumura and Shawn A. Chester, "Experiments and modeling the viscoelastic behavior of polymeric gels," *Journal of the Mechanics and Physics of Solids*, 137, 103829, 2020.

Nikola Bosnjak, Shuolun Wang, Daehoon Han, Howon Lee and Shawn A. Chester, "Modeling of fiber-reinforced polymeric gels," *Mechanics Research Communications*, 96, 7-18, 2019.

Chen Yang, Jeffrey Luo, Marianne Polunas, Nikola Bosnjak, Sy-Tsong Dean Chueng, Michelle Chadwick, Hatem E. Sabaawy, Shawn A. Chester, Ki-Bum Lee and Howon Lee, "4D printed transformable tube array for high-throughput 3D cell culture and histology," *Submitted to Advanced Materials.*

Nikola Bosnjak and Shawn A. Chester, "Photochemical effects on viscoleastic behavior of polymeric gels," *In preparation.*

Nikola Bosnjak and Shawn A. Chester, "Experiments and modeling of viscoelasticity in polymeric gels," *Invited talk,* ASM International, Chapter NY/NJ, USA, 2020.

Nikola Bosnjak, Shuolun Wang, Daehoon Han, Howon Lee and Shawn A. Chester, "Modeling of fiber-reinforced polymeric gels," *Oral presentation,* American Society of Mechanical Engineers (ASME) International Mechanical Engineering Congress and Exposition, Salt Lake City, UT, USA, 2019.

Nikola Bosnjak and Shawn A. Chester, "Modeling of light-activated polymeric gels," *Oral presentation,* American Society of Mechanical Engineers (ASME) International Mechanical Engineering Congress and Exposition, Salt Lake City, UT, USA, 2019.

Nikola Bosnjak, Justin Newkirk and Shawn A. Chester, " Experiments and modeling the viscoelastic behavior of polymeric gels," *Oral presentation,* The 56th Annual Technical Meeting of the Society of Engineering Science (SES), St. Louis, MO, USA, 2019.

Nikola Bosnjak, Shuolun Wang, Daehoon Han, Howon Lee and Shawn A. Chester, "Modeling of fiber-reinforced polymeric gels," *Oral presentation,* The 56th Annual Technical Meeting of the Society of Engineering Science (SES), St. Louis, MO, USA, 2019.

Nikola Bosnjak and Shawn A. Chester, "New insights on the viscoelastic behavior of polymeric gels," *Oral presentation,* American Society of Mechanical Engineers (ASME) International Mechanical Engineering Congress and Exposition, Pittsburgh, PA, USA, 2018.

Nikola Bosnjak and Shawn A. Chester, "Modeling of fiber-reinforced polymeric gels," *Oral presentation,* American Society of Mechanical Engineers (ASME) International Mechanical Engineering Congress and Exposition, Pittsburgh, PA, USA, 2018.

Nikola Bosnjak and Shawn A. Chester, "Integrated modeling and experiments of viscoelastic gels,
Oral presentation, The 55th Annual Technical Meeting of the Society of Engineering Science (SES), Madrid, Spain, 2018.

Nikola Bosnjak and Shawn A. Chester, "Integrated modeling and experiments of viscoelastic polymeric gels," *Oral presentation,* European Mechanics of Materials Conference, Nantes, France, 2018.

Nikola Bosnjak and Shawn A. Chester, "Experiments and modeling of polymeric gels," *Oral presentation,* American Society of Mechanical Engineers (ASME) International Mechanical Engineering Congress and Exposition, Tampa, FL, USA, 2017.

Nikola Bosnjak and Shawn A. Chester, "Experiments and modeling of polymeric gels," *Oral presentation* The 54th Annual Technical Meeting of the Society of Engineering Science (SES), Boston, MA, USA, 2017.

Nikola Bosnjak and Shawn A. Chester, "Experiments and modeling of polymeric gels," *Oral presentation,* American Society of Mechanical Engineers (ASME) International Mechanical Engineering Congress and Exposition, Phoenix, AZ, USA, 2016.

Nikola Bosnjak and Shawn A. Chester, "Mechanical characterization of polymeric gels," *Oral presentation,* The 53rd Annual Technical Meeting of the Society of Engineering Science (SES), College Park, MD, USA, 2016.

To my family and friends

ACKNOWLEDGMENT

I would like to take this opportunity to express my gratitude to the people without whose help my research would not be possible. First of all, I would like to thank my advisor, Dr. Shawn Chester for his mentorship and for sharing his knowledge in various aspects of mechanics of materials. He encouraged me to independently analyze and solve problems, while always being there to ensure I am on the right path. Equally important, I learned plenty from his work and professional ethics, which I am aspiring to adopt.

I would also like to thank Dr. Siva Nadimpalli for allowing me to use his laboratory facilities, but more importantly, for sharing his vast knowledge of experimental testing of materials, and Dr. Veljko Samardzic, whose advice set me off on this journey. Further, I would like to thank the thesis committee members, Dr. Howon Lee, Dr. James Hanson, Dr. Brittany Froese Hamfeldt and Dr. Pushpendra Singh for their advice and numerous conversations which enhanced my research. Additionally, I would like to express my appreciation to the National Science Foundation for providing the funding for my PhD research (under grant numbers CMMI-1463121 and CMMI-1751520).

Finally, I would like to thank my lab mates: Shuolun Wang, Patrick Thompson, Suman Jaiswal and Keven Alkhoury for a productive and exciting work environment. I would particularly like to thank Shuolun for his valuable input and help in my initial research and great discussions. In addition, many thanks to Rajasekhar Tripuraneni, Subhajit Rakshit, Akshay Pakhare and Igor Bezsonov for great conversations and friendship.

TABLE OF CONTENTS

TABLE OF CONTENTS
(Continued)

Chapter **Page**

TABLE OF CONTENTS
(Continued)

Chapter **Page**

TABLE OF CONTENTS
(Continued)

Chapter **Page**

LIST OF TABLES

LIST OF FIGURES

LIST OF FIGURES
(Continued)

Figure **Page**

LIST OF FIGURES
(Continued)

Figure **Page**

LIST OF FIGURES
(Continued)

Figure **Page**

LIST OF FIGURES
(Continued)

Figure **Page**

CHAPTER 1

INTRODUCTION

1.1 Background

Solid polymers and polymeric materials consist of underlying polymeric network composed of long entangled molecular chains mutually connected with crosslinks or non-permanent bonds. When brought in contact with a suitable solvent, the network will absorb the solvent and swell. The mixing of the solvent and polymer network constitutes what is known as a polymeric gel, and the volume change due to swelling may be on the order of hundreds of percent. The amount of solvent imbibed due to mixing and swelling, along with environmental conditions, lead to significant changes in the volume and mechanical properties of gels compared to the dry network.

Numerous important industrial applications and scientific merits exist in studying the coupled deformation-diffusion behavior of polymeric gels. As an example, in the oil industry, swellable rubber materials are vulcanized onto drill pipes to serve as what is known as *packers*. These packers, when in contact with oil (or water), imbibe the oil (or water) to form a swollen gel which is used to seal different segments of a well bore [76]. Additionally, in biomedicine, the demand for more controlled drug delivery systems is increasing, and various types of gels are used for that purpose [63, 128]. Due to the similarity of gels with biological materials, polymeric gels are extensively used in tissue engineering (cf., e.g., [114, 91, 85, 80]). Further, many polymeric gels are biocompatible and biodegradable, making them highly suitable for drug delivery applications (cf., e.g., [28, 145]) and medical implants [139]). Lastly, one of the most popular applications of polymeric gels is in microfluidic channels as actuators and sensors [7, 101].

Also, many polymers respond to environmental stimuli such as temperature, electric and magnetic fields, pH, and more [53, 52, 46, 116, 66, 82]. The responsiveness of polymeric gels to environmental stimuli has been widely employed in soft robotics [103, 136]. The applications of soft robots are vast [65], the more exotic ones include morphing airfoils, rotary actuators, and grippers [140, 48, 10]. Newly designed polymeric gels are being developed to enhance the performance of these systems [147]. Further, the flexibility of soft robots and their similarity to biological systems are utilized in bio-hybrid robotics [12]. The fast emerging development of gel-based soft robots makes modeling of this class of materials an important task for simulating their operation.

Historically, first important breakthrough in the research of polymeric gels was made in the middle of 20th century. During the 1940's, polymer chemist Paul Flory and his research group laid a foundation for modern understanding of polymeric gels. From current scientific perspective, two most notable products of their research are Flory-Huggins model [42], and Flory-Rehner theory [45]. Flory-Huggins model provides the statistical model for migration of fluid molecules inside a polymer network. Moreover, most of the current models for polymer swelling are based on Flory-Rehner equilibrium swelling theory. The importance of this theory lies in a fact that this is the first attempt to combine mechanical Neo-Hookean model with chemical mixing.

Later on in the 1970's, Tanaka et al. [126] proposed their theory for kinetics of polymeric gels. In addition, they obtained one of the first experimental data for polymeric gels. This is commonly considered as a starting point for most of modern-day research. Recent years saw an extensive number of multiphysics continuum-level gel theories for the coupled diffusion-deformation behavior being developed (cf., e.g., [58, 35, 29, 16, 34, 90, 19]).

Alongside the theoretical research, various experimental procedures have been developed to capture the mechanical behavior of gels, some of which include indentation [62], microscale tensile testing [67] and compression testing [37, 70]. Most of the above mentioned experimental procedures involve a small-scale deformation of the material. In addition, large deformation testing of gels is conducted by [113], [135], and [141]. Although the incorporation of large deformations is common in many modeling and computational studies, the insufficient amount of relevant experimental data is impeding research that would push our knowledge further.

1.2 Introduction to Viscoelastic Polymeric Gels

A vast number of polymeric materials exhibit a non-linear viscoelastic behavior. Viscoelasticity in polymeric materials is commonly considered to arise due to the difference in time scale between rapid short-range motion and slower long-range motion of polymeric chains, as well as the interaction between the chains [39]. Being such a well known phenomena, the viscoelastic behavior of polymeric materials has been thoroughly researched over the past decades. Mechanical testing of viscoelastic polymers was performed by [122], [105] and [59]. Moreover, there have been many notable attempts to model the time-dependent behavior of viscoelastic polymers. Some of the initial work on modeling viscoelasticity in polymers was done by [49] and [8], followed by the models developed by [130] and [23]. More recent constitutive models are the work of [32], [111], [68], [33], [93] and [83].

The behavior of viscoelastic polymers is known to be affected by different environmental conditions, such as temperature, voltage, and chemical potential. Experimental data on temperature dependent viscoelastic behavior was published as early as mid 1950s (cf., e.g., [138, 107, 108]) with some more recent observations by [73] and [31]. The vast amount of experimental research is accompanied by constitutive models to capture that behavior [110, 74, 31, 99]. In addition to

studies on the electro-elasticity (cf., e.g.,[30, 20]), the coupled electro-mechanical behavior of viscoelastic polymers has been shown and modeled in the literature [131, 142, 60, 133]. The coupled chemo-mechanical behavior of viscoelastic polymers has also been studied in recent years. In the current literature on viscoelastic gels, one can find the experimental research by numerous groups [146, 12, 94, 72]. Further, continuum-level constitutive models for viscoelastic gels, which take into account the chemo-mechanical behavior have been developed [61, 15]. Nonetheless, the current state of the literature lacks sufficient quantity of data and observations to corroborate and calibrate the vast number of models.

It is also worth noting that recent years saw an extensive number of studies, both experimental and theoretical, involving poroelasticity (cf., e.g., [47, 134, 62, 61]). While these studies have provided an insight in the coupled diffusion-deformation behavior at smaller deformations, the response of polymeric gels undergoing large deformations is yet to be fully characterized and modeled.

1.3 Introduction to Fiber-Reinforced Polymeric Gels

An important distinction between biological tissues and much of the previous literature on the mechanics of polymeric gels is that most biological tissues contain fibers. The existence of these fibers embedded in the material, causes the properties to be significantly different along the fiber direction [137, 97, 22, 106, 21]. In other words, the presence of embedded fibers imposes pronounced anisotropy in the response of these materials.

In the literature, one also finds a vast number of constitutive models for capturing anisotropic behavior of fiber-reinforced polymers (cf., e.g., [57, 11, 98, 2]). However, there are only a few notable attempts to include influence of embedded fibers on behavior of polymeric gels in recent years (cf., e.g., [104, 95, 96]).

1.4 Introduction to Photo-Sensitive Polymeric Gels

The photo-activation of polymeric gels is typically achieved through tethering of photo-sensitive groups onto the polymeric backbone. The two most commonly employed photo-sensitive groups are azobenzene and spirobenzopyran chromophores (cf., e.g., [41, 132]). When irradiated, azobenzene undergoes *trans-cis* photoisomerization, while the spirobenzopyran undergoes photoisomerization from a hydrophilic open ring to a hydrophobic closed ring. Both of these processes are reversible and are known to affect the amount of swelling of polymeric gels ([118, 24]). More recently, the photo-induced addition-fragmentation chain transfer (AFCT) was utilized to alter the mechanical properties of polymeric gel. In their study, [92] have shown the AFCT has a significant impact on the viscoelastic behavior of polymeric gel.

In current literature one finds experimental studies aimed to characterize the influence of irradiation on the response of polymeric materials and gels. The influence of photo-induced bond formation in polymeric network has been widely studied (cf., e.g., [102, 54, 4, 6, 38]), as well as the photo-degradation due to bond cleavage (cf., e.g., [120, 112, 143]). Also, the influence of irradiation on swelling kinetics in polymeric gels has been well documented (cf., e.g., [69, 84, 77]), and the data by [24] suggests the reversibility of the process.

While photo-induced bond formation/cleavage and swelling kinetics have been extensively investigated, some experimental studies suggest the effects of irradiation go beyond the degree of swelling. The recent study by [92] suggests the viscoelastic response of polymeric gel is affected by irradiation. Their experimental data (discussed in further detail in Section 4.2) shows a noticeable increase in the loss modulus while the gel is irradiated, returning to its baseline once the irradiation is stopped.

In addition to experimental work, recent years have seen the notable attempts to model the response of photo-sensitive gels (cf., e.g., [78, 127, 27, 14]). While

most of the modeling studies focus on capturing the swelling kinetics, the change in viscoelastic response due to irradiation is yet to be accounted for.

CHAPTER 2

VISCOELASTIC POLYMERIC GELS

2.1 Introduction

The work presented in this chapter is aimed to characterize the viscoelastic response of both dry and fully swollen polymeric gels through experimental observations and continuum level modeling. Towards our goal, we have developed an experimental procedure intended to capture the major aspects of the non-linear mechanical behavior of polymeric gels, including the viscoelastic response. To complement the experimental observations, we calibrate a constitutive model for viscoelastic polymeric gels. In what follows, we restrict our attention to the specific cases where the material is either completely dry, or fully swollen.

For our experiments we have chosen the commercially available material VHB 4910, since it is well known exhibit viscoelastic behavior in the absence of fluid [59, 133]. Also, we have observed that VHB 4910 swells when in contact with suitable solvents. Therefore, all of our experiments make use of n-Pentane, o-Xylene, and Toluene, as solvents in conjunction with VHB 4910 to create our polymeric gels. The continuum-level constitutive model is mechanically incompressible, includes viscoelasticity, and does not explicitly take diffusion into account. That is to say we consider time dependence in the mechanical response, however, not in the diffusive response of the solvent, which is taken to be at a known and fixed degree of swelling.

The remainder of this chapter is organized as follows, in Section 2.2 we overview some of the terminology and important details involved with mechanical testing of swollen polymeric gels. In Section 2.3 we present our experimental procedures, as well as analysis procedures for our measurements, and the corresponding results. In Section 2.4, we present the constitutive model used to interpret the experimental

results and the model is calibrated in Section 2.5. Lastly, Section 2.6 provides some concluding remarks.

2.2 Preliminaries

It is worthwhile to make clear our assumptions used for mechanical testing polymeric gels. First, for clarification, the nomenclature that will be used throughout is:

- Virgin — A dry sample, without any previous history of solvent exposure, or mechanical loading, is considered *virgin*.
- Fully swollen — A virgin sample, exposed to ample solvent, free of mechanical constraints, and allowed to swell until equilibrium, is considered *fully swollen*. This process is termed *free swelling*.
- Solvent cycled — A virgin sample, first fully swollen, and then completely dried (deswollen), is considered *solvent cycled*. The process of swelling following by drying may be repeated numerous times. For example, a sample could be solvent cycled five times, that indicates a virgin sample was fully swollen and then freely dried five times.

When mechanically testing unswollen samples (either virgin or solvent cycled), in a uniaxial setting the total deformation that polymer network undergoes is the mechanical stretch λ^m. On the other hand, exposing that polymer network to an ample quantity of a suitable solvent for long enough time, in the absence of mechanical constraints or loading, will cause it to freely swell to equilibrium. The process of free swelling yields an isotropic volumetric expansion, and on a continuum level, a stress-free state — what we call fully swollen. The stretch caused by swelling is denoted by λ^s, assumed to be spherical, and when freely swollen λ^s is homogeneous inside a gel.[1] For our experiments on freely swollen gels, we consider the initial

[1]In general, in the presence of mechanical or chemical constraints, λ^s need not be homogeneous inside a polymeric gel.

configuration for mechanical testing the freely swollen state, with a prior homogeneous swelling stretch λ^s. Uniaxial mechanical testing on the freely swollen polymer gels is achieved by displacement controlled deformation applied on the initially freely swollen material. This is shown schematically in Figure 2.1. Further, as is common in the literature on the mechanics of gels, we employ a multiplicative decomposition of the total uniaxial stretch, making the total deformation of the swollen polymer gel

$$\lambda = \lambda^m \lambda^s \,. \tag{2.1}$$

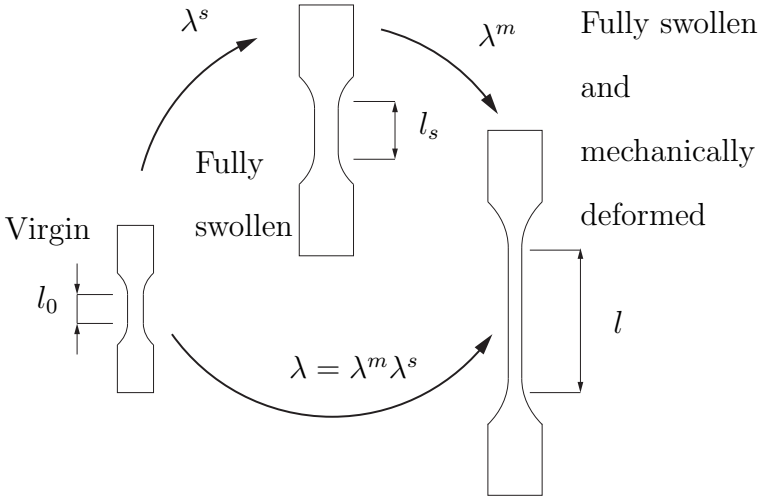

Figure 2.1 Schematic of the multiplicative decomposition of the total uniaxial stretch into swelling and mechanical contributions.

Going further into the details, in reference with Figure 2.1, the total uniaxial stretch is defined as

$$\lambda = \frac{l}{l_0} \tag{2.2}$$

where l is the deformed gauge length and l_0 is the virgin gauge length. The swelling stretch represents the ratio of the swollen length to virgin length

$$\lambda^s = \frac{l_s}{l_0} \,, \tag{2.3}$$

where l_s is the length of swollen material. Following Figure 2.1 and relation (2.1), the mechanical stretch is the ratio of the mechanically deformed length to the freely swollen length, which can be written in the form

$$\lambda^m = \frac{l}{l^s} = \frac{l^s + u^m}{l^s} = 1 + \frac{u^m}{l^s}\,, \tag{2.4}$$

where u^m is the axial displacement caused by mechanical deformation. In the case of dry material without any swelling, we simply have $\lambda^s = 1$, and therefore $\lambda = \lambda^m$.

Since we are interested in assessing the rate-dependent behavior of polymeric gels, the rate of deformation is essential. To make the analysis as useful as possible, we use the mechanical stretch rate

$$\dot{\lambda}^m = \frac{\dot{u}^m}{l^s}\,, \tag{2.5}$$

and the total stretch rate at a fixed amount of swelling

$$\dot{\lambda} = \frac{\dot{u}^m}{l_0} = \dot{\lambda}^m \lambda^s\,. \tag{2.6}$$

The standard nominal (1st Piola) stress in uniaxial tension for dry material is given by

$$P = \frac{F}{A_0} \tag{2.7}$$

where F is the force signal obtained by the load cell, and A_0 is the dry nominal cross sectional area. Care must be taken in the choice of a stress measure used for fully swollen uniaxial tests. Prior to any mechanical loading, since the sample is fully swollen, but mechanically undeformed we have $\lambda^m = 1$ and $\lambda^s > 1$, leading to an initial stretch $\lambda = \lambda^s > 1$ prior to the application of any prescribed mechanical deformation. Therefore, we will also report on the stress measured per freely swollen cross sectional area, a mechanical Piola stress. Here the mechanical Piola stress is

denoted by

$$P^m = \frac{F}{A^s}\,, \tag{2.8}$$

where A^s is the nominal cross sectional area of the fully swollen sample. Additionally, the Cauchy stress, or true stress, is the force per unit current cross sectional area. However since we are unable to measure the current cross sectional area during a test, and do not want to make unnecessary assumptions, we do not report it in this work.

Lastly, we will make frequent use of the stiffness in our analysis, which experimentally is taken simply as the slope of the uniaxial tension stress - stretch curve, measured at a specific deformation since it is not constant. Since our experiments are designed to obtain the material response at a fixed degree of swelling, we assume λ^s is a constant, therefore,

$$\frac{d(\bullet)}{d\lambda} = \frac{d(\bullet)}{d\lambda^m}\frac{d\lambda^m}{d\lambda} = \frac{d(\bullet)}{d\lambda^m}\left(\lambda^s\right)^{-1}\,. \tag{2.9}$$

Accordingly, we only report on stiffnesses measured relative to mechanical deformation in this work. Further, since the effective stiffness is what one would measure in the current deformed configuration, for dry and swollen samples the effective stiffness is

$$\frac{dP}{d\lambda^m}, \quad \text{and} \quad \frac{dP^m}{d\lambda^m}\,, \tag{2.10}$$

respectively. To experimentally measure the stiffness based on experimental data, we determine the slope of the stretch-stress curve at a specified stretch by fitting a line to five data points centered around the specified stretch.

2.3 Experimental Procedures and Results

In this section, we report our experimental procedures for capturing the non-linear viscoelastic behavior of virgin, fully swollen, and solvent cycled polymeric materials, as well as the corresponding results. Our experiments are performed on the popular

and widely known commercially available acrylic polymer VHB 4910. This material is chosen since virgin VHB is well known to exhibit highly viscoelastic non-linear behavior [59, 133].

The overall experimental scheme broadly consists of the following:

1. uniaxial tension, stress relaxation, and creep testing on virgin samples;
2. free swelling of virgin samples;
3. uniaxial tension and stress relaxation on fully swollen samples;
4. uniaxial tension and stress relaxation, on solvent cycled samples;

with more detail in what follows.

We commence the experimental procedure by determining the virgin baseline behavior of the polymer. To investigate the *time-independent* behavior of the virgin polymer, we perform a set of large deformation tensile tests, including load and unload, at a very slow mechanical stretch rate, accompanied by large deformation creep and stress relaxation testing. Next, to probe the *time-dependent* behavior of the virgin polymer we perform a set of tensile tests consisting of loading followed by unloading at various prescribed mechanical stretch rates. Further, to thoroughly probe the relaxation behavior of the virgin polymer, we perform a set of stress relaxation tests at a moderate prescribed stretch. After the uniaxial baseline data for the virgin polymer is obtained, we next move onto free swelling. To determine the swelling stretch caused by free swelling, VHB 4910 was immersed in three different solvents, n-Pentane, o-Xylene and Toluene, until equilibrium was reached, over 24 hours. The next step involves repeating some of the uniaxial tests mentioned before, but now on fully swollen samples. The procedure consists of a similar set of uniaxial tests as used for the dry virgin material, to investigate the time-independent, time-dependent, and relaxation behavior of fully swollen VHB 4910. Lastly, virgin

samples are freely swollen, followed by free drying of those same samples — what we have termed solvent cycled. Then, another similar set of uniaxial tests are performed again to determine if there is any measurable irreversible change to the mechanical behavior due to solvent cycling.

2.3.1 Experimental Setup

All tensile tests reported here are conducted on an MTS Criterion Model 43 uniaxial testing machine at a fixed room temperature of 24°C. We use dog-bone shaped specimens, and virgin samples are cut out from a roll of VHB 4910 tape using an ASTM D638-V cutting die. The nominal length, width, and thickness of the virgin gauge section are 9.49 mm, 3.18 mm, and 1 mm respectively. Importantly, since there are minute variations in the material, both thickness and width are measured prior to the start of all experiments. When dealing with very soft materials, the use of calipers or a micrometer can lead to false measurements due to the deformation of the material under the caliper jaws or micrometer anvils. Therefore, we use a non-contact measurement based on photos of dry and swollen specimens, and use ImageJ [109] software to measure the thickness and the width of gauge section. Our experience shows that this leads to the best dimensionally repeatable data we were able to obtain. All the photos used for dimensional measurements reported here were taken with a Nikon-D3200 camera mounted on a tripod for repeatability.

To measure the deformation in our tensile experiments, the non-contact Digital Image Correlation (DIC) software Vic2D (Correlated Solutions) is employed and integrated with a digital camera (PointGrey GRAS-50S5M-C). Due to compliance of the testing machine, slippage, or other factors, post-processing DIC measurements of the gauge section have been found the most reliable method to obtain deformation data in these soft materials. Additionally, our DIC data acquisition system allows for concurrent image capture and force signal measurement. Since VHB is transparent,

for virgin and solvent cycled samples, a number of black lines are applied to the gauge section with a permanent marker prior to testing to obtain color contrast for DIC measurements. However, the permanent marker was unreliable when applied to the surface of the fully swollen (wet) sample. Therefore, we applied fine black powder particles (silicon carbide grit, size 60) to the wet sample surface and they provide contrast for DIC.

To measure the force, a combination of a 5-pound load cell (Transducer Techniques MDB-5) and 100-gram load cell (Transducer Techniques GSO-100) are used depending on the expected load encountered. The choice is made to obtain the best signal-to-noise ratio for each particular experiment. For example, a dry virgin material at very large stretch requires the 5-pound load cell, however a fully swollen load-unload tension test to moderate stretch will not exceed 100 g, and therefore the smaller load cell is used.

When left in air for 10 minutes, samples fully swollen with solvent (n-Pentane, o-Xylene, or Toluene) on average lost 20.7 % of their mass through evaporation, compared to just 7.1 % when completely submerged in water. Therefore, to mitigate the evaporation of solvent from the swollen gel, the tensile tests on fully swollen gels are performed inside a fluid bath filled with water, that is mounted in the load train of the testing machine, as shown in Figure 2.2. We have found that immersion of the swollen gel in water significantly reduces the evaporation of the imbibed solvent, and is our best effort to ensure the solvent concentration is homogeneous inside the material.

In addition, the typical order of magnitude for solvent diffusivity in a polymeric gel is approximately $10^{-10}\,\mathrm{m}^2/\mathrm{s}$ (cf., e.g., [25, 55]), for a length scale of 1 mm, we estimate the characteristic diffusion time of about 2.75 hours. Since the majority of our experiments take place on a much shorter timescale, when analyzing the

experimental data we assume the solvent concentration is constant and uniform throughout for all of our mechanical tests.

It is important to note that, although the curvature of the fluid bath, along with the presence of water, somewhat distorts the images used for DIC in the transverse direction, it is not significant in the loading direction. A verification procedure is provided in the Appendix showing that the DIC measurements are acceptable with only minor error in this fluid bath setup. Therefore, we freely use DIC to measure the axial extension in our uniaxial experiments on submerged specimens.

Further, when performing a mechanical test on a sample submerged in a fluid bath, as in Figure 2.2, the data recorded by the load cell is affected by buoyancy. To ensure the best quality force data, we include the buoyancy of the submerged grip, load train, and sample, when processing the experimental results. To determine the effect of buoyancy, we hold a swollen sample inside the top grip, and directly measure the change in force at different submerged depths. The recorded force per depth (N/m) is used when analyzing the data, allowing for the inclusion of buoyancy in the analysis. Details of the buoyancy calibration are provided in the Appendix B.

2.3.2 Virgin Uniaxial Testing Procedure

First, the dimensions of the gauge section width and thickness of each sample are measured using ImageJ [109] as described previously. The quasi-static large deformation tensile tests are performed at a constant stretch rate of $\dot{\lambda} = \dot{\lambda}^m = 10^{-4}\,\mathrm{s}^{-1}$, based on the virgin gauge section dimensions. The crosshead displacement is prescribed to obtain a maximum stretch of $\lambda = \lambda^m = 10$ based on the virgin gauge length, followed by unloading to the initial stretch of $\lambda = 1$ to probe the large deformation behavior and hysteresis in the material response. Later, DIC analysis is performed as a post-processing step to obtain the actual deformation in the gauge section.

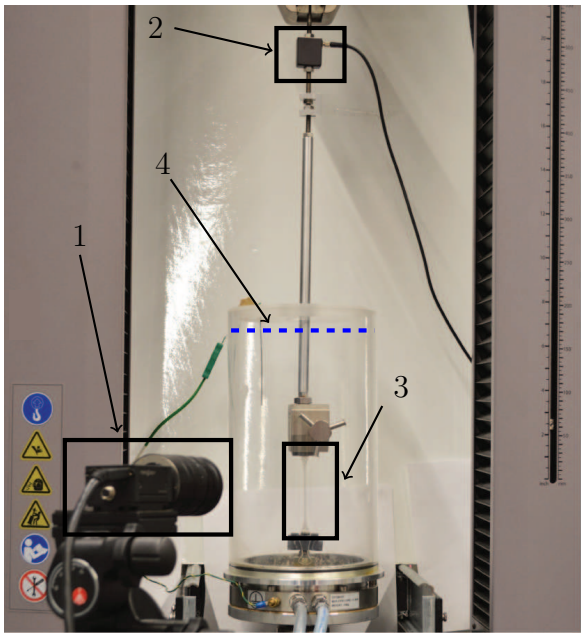

Figure 2.2 Experimental setup for mechanical testing of a sample inside a fluid bath. Here, 1 denotes the digital camera, 2 the (5-pound) load cell, 3 an extended fully swollen gel sample, and 4 the water level.

For load-unload tensile tests at moderate stretch rates, we prescribe the crosshead displacement to obtain a maximum stretch of $\lambda = \lambda^m = 2$, and the unloading displacement to return to the initial stretch of $\lambda = \lambda^m = 1$ at a constant stretch rate. To assess rate dependency, two different rates are used $\dot{\lambda} = \dot{\lambda}^m = 10^{-2}\,\mathrm{s}^{-1}$ and $10^{-1}\,\mathrm{s}^{-1}$, with the prescribed loading profiles shown in Figure 2.3.

Next, we perform a set of stress relaxation experiments. First, samples are loaded to a stretch $\lambda = \lambda^m = 2$, at a stretch rate of $\dot{\lambda} = \dot{\lambda}^m = 2 \times 10^{-1}\,\mathrm{s}^{-1}$, the fastest our screw driven testing machine can reliably move. After reaching the prescribed stretch, samples are then held at that fixed stretch for 1 hour, while the force is being recorded to determine the stress relaxation. As usual, DIC analysis is performed as a post-processing step, used here to obtain the actual stretch in the gauge section during the relaxation experiment.

Lastly, to complement the quasi-static large deformation testing and to ensure a time-independent response of the virgin material, we additionally performed:
(i) stress relaxation testing at various stretch levels, until stress equilibrium has been reached over 24 hours; and (ii) creep testing at various constant stresses, until stretch equilibrium has been reached over 24 hours.

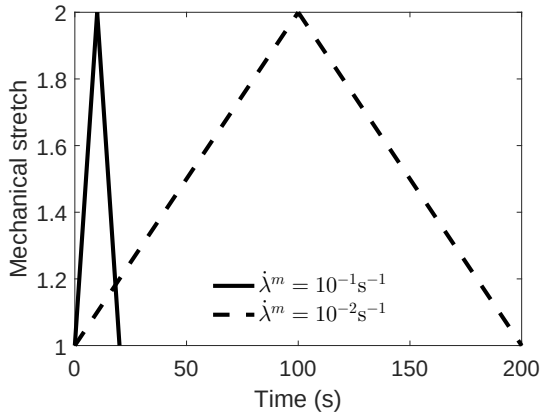

Figure 2.3 Prescribed loading-unloading stretch profile to a maximum mechanical stretch of $\lambda^m = 2$.

2.3.3 Free Swelling Procedure

The free swelling procedure commences by taking the photos of virgin samples for dimensional measurements. Then, the virgin samples are fully submerged in ample solvent inside sealed glass jars. The sealed jars are placed inside a fume hood, and the samples are allowed to undergo free swelling for over 24 hours. During that time, the swelling process reaches equilibrium and samples are considered fully swollen. To ensure that equilibrium was reached, the mass of the samples is measured periodically using a Sartorius Practum213-1S scale.

To obtain the swelling stretch of the fully swollen samples, photos of fully swollen samples were taken. ImageJ [109] software is then used to measure the virgin and the fully swollen lengths, and the swelling stretch is obtained using (2.3). Assuming spherical swelling, the fully swollen sample dimensions are obtained by scaling the

virgin dimensions by the swelling stretch. Therefore, the cross sectional area of the fully swollen gauge section is

$$A^s = (\lambda^s t_0)\,(\lambda^s w_0) = (\lambda^s)^2\, A_0\,. \tag{2.11}$$

2.3.4 Fully Swollen Uniaxial Testing Procedure

Other than the samples being submerged in the water bath, the uniaxial testing procedure for a fully swollen gel is essentially the same as the dry procedure described in Subsection 2.3.2. The main differences lie in the care needed in analysis to account for the prior swelling deformation, and the affects of the water bath such as buoyancy. As before, DIC is used in all cases as a post processing step to assess the actual deformation in the gauge section.

Large deformation quasi-static tensile tests are performed at a very slow mechanical stretch rate of $\dot{\lambda}^m = 10^{-4}\mathrm{s}^{-1}$, based on the swollen length of the gauge section. Fully swollen samples were subjected to a prescribed total stretch of either $\lambda = 10$, or just prior to failure, followed by unloading to the initial stretch of $\lambda = \lambda^s$, which is the freely swollen stretch.

For moderate rate loading-unloading tensile tests, the sample is loaded to a mechanical stretch of $\lambda^m = 2$, which corresponds to a total stretch $\lambda = \lambda^m\lambda^s = 2\lambda^s$, followed by unloading to $\lambda^m = 1$, which matches the initial freely swollen total stretch of $\lambda = \lambda^s$. To assess rate dependency, two different rates are used $\dot{\lambda}^m = 10^{-2}\,\mathrm{s}^{-1}$ and $10^{-1}\,\mathrm{s}^{-1}$, and Figure 2.3 shows the prescribed stretch profiles.

Finally, we perform a set of stress relaxation tests, in which the samples are first loaded to $\lambda^m = 2$ at a stretch rate $\dot{\lambda}^m = 2 \times 10^{-1}\,\mathrm{s}^{-1}$, and held at that fixed stretch for 1 hour, while the force is being recorded to determine the stress relaxation behavior.

2.3.5 Solvent Cycling Procedure

As mentioned earlier, solvent cycling is the process of swelling, followed by drying. Following the free swelling procedure, some specimens were then allowed to freely dry. The free swelling procedure was already described in Subsection 2.3.3, and is followed again for solvent cycling. The free drying procedure is very similar, however the swollen samples are set inside a petri dish, free of constraint, in a fume hood for 48 hours. Mass measurements are taken frequently along the process as described previously. We consider the sample to be completely dry once its mass is nearly equal (i.e., the same value relative to the instrument precision) to that of the dry virgin sample, implying all the solvent has evaporated from the polymer network.

2.3.6 Uniaxial Testing Procedure After Solvent Cycling

The uniaxial testing procedure of samples that underwent solvent cycling consists of nearly the identical set of experiments used to test virgin samples. First, the large deformation quasi-static response of the material is probed through uniaxial tensile tests at a very slow mechanical stretch rate of $\dot{\lambda^m} = 10^{-4}\text{s}^{-1}$, based on the solvent cycled gauge section length (which coincides with the virgin length). For this purpose, the samples have been deformed to a prescribed mechanical stretch $\lambda^m = 10$. Next, to determine the hysteresis in the material response, along with the rate-dependence, we perform a set of load-unload tensile tests to a mechanical stretch of $\lambda^m = 2$, employing two different deformation rates $\dot{\lambda^m} = 10^{-2}\text{s}^{-1}$ and 10^{-1}s^{-1}. Lastly, a set of stress relaxation tests at a fixed stretch of $\lambda^m = 2$ were performed with a relaxation time of over 1 hour.

2.3.7 Experimental Results

Uniaxial Results on Virgin Specimens The results of our uniaxial tests on virgin specimens are shown in Figure 2.4. Specifically, Figure 2.4a very clearly shows

the large deformation response under very slow loading. Here, clear evidence of the chain-locking behavior of VHB 4910 is observed at a uniaxial mechanical stretch of $\lambda^m \approx 9$. Further, the dry virgin material exhibits pronounced rate-dependent behavior, which is observed in Figure 2.4a and 2.4b. The load-unload tensile tests at two moderate rates show clear rate-dependence as well as significant hysteresis upon unloading due to viscoelastic effects. Lastly, Figure 2.4c shows the measured stress relaxation behavior at an applied stretch of $\lambda = 2$. From this figure one clearly observes relaxation, going from a nominal stress of just over 110 kPa and relaxing to just over 40 kPa over 1 hour. In Figure 2.4d the large deformation quasi-static tension test results at a rate of 10^{-4}s^{-1} are plotted along with the long term creep and relaxation data at equilibrium. Since the large deformation quasi-static tensile response has some hysteresis, we interpolated the creep and relaxation data (utilizing the `smooth` function in MATLAB) to obtain the time-independent response of the material.

To quantify the experimental observations and rate-dependent behavior of the material, we measure the stiffness and hysteresis at different stretch rates. The initial stiffness $\frac{dP}{d\lambda^m}$ is measured for all three $\dot{\lambda}^m$ employed in tensile testing. Additionally, from the data obtained using a large deformation quasi-static test, we also measure the stiffness near the maximum measurable, and midway. The amount of hysteresis is determined by the area enclosed by the loading and unloading path on the stress-stretch curve.

The measured effects of locking are clear, with an increase in stiffness $\frac{dP}{d\lambda^m}$ from 17.19 kPa at a stretch of 4.5 to 102.53 kPa at a stretch of 8.36. Further, the experimental results showcase a noticeable increase in initial stiffness with an increase in $\dot{\lambda}^m$, ranging from 60.2 kPa for the $\dot{\lambda}^m = 10^{-4}\text{s}^{-1}$, 170.18 kPa for the $\dot{\lambda}^m = 10^{-2}\text{s}^{-1}$, to 333.31 kPa for the $\dot{\lambda}^m = 10^{-1}\text{s}^{-1}$. In addition to the increase in stiffness, one

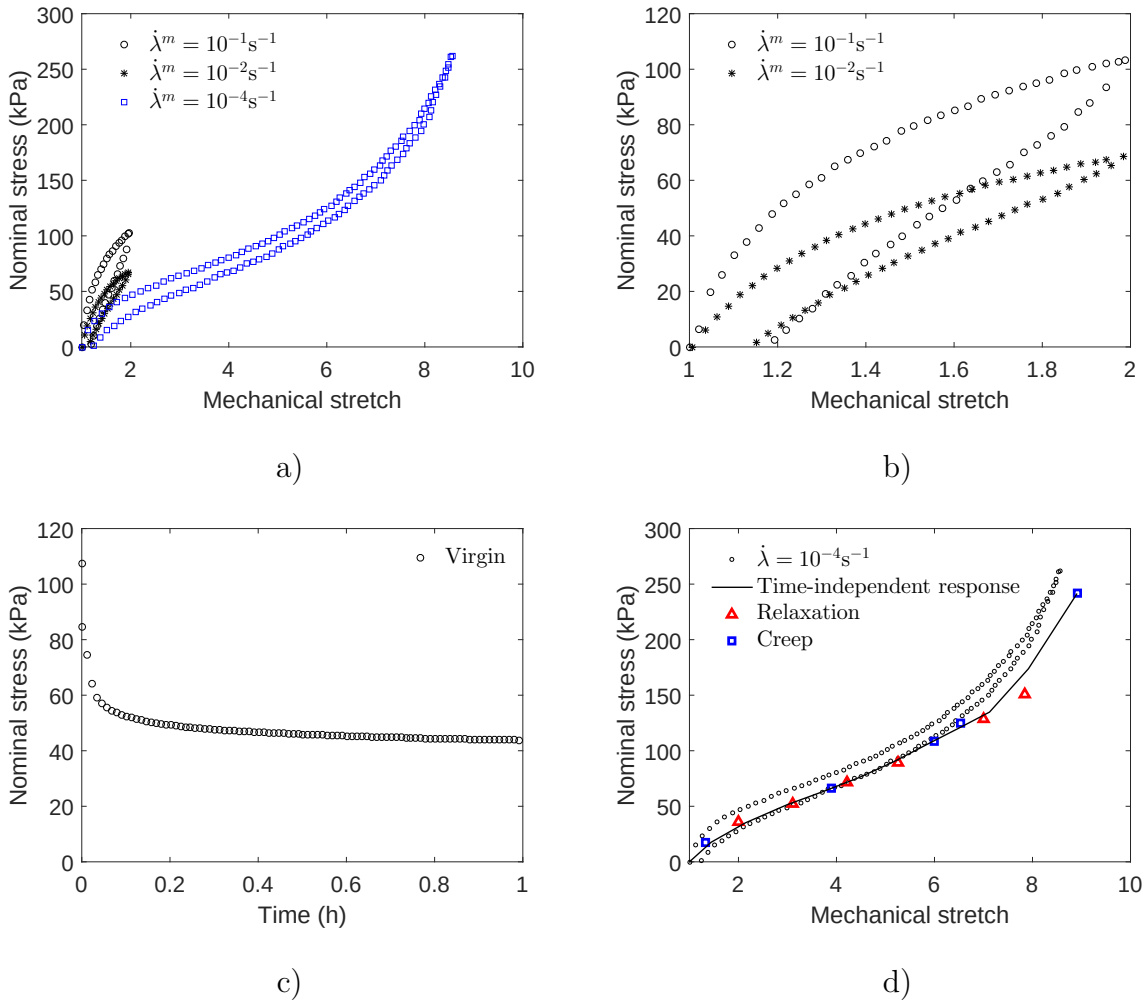

Figure 2.4 Uniaxial experimental results for dry virgin specimens. a) Large deformation quasi-static and moderate rate load-unload uniaxial tensile tests, with nominal stress as a function of mechanical stretch λ^m, which in case of dry samples is the same as the total stretch λ. b) The same load-unload data at moderate rates in a smaller range of stretch for clarity. c) Stress relaxation for an applied mechanical stretch of 2. And d) comparison between the quasi-static large deformation tensile test and the time-independent behavior obtained through combination of stress relaxation and creep testing.

can notice an increase in hysteresis from 15.82 kPa at $\dot{\lambda}^m = 10^{-2}\,\text{s}^{-1}$ to 31.41 kPa at $\dot{\lambda^m} = 10^{-1}\,\text{s}^{-1}$.

We note that the tabulated data and comparisons to the fully swollen material is provided later in Subsection 2.3.7 when the fully swollen results are discussed.

Free Swelling Results As mentioned previously, optical measurements of specimens before and after free swelling of VHB 4910 in various solvents provide a reliable measurement of the swelling stretch at equilibrium without constraints. Figure 2.5 shows the virgin dry specimen, and the corresponding fully swollen specimen for the solvents: a) n-Pentane; b) o-Xylene; and c) Toluene. The average mass of our virgin samples is 0.495 g prior to solvent exposure. Our measurements show that a VHB 4910 specimen fully swollen in n-Pentane on average absorbs 0.66 g of solvent and has a swelling stretch of $\lambda^s = 1.49$. Similar measurements for o-Xylene show that it absorbs 3.47 g of solvent and has a swelling stretch of $\lambda^s = 1.95$. And lastly for Toluene, 3.40 g are absorbed and the swelling stretch is $\lambda^s = 1.98$. To ensure the equilibrium, the mass is measured periodically over 48 hours. Figure 2.6 clearly shows the swelling process reaching equilibrium in about 24 hours, for all three solvents.

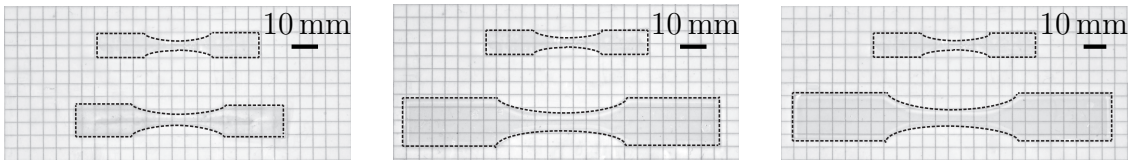

a) b) c)

Figure 2.5 VHB 4910 ASTM D638-V dog-bone specimens before and after free swelling to equilibrium, and also used for uniaxial testing. a) Dry and swollen with n-Pentane, with equilibrium swelling stretch $\lambda^s = 1.49$. b) Dry and swollen with o-Xylene with equilibrium swelling stretch $\lambda^s = 1.95$. c) Dry and swollen with Toluene with equilibrium swelling stretch $\lambda^s = 1.98$. We note that the dotted lines are drawn along the edges of specimens to emphasize the specimen boundary for this transparent material.

Uniaxial Results on Fully Swollen Specimens The results of our uniaxial tests of fully swollen specimens are shown in Figure 2.7 for tension tests on VHB fully swollen with n-Pentane, Figure 2.8 for tension tests on VHB fully swollen with o-Xylene, Figure 2.9 for tension tests on VHB fully swollen with Toluene, and Figure 2.10 for relaxation tests on specimens fully swollen with all three solvents.

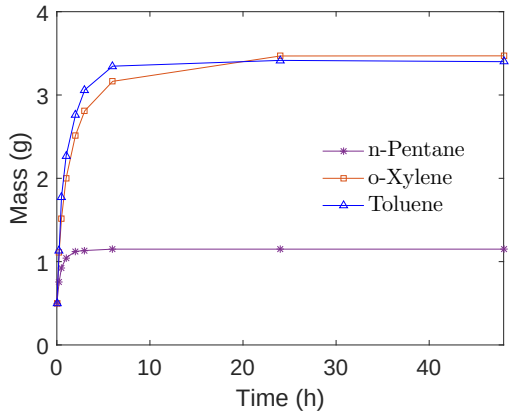

Figure 2.6 Sample mass measured periodically over 48 hours of free swelling indicating equilibrium is reached at 24 hours.

First considering the tensile behavior of VHB 4910 fully swollen in n-Pentane, Figure 2.7 shows the large deformation quasi-static load-unload response, as well as the load-unload response at a few fixed, but different, moderate stretch rates. Based on the large deformation tensile test we can observe no hysteresis in the response of the material, along with a decrease in the initial effective stiffness from 60.2 kPa to 27.53 kPa, as seen in Table 2.1. Also, we find that the material does not show any clear locking behavior when compared to the virgin material, with the stiffness increasing from 14.41 kPa at a total stretch of 4.5 to just 17.85 kPa at a stretch of 7.73, as shown in Table 2.2. Looking at the moderate rate load-unload data to a stretch of 2, the measured initial effective stiffness $\frac{dP^m}{d\lambda^m}$ drops to 32.74 kPa at $\dot{\lambda}^m = 10^{-2}\,\mathrm{s}^{-1}$ and 34.29 kPa at $\dot{\lambda}^m = 10^{-1}\,\mathrm{s}^{-1}$. The difference in stiffness at various stretch rates is negligible compared to the virgin material (see Table 2.1), and the samples exhibit an almost complete absence of rate-dependency in the response. Along with the decrease in stiffness, one can observe the lack of hysteresis, with the measured hysteresis area going from 15.82 kPa to 0.37 kPa at $\dot{\lambda}^m = 10^{-2}\,\mathrm{s}^{-1}$, and from 31.41 kPa to 0.84 kPa at $\dot{\lambda}^m = 10^{-1}\,\mathrm{s}^{-1}$, as seen in Table 2.3. *In summary, the load-unload tensile experiments at various rates show no signs of rate-dependence or hysteresis.*

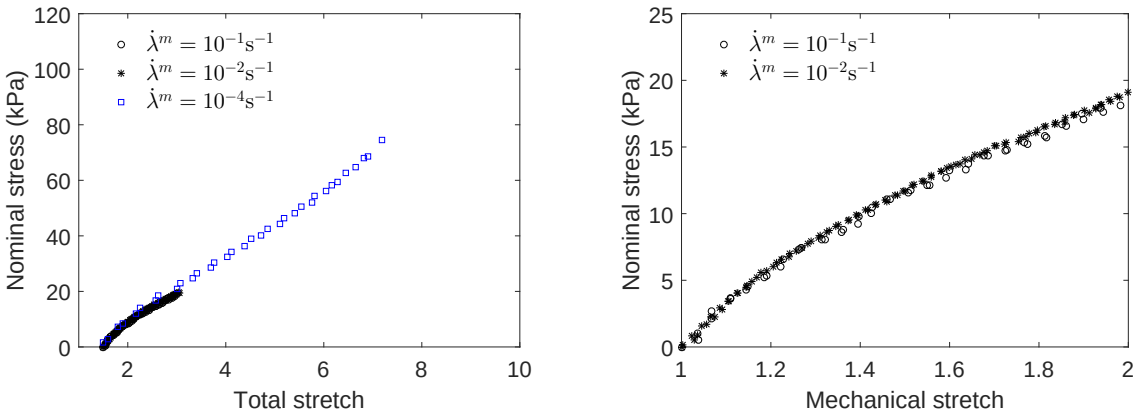

a) b)

Figure 2.7 Experimental results for samples swollen in n-Pentane. a) Large deformation quasi-static load-unload, along with load-unload moderate rate tests to $\lambda^m = 2$, with results presented as a function of total stretch $\lambda = 1.49\lambda^m$. b) Load-unload tests to $\lambda^m = 2$ at moderate stretch rates and presented as a function of mechanical stretch.

Next, considering the tensile behavior of VHB 4910 fully swollen in o-Xylene, Figure 2.8 shows the large deformation quasi-static load-unload response, as well as the load-unload response at a few fixed, but different, moderate stretch rates. Based on the large deformation tensile test we can observe the absence of hysteresis in the material response, followed by the decrease in the initial effective stiffness from 60.2 kPa to 24.73 kPa, as seen in Table 2.1. Also, we find that the material has failed at a total stretch of 6.85, whereas the virgin material was still intact. Further, the material does not show any clear locking behavior compared to the virgin material, with an increase in stiffness from 19.36 kPa at a total stretch of 4.5, to 24.75 kPa at the failure stretch, as seen in Table 2.2. Measuring the initial effective stiffness $\frac{dP^m}{d\lambda^m}$ for moderate rate load-unload results, we notice the drop to 23.94 kPa at $\dot{\lambda}^m = 10^{-2}\,\text{s}^{-1}$ and 26.59 kPa at $\dot{\lambda}^m = 10^{-1}\,\text{s}^{-1}$. The difference in stiffness at various stretch rates is negligible compared to the virgin material, displaying almost the complete absence of rate-dependency in the response, as seen in Table 2.1. Along with the decrease in stiffness, we measure almost a complete lack of hysteresis, with the measured

hysteresis area going from 15.82 kPa to 0.18 kPa at $\dot{\lambda}^m = 10^{-2}\,\mathrm{s}^{-1}$, and from 31.41 kPa to 0.46 kPa at $\dot{\lambda}^m = 10^{-1}\,\mathrm{s}^{-1}$, as seen in Table 2.3. *Again, the load-unload tensile experiments at various rates show no apparent signs of rate-dependence or hysteresis.*

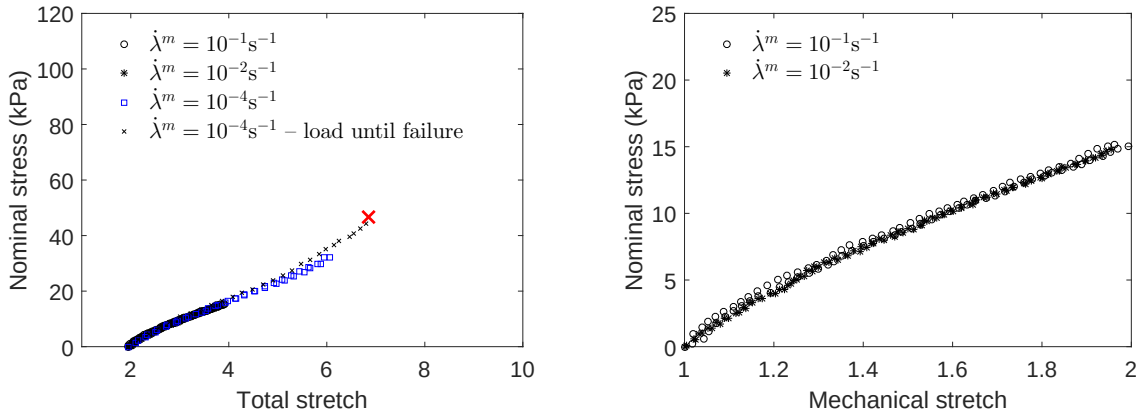

a) b)

Figure 2.8 Experimental results for samples swollen in o-Xylene. a) Large deformation, along with load-unload testing to $\lambda^m = 2$, with results as a function of total stretch $\lambda = 1.95\lambda^m$. b) Load-unload tests to $\lambda^m = 2$ at different mechanical stretch rates and presented as a function of mechanical stretch. The red $\times$ indicates failure of the sample.

Further, considering the tensile behavior of VHB 4910 fully swollen in Toluene, Figure 2.9 shows the large deformation quasi-static load-unload response, as well as the load-unload response at a few fixed, but different, moderate stretch rates. Based on the large deformation tensile test we can observe the lack of hysteresis in the material response, followed by the decreases in the initial effective stiffness from 60.2 kPa to 21.58 kPa, as seen in Table 2.1. Also, we find that the material has failed at a total stretch of 7.81, whereas the virgin material was still intact. The material does not show any clear locking behavior compared to the virgin material, with an increase in stiffness from 13.16 kPa at a total stretch of 4.5, to 18.49 kPa at the failure stretch, as shown in Table 2.2. Measuring the initial effective stiffness $\frac{dP^m}{d\lambda^m}$ from moderate rate load-unload data, we observe a drop to 22.01 kPa at $\dot{\lambda}^m = 10^{-2}\,\mathrm{s}^{-1}$ and 21.44 kPa

at $\dot{\lambda}^m = 10^{-1}\,\mathrm{s}^{-1}$. The difference in stiffness at various stretch rates is negligible compared to the virgin material, displaying the absence of rate-dependency in the response, as observed in Table 2.1. Along with the decrease in stiffness, we notice the lack of hysteresis, with a decrease in the measured hysteresis area from 15.82 kPa to 0.6 kPa at $\dot{\lambda}^m = 10^{-2}\,\mathrm{s}^{-1}$, and from 31.41 kPa to 0.33 kPa at $\dot{\lambda}^m = 10^{-1}\,\mathrm{s}^{-1}$, as seen in Table 2.3. *Again, the load-unload tensile experiments at various rates show no signs of rate-dependence or hysteresis.*

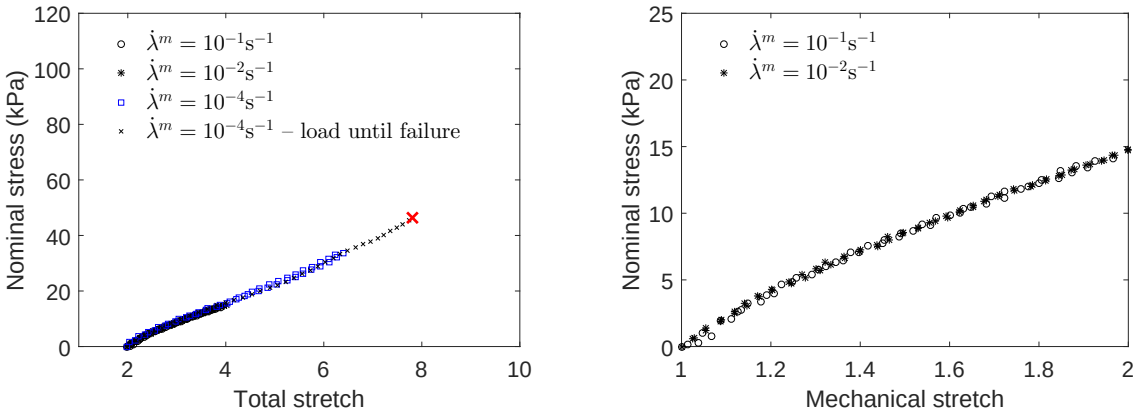

a) b)

Figure 2.9 Experimental results for samples swollen in Toluene. a) Large deformation, along with load-unload testing to $\lambda^m = 2$, with results as a function of total stretch $\lambda = 1.98\lambda^m$. b) Load-unload tests to $\lambda^m = 2$ at different mechanical stretch rates and presented as a function of mechanical stretch. The red $\times$ indicates failure of the sample.

Table 2.1 Measured Initial Effective Stiffness, $\frac{dP}{d\lambda^m}$ for Birgin, and $\frac{dP^m}{d\lambda^m}$ for Fully Swollen Samples at Different Applied Stretch Rates.

$\dot{\lambda}^m$ (s^{-1})	10^{-4}	10^{-2}	10^{-1}
Virgin (kPa)	60.20	170.18	333.31
n-Pentane (kPa)	27.53	32.74	34.29
o-Xylene (kPa)	24.73	23.94	26.59
Toluene (kPa)	21.58	22.01	21.44

Table 2.2 Chain-Locking Behavior Observed Through Stiffness Measurements on Virgin ($\frac{dP}{d\lambda^m}$) and Fully Swollen ($\frac{dP^m}{d\lambda^m}$) Samples with Data Taken at a Stretch Rate of $\dot{\lambda} = 10^{-4}\text{s}^{-1}$. For Samples Swollen with o-Xylene and Toluene, We Take the Maximum λ to be at the Failure.

	Initial (kPa)	At $\lambda = 4.5$ (kPa)	Near max. λ (kPa)
Virgin	60.20	17.19	102.53 at ($\lambda = 8.36$)
n-Pentane	27.53	14.41	17.85 at ($\lambda = 7.73$)
o-Xylene	24.73	19.36	24.75 at ($\lambda = 6.85$)
Toluene	21.58	13.16	18.49 at ($\lambda = 7.81$)

Table 2.3 Measured Hysteresis for a Maximum Mechanical Stretch of 2 for Virgin and Fully Swollen Samples at Different Applied Stretch Rates.

$\dot{\lambda}^m$ (s^{-1})	10^{-2}	10^{-1}
Virgin (kPa)	15.82	31.41
n-Pentane (kPa)	0.37	0.84
o-Xylene (kPa)	0.18	0.46
Toluene (kPa)	0.6	0.33

Lastly, Figure 2.10 shows the stress relaxation behavior of VHB 4910 fully swollen in all three solvents with the virgin data superimposed. After a rapid crosshead displacement, the mechanical stretch is held fixed at $\lambda^m = 2$ for 1 hour. What is most notable about these results are that the behavior is nearly all elastic for all fully swollen gels. VHB 4910 swollen in o-Xylene and Toluene do not even have a measurable amount of stress relaxation, and the specimens fully swollen with n-Pentane show a dramatically decreased amount of relaxation, over a much shorter time span compared to the dry case.

Uniaxial Results on dry, Solvent Cycled Specimens Thus far, it is clear that the uptake of solvent has an affect on the mechanical behavior of these materials.

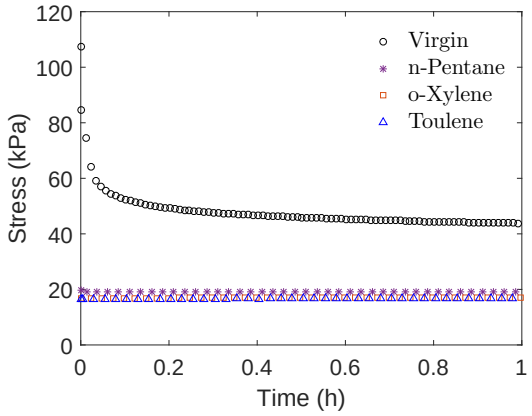

Figure 2.10 Virgin and fully swollen stress relaxation results. The virgin experiment is plotted using the stress measure P, while the swollen experiments are plotted using the stress measure P^m.

To assess if swelling causes irreversible changes to the mechanical behavior, we solvent cycle — freely swell, then freely dry — and then use those samples for uniaxial tests. Mass measurements shown in Figure 2.11 show all three solvents completely evaporating after about 24 hours of free drying, ensuring fully dried samples for mechanical testing. For samples that have been solvent cycled five times, Figure 2.12 shows the reappearance of chain-locking behavior, and Figure 2.13 shows the reappearance of the viscoelastic response for uniaxial load-unload experiments. Additionally, Figure 2.14 shows a reappearance of viscoelasticity for the material subjected to a stress relaxation experiment. These combined results show that *prior solvent cycling has no significant residual effects on the overall response of the polymer, which we take as an indication of the reversibility of the process.*

2.3.8 Summary of the Experimental Results

Figure 2.15 shows already presented data, but now with multiple stretch-stress curves all superimposed atop each other, and immediately the change in behavior is visible. The behavior of virgin samples shows clear viscoelastic effects. However, the fully swollen results show no signs of rate dependency, nor hysteresis, with load-unload

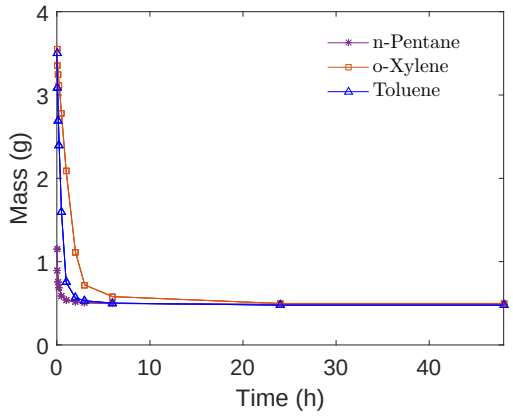

Figure 2.11 Mass of initially fully swollen samples, measured periodically during 48 hours of free drying.

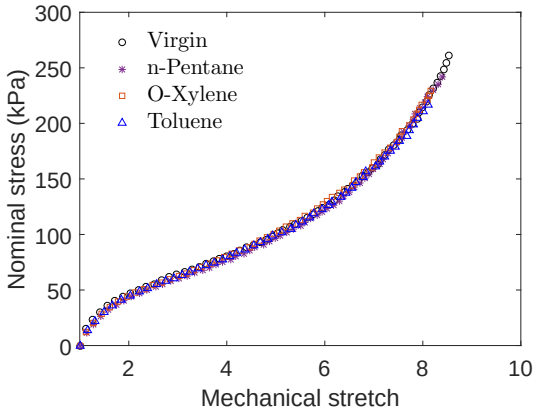

Figure 2.12 Large deformation uniaxial tensile loading results after solvent cycling 5 times with n-Pentane, o-Xylene and Toluene, along with a virgin sample. The results lie almost completely on top of each other.

stretch-stress curves obtained at different rates being almost completely on top of each other. Measurements of the hysteresis, stiffness, and stress-stretch behavior all lead toward the hypothesis that **the fully swollen material has lost nearly all viscoelasticity, and the fully swollen material behaves like a non-linear elastic material.** Further, our solvent cycling results show that **prior solvent cycling has no significant residual effects on the overall response of the polymer, which we take as an indication of the reversibility of the process.**

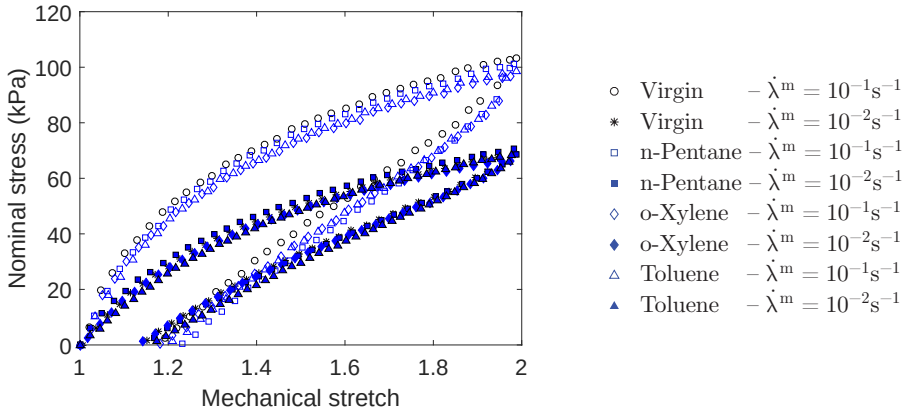

Figure 2.13 Uniaxial load-unload tensile test results after solvent cycling 5 times with n-Pentane, o-Xylene and Toluene. For ease of comparison, we also show the virgin results.

Based on some discussions in the literature (e.g., [40, 129]) one possible mechanism for this change in behavior is that when the polymer network is expanded by introducing solvent molecules, the interaction between polymer chains becomes very small because the distance of the individual chains becomes larger, resulting in the absence of viscosity.

Additionally, the well known and prevalent [44] model predicts the effective modulus under uniaxial tension to be $E = E_d J^{-1/3}$, where E_d is the dry elastic modulus [100]. However, based on the quasi-static results shown in Table 2.1 we find that **the effective modulus is not a function of the swelling ratio alone** and is affected by other factors such as the specific solvent. Here o-Xylene has an equilibrium swelling stretch of $\lambda^s = 1.95$ and Toluene has $\lambda^s = 1.98$, based on the [44] model we should expect the ratio of moduli to be

$$\frac{E_{\text{o-Xylene}}}{E_{\text{Toluene}}} = \frac{J^{-1/3}_{\text{o-Xylene}}}{J^{-1/3}_{\text{Toluene}}} = \frac{\lambda^s_{\text{Toluene}}}{\lambda^s_{\text{o-Xylene}}} = \frac{1.98}{1.95} = 1.015$$

however the measured ratio is 1.146, over a 10% difference.

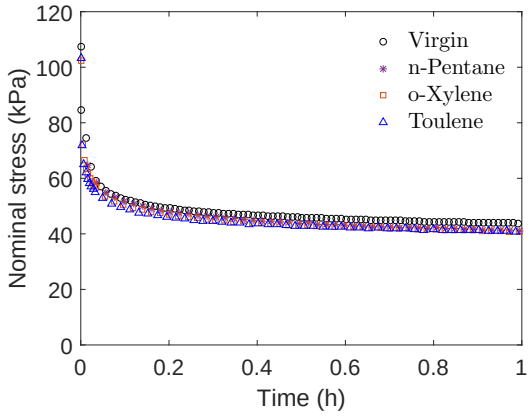

Figure 2.14 Stress relaxation of virgin VHB, and after five cycles of swelling with n-Pentane, o-Xylene and Toluene. The results lie almost completely on top of each other.

2.4 Constitutive Model

In this section we overview a continuum-level constitutive model for polymeric gels, which aims to give particular attention to the viscoelastic response. The large deformation time-independent response of the polymer is modeled employing a non-Gaussian statistical mechanics model, which takes into account the limited extensibility of polymer chains [5, 3], as well as a scaling exponent on the swelling ratio to account for the change in effective stiffness [100, 144]. Viscous effects are modeled following the micromechanically motivated approach by [49] and [83]. Lastly, the mixing between the polymer network and solvent is accounted for by the Flory-Huggins model [43, 64]. The model, in it's current form, follows from the previous work of our research group [16, 17, 15, 18] and is summarized in this section for clarity. However, in contrast to our previous models, we do not explicitly account for solvent diffusion, and only consider equilibrium conditions. This assumption is made since our experiments are not intended to probe the diffusive behavior of these polymeric gels. Lastly, while it is well known that more complete constitutive models exist to capture the elastic modulus of swollen elastomers (cf. e.g., [100]), we do not

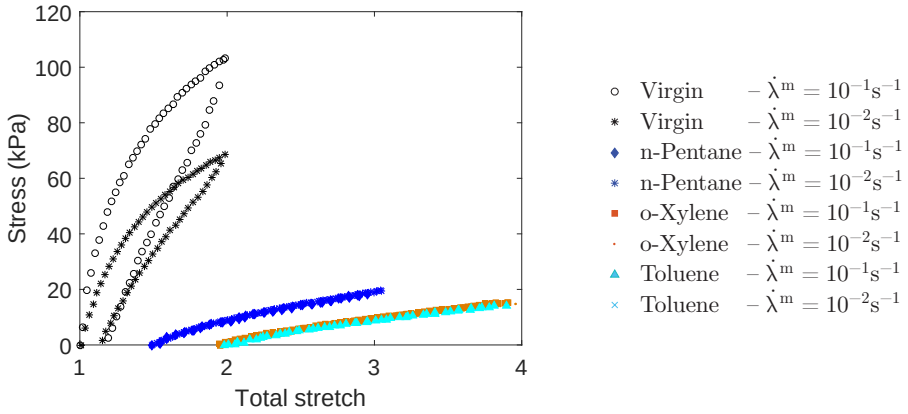

Figure 2.15 A subset of the experimental results showing the load-unload response for moderate rates displaying the clear affect of swelling on the behavior. The virgin experiments are plotted using the stress measure P, while the swollen experiments are plotted using the stress measure P^m.

burden ourselves with the extra complexity since the focus here is on the viscoelastic behavior.

2.4.1 Kinematics

The model is based on a multiplicative decomposition of the deformation gradient into mechanical and swelling parts

$$\mathbf{F} = \mathbf{F}^m\mathbf{F}^s \quad \text{with} \quad \mathbf{F}^s = \lambda^s\mathbf{1}, \quad \lambda^s \geq 1\,. \tag{2.12}$$

In (2.12) $\mathbf{F}^s(\mathbf{x}_{\mathrm{R}})$ represents the local distortion of the material due to swelling at an arbitrary material point $\mathbf{x}_{\mathrm{R}}$ of the undeformed body $\mathcal{B}_{\mathrm{R}}$, and λ^s is the swelling stretch. This local deformation accounts for the swelling of the material due to absorbed solvent molecules. $\mathbf{F}^m(\mathbf{x}_{\mathrm{R}})$ represents the subsequent mechanical stretching and rotation of this coherent swollen network structure.

With respect to (2.12), the right and left Cauchy-Green tensors are

$$\mathbf{C} = \mathbf{F}^{\top}\mathbf{F} = (\mathbf{F}^m\mathbf{F}^s)^{\top}(\mathbf{F}^m\mathbf{F}^s) = \mathbf{F}^{m\top}\mathbf{F}^m\,(\lambda^s)^2 = \mathbf{C}^m\,(\lambda^s)^2\,, \quad \text{and} \tag{2.13}$$

$$\mathbf{B} = \mathbf{F}\mathbf{F}^{\top} = (\mathbf{F}^m\mathbf{F}^s)\,(\mathbf{F}^m\mathbf{F}^s)^{\top} = \mathbf{F}\mathbf{F}^{m\top}\,(\lambda^s)^2 = \mathbf{B}^m\,(\lambda^s)^2\,, \tag{2.14}$$

respectively.

Next, we assume that the mechanical response of the solvent and polymeric material is purely incompressible, and therefore $J^m = 1$. Further, we assume that the only volume change is due to swelling caused by the solvent, which is given by

$$J^s = 1 + \Omega c_{\mathrm{R}} \,, \tag{2.15}$$

where Ω is the molar volume of the solvent and c_{R} is solvent concentration measured in moles of fluid absorbed per unit reference volume. In addition, since

$$J^s = \det \mathbf{F}^s = (\lambda^s)^3 \,, \tag{2.16}$$

and with respect to (2.15), we may write

$$\lambda^s = (1 + \Omega c_{\mathrm{R}})^{1/3} \,. \tag{2.17}$$

2.4.2 Free Energy

The experimental observations clearly show the material to be viscoelastic when dry, and also capable of undergoing swelling deformation in the presence of an ample solvent. To model the features of such a material, we consider the following three contributions to the free energy: (i) a time-independent contribution to account for the long time mechanical behavior; (ii) a time-dependent contribution to account for viscous effects; and (iii) a chemical mixing contribution to account for mixing between the solvent and polymer network. Thus, our basic form of the free energy function which accounts for the combined effects of mechanical stretching, swelling and mixing consists of three parts

$$\psi_{\mathrm{R}} = \psi_{\mathrm{R}}^{\mathrm{TI}} + \sum_{\gamma} \psi_{\mathrm{R}}^{\mathrm{TD}(\gamma)} + \psi_{\mathrm{R}}^{\mathrm{chem}} \tag{2.18}$$

where $\psi_{\mathrm{R}}^{\mathrm{TI}}$ models time-independent response, $\sum_{\gamma} \psi_{\mathrm{R}}^{\mathrm{TD}(\gamma)}$ models time-dependent behavior employing γ viscous mechanisms, and $\psi_{\mathrm{R}}^{\mathrm{chem}}$ is the chemical free energy of mixing between the polymer network and the solvent.

For the time-independent free energy, we adopt the statistical mechanics based Arruda-Boyce model [5, 3] which takes into account the limited extensibility of polymer chains, coupled with a scaling exponent to account for stiffness changes [100],

$$\psi_{\mathrm{R}}^{\mathrm{TI}} = G_0 \lambda_L^2 J^q \left[\left(\frac{\bar{\lambda}}{\lambda_L} \right) \beta + \ln \left(\frac{\beta}{\sinh \beta} \right) - \left(\frac{1}{\lambda_L} \right) \beta_0 - \ln \left(\frac{\beta_0}{\sinh \beta_0} \right) - 3J^{2/3} \right] + G_0 \lambda_L^2 \left[3J^{2/3} \right] - G_0 \left(\frac{\lambda_L \beta_0}{3} \right) \ln J \ . \quad (2.19)$$

Here G_0 is the initial shear modulus, λ_L is the locking stretch, and $\bar{\lambda} = \sqrt{\mathrm{tr}\,\mathbf{C}/3}$ is the effective stretch. Additionally, β and β_0 are functions given by

$$\beta = \mathcal{L}^{-1} \left(\frac{\bar{\lambda}}{\lambda_L} \right) \quad \text{and} \quad \beta_0 = \mathcal{L}^{-1} \left(\frac{1}{\lambda_L} \right), \quad (2.20)$$

where $\mathcal{L}^{-1}$ is the inverse of the Langevin function, $\mathcal{L}(\bullet) = \coth(\bullet) - 1/(\bullet)$. The locking stretch, λ_L, is the effective stretch where the polymer network is fully extended and cannot extend any further.

For the time-dependent contribution to the free energy, we follow the approach of [49] and [83] which takes the form

$$\psi_{\mathrm{R}}^{\mathrm{TD}(\gamma)} = \frac{1}{2} G_{\mathrm{TD}}^{(\gamma)} \left[\left(\mathbf{A}^{(\gamma)} : \mathbf{C}^m - 3 \right) - \ln \left(\det \mathbf{A}^{(\gamma)} \right) \right] \quad (2.21)$$

where $G_{\mathrm{TD}}^{(\gamma)}$ are the shear moduli for each viscous mechanism γ. The evolution equation of each tensorial internal variable $\mathbf{A}^{(\gamma)}$ is given in the form

$$\dot{\mathbf{A}}^{(\gamma)} = \frac{1}{\tau^{(\gamma)}} \left((\mathbf{C}^m)^{-1} - \mathbf{A}^{(\gamma)} \right), \quad \mathbf{A}\left(\mathbf{x}_{\mathrm{R}}, t = 0\right) = 1 \,, \quad (2.22)$$

where $\tau^{(\gamma)}$ is the relaxation time for each γ.

We adopt a Flory-Huggins [42, 64] model for the chemical mixing free energy which takes into account the mixing of polymer and solvent molecules

$$\psi_{\mathrm{R}}^{\mathrm{chem}} = \mu^0 c_{\mathrm{R}} + R\vartheta c_{\mathrm{R}} \left(\ln\left(\frac{\Omega c_{\mathrm{R}}}{1+\Omega c_{\mathrm{R}}}\right) + \chi\left(\frac{1}{1+\Omega c_{\mathrm{R}}}\right)\right) . \tag{2.23}$$

Where μ^0 is the chemical potential of the solvent, R is the universal gas constant, ϑ the absolute temperature, and χ polymer-solvent interaction parameter.

2.4.3 Cauchy Stress

The Cauchy stress $\mathbf{T}$ is given by

$$\mathbf{T} = J^{-1}\left(2\mathbf{F}^m \frac{\partial \psi_{\mathrm{R}}}{\partial \mathbf{C}^m}\mathbf{F}^{m\top} - p\mathbf{1}\right) = J^{-1}\left[GJ^q\left(\lambda^s\right)^2\mathbf{B}^m + \sum_\gamma G_{\mathrm{TD}}^{(\gamma)}\mathbf{F}^m\mathbf{A}^{(\gamma)}\mathbf{F}^{m\top} - p^*\mathbf{1}\right], \tag{2.24}$$

where the shear modulus $G = G_0\left(\frac{\lambda_L}{3\bar{\lambda}}\right)\mathcal{L}^{-1}\left(\frac{\bar{\lambda}}{\lambda_L}\right)$ is a function of stretch, and p a scalar pressure field to satisfy the mechanical incompressibility constraint. The term p^* simply aggregates all of the spherical terms that arise.

2.4.4 Chemical Potential

Based on the thermodynamic derivation found in the previous work from our group (c.f., e.g., [16]), and using the free energy form (2.18), the chemical potential μ is given by

$$\begin{aligned}\mu &= \frac{\partial \psi_{\mathrm{R}}}{\partial c_{\mathrm{R}}} - \frac{1}{3}\mathrm{tr}\,\mathbf{T}\Omega \\ &= \mu^0 + R\vartheta\left(\ln\left(\frac{\Omega c_{\mathrm{R}}}{1+\Omega c_{\mathrm{R}}}\right) + \frac{1}{1+\Omega c_{\mathrm{R}}} + \chi\frac{1}{\left(1+\Omega c_{\mathrm{R}}\right)^2}\right) + \left(p - G_0\right)\frac{\Omega}{1+\Omega c_{\mathrm{R}}} .\end{aligned} \tag{2.25}$$

Further, since we do not account for diffusion, the role of the chemical potential serves to obtain the conditions for chemical equilibrium, which is obtained when $\mu = \mu^0$. A few examples of when this may be put to use are to obtain the parameter χ in a free swelling experiment, or obtaining the swelling stretch for a given loading.

2.4.5 Specialized Constitutive Equations for Uniaxial Tension and Free Swelling/Drying

When specialized for uniaxial tension, the constitutive model reduces to a one-dimensional set of equations, in which case the Cauchy stress takes the form

$$\sigma = \underbrace{J^{-1} G J^q \left(\lambda^s\right)^2 \left[\left(\lambda^m\right)^2 - \frac{1}{\lambda^m}\right]}_{\text{Time-independent contribution}} + \underbrace{J^{-1} \sum_{\gamma} G_{\mathrm{TD}}^{(\gamma)} \left[\left(\lambda^m\right)^2 A^{(\gamma)} - \frac{1}{\lambda^m \sqrt{A^{(\gamma)}}}\right]}_{\text{Time-dependent contribution}}, \tag{2.26}$$

where σ is the Cauchy stress in the loading direction. The evolution equation of each $A^{(\gamma)}$ in case of uniaxial tension is given in the form

$$\dot{A}^{(\gamma)} = \frac{1}{\tau^{(\gamma)}} \left(\left(\lambda^m\right)^{-2} - A^{(\gamma)}\right). \tag{2.27}$$

Further, with respect to (2.7) and (2.8) we obtain the uniaxial nominal stress per unit virgin cross sectional area

$$P = \underbrace{G J^q \lambda^s \left[\lambda^m - \frac{1}{\left(\lambda^m\right)^2}\right]}_{\text{Time-independent contribution}} + \underbrace{\sum_{\gamma} G_{\mathrm{TD}}^{(\gamma)} \left(\lambda^s\right)^{-1} \left[\lambda^m A^{(\gamma)} - \frac{1}{\left(\lambda^m\right)^2 \sqrt{A^{(\gamma)}}}\right]}_{\text{Time-dependent contribution}} \tag{2.28}$$

and the mechanical nominal stress per unit freely swollen cross sectional area

$$P^m = \underbrace{G J^q \left(\lambda^s\right)^2 \left[\lambda^m - \frac{1}{\left(\lambda^m\right)^2}\right]}_{\text{Time-independent contribution}} + \underbrace{\sum_{\gamma} G_{\mathrm{TD}}^{(\gamma)} \left[\lambda^m A^{(\gamma)} - \frac{1}{\left(\lambda^m\right)^2 \sqrt{A^{(\gamma)}}}\right]}_{\text{Time-dependent contribution}}, \tag{2.29}$$

respectively. For clarity, here we explicitly labeled the time-independent and time-dependent contributions to the materials behavior.

For mechanical testing and shape change measurements of all of our samples, we assume chemical equilibrium, and accordingly $\mu = \mu^0$. Therefore, following (2.25), we obtain

$$R\theta \left(\ln\left(1 - \left(\lambda^s\right)^{-3}\right) + \left(\lambda^s\right)^{-3} + \chi \left(\lambda^s\right)^{-6}\right) + \left(p - G_0\right) \Omega \left(\lambda^s\right)^{-3} = 0. \tag{2.30}$$

Which as mentioned before may be used to estimate χ in free swelling, or more generally the amount of solvent that a gel would uptake for a given loading condition.

2.5 Calibration

The constitutive model is calibrated in MATLAB for uniaxial conditions using the built-in least squares function `lsqnonlin`. The model calibration consists of multiple distinct steps that build upon each other. First, we determine the time-independent behavior of the virgin dry material in the absence of any solvent to obtain the time-independent material parameters G_0 and λ_L. Those time-independent material parameters are then held fixed for calibration of the time-dependent behavior for the dry virgin material in the absence of any solvent to obtain the time-dependent material parameters $G^{\mathrm{TD}(\gamma)}$ and $\tau^{(\gamma)}$, along with γ. Next, using free swelling data, the constitutive model is calibrated to obtain the polymer-solvent interaction parameter χ, for all of the polymer-solvent combinations in use in this paper implementing the previously calibrated equilibrium material parameters. Further, following the same procedure used for the virgin uniaxial tests, we calibrate our model to the experimental data obtained in our experiments on fully swollen samples. Lastly, also worth mentioning is that the calibration is performed separately for each of the solvents used.

2.5.1 Calibration of the Time-Independent Behavior

Calibration of the Virgin Time-Independent Behavior To determine the time-independent behavior of dry virgin VHB 4910, we calibrate our constitutive model against the time-independent data obtained through the combination of stress relaxation and creep testing, seen in Figure 2.4d. Figure 2.16a shows the calibrated constitutive model is in a good agreement with the experimental data on dry virgin material, and the calibrated material parameters G_0 and λ_L are provided in Table

2.4. We note that since the material is incompressible, and dry, the terms related to q will not affect the response and therefore q is not yet considered.

Calibration of the Fully Swollen Time-Independent Behavior Figures 2.16b, 2.16c and 2.16d show the calibrated model along with the experimental data for samples fully swollen in n-Pentane, o-Xylene, and Toluene, respectively. For the samples swollen with o-Xylene and Toluene, we calibrated the model against the experimental data from large deformation tensile testing until failure. The initial shear modulus G_0 and locking stretch λ_L obtained from virgin calibration are held fixed, and the corresponding material parameter q obtained when fully swollen in each solvent is provided in Table 2.4.

Table 2.4 Calibrated Time-Independent Material Parameters.

	G_0 (kPa)	λ_L	q
Virgin	15.10	7.02	N/A
n-Pentane	15.10	7.02	-1.07
o-Xylene	15.10	7.02	-0.89
Toluene	15.10	7.02	-0.95

2.5.2 Calibration of the Time-Dependent Behavior

Calibration of the Virgin Time-Dependent Behavior To calibrate the time-dependent portion of the constitutive model, we hold the virgin time-independent parameters fixed, and perform a least squares fit to the experimental data from load-unload tensile tests and stress relaxation tests on virgin samples. To keep the number of viscous mechanisms reasonably low, while still adequately modeling the behavior, we have found that three viscous mechanisms ($\gamma = 3$) are sufficient. Figure 2.17a and

2.17b show the calibrated model along with the experimental data. Values for the time-dependent material parameters $G_{\mathrm{TD}}^{(\gamma)}$ and $\tau^{(\gamma)}$ for virgin samples are presented in Table 2.5.

Calibration of the Fully Swollen Time-Dependent Behavior The comparison between the calibrated model and the loading-unloading experimental data for fully swollen samples is shown in Figure 2.17c, 2.18a and 2.18c, and showcases the ability of our model to account for the lack of both energy dissipation and rate dependent behavior of fully swollen material. Further, calibration of the constitutive model against the stress relaxation data for fully swollen samples is in a good agreement with the experimental observation regarding the absence of stress relaxation behavior. This can be seen in Figures 2.17d, 2.18b and 2.18d. However, there is a slight disagreement between the calibrated model and the experimental data for samples fully swollen with o-Xylene, as seen in Figures 2.18a and 2.18b. Although the vanishing of viscoelastic behavior is accounted for, the stress predicted by the calibrated model is slightly higher than the experimentally obtained values. The possible change in the locking stretch λ_L due to the solvent uptake could be a reason for this discrepancy, however that is not significant enough for us to consider in this work.

The calibrated material parameters are provided in Table 2.5. Based on the calibrated time-dependent materials parameters, for the samples fully swollen with n-Pentane, we observe a low utilization of viscous mechanisms with $G_{\mathrm{TD}}^{(1)} \approx G_{\mathrm{TD}}^{(2)} \approx 0$, and $G_{\mathrm{TD}}^{(3)}$ an order of magnitude lower than the values obtained from calibration of virgin behavior. Further, for the samples fully swollen with n-Pentane the relaxation time of the first viscous mechanism exhibits a very fast relaxation, since $\tau^{(1)} \approx 0\,\mathrm{s}$, while the second and third viscous mechanisms exhibit a very slow relaxation, with $\tau^{(2)} \approx 10^3\,\mathrm{s}$ and $\tau^{(3)} \approx 10^4\,\mathrm{s}$. For the samples fully swollen with o-Xylene and Toluene, one can observe the apparent absence of all viscous mechanisms since $G_{\mathrm{TD}}^{(\gamma)} \approx 0$ relative

to the virgin material, along with the instantaneous relaxation observed as $\tau^{(\gamma)} \approx 0$ leading to a time-independent response.

Table 2.5 Calibrated Time-Dependent Material Parameters.

	$G_{\mathrm{TD}}^{(1)}$(kPa)	$\tau^{(1)}$(s)	$G_{\mathrm{TD}}^{(2)}$(kPa)	$\tau^{(2)}$(s)	$G_{\mathrm{TD}}^{(3)}$(kPa)	$\tau^{(3)}$(s)
Virgin	38.29	6.91	14.41	165.86	12.87	1.07×10^{4}
n-Pentane	0.33	0.26	0.08	1.57×10^{3}	1.31	9.99×10^{3}
o-Xylene	0.00	0.00	0.00	0.00	0.00	0.00
Toluene	0.47	0.00	0.00	0.00	0.00	0.00

2.5.3 Calibration of the Free Swelling Behavior

To obtain the polymer-solvent interaction parameter χ, we calibrate the constitutive model to the free swelling data. Following (2.30), and using the experimentally determined swelling stretch found in Subsection 2.3.7, along with the material parameters from Table 2.4, we obtain the χ values for each polymer-solvent combination. The values obtained through calibration are found in Table 2.6.

Table 2.6 Measured Equilibrium Free Swelling Stretch, and the Calibrated Polymer-Solvent Interaction Parameter χ for VHB 4910 in Various Solvents.

	n-Pentane	o-Xylene	Toluene
λ^s	1.49	1.95	1.98
χ	0.631	0.550	0.548

2.5.4 Model Summary

The values obtained by calibrating the model for the time-independent behavior display the change in the scaling exponent q with the solvent uptake, while keeping

both the initial shear model G_0 and locking stretch λ_L fixed. That allows for the constitutive model to reduce back to the same material when dry, while the scaling exponent q originally proposed by [100] accounts for the measured change in the effective stiffness due to solvent. Also, as expected, the polymer-solvent interaction parameter χ regulates the degree of swelling, such that as χ decreases the degree of swelling increases.

Calibration of the time-dependent behavior of virgin samples, show utilization of all viscous mechanisms. The calibrated parameters for samples fully swollen with n-Pentane show a very low utilization of viscous mechanisms, since the $G_{\text{TD}}^{(\gamma)}$ is at least an order of magnitude lower than those obtained from virgin samples. Additionally, in contrast to the values obtained from the time-dependent calibration of the virgin behavior, for samples fully swollen with o-Xylene and Toluene, we find that $G_{\text{TD}}^{(\gamma)} \approx 0$, making all the viscous mechanism insignificant. Further, the relaxation times for all viscous mechanisms $\tau^{(\gamma)} \approx 0$ when fully swollen in these two solvents, reflecting the apparent instantaneous relaxation of fully swollen VHB 4910. Thus, our constitutive model proved capable of accounting for the apparent vanishing of rate-dependence, hysteresis and stress relaxation behavior of viscoelastic polymeric gels.

2.6 Concluding Remarks

In this research, we have characterized the viscoelastic response of both dry and fully swollen gels through experimental observations and continuum level modeling. Using VHB 4910 along with three different solvents, n-Pentane, o-Xylene and Toluene, we have measured the mechanical response in (i) quasi-static uniaxial large deformation tension, (ii) uniaxial load-unload at multiple rates, and (iii) stress relaxation; when virgin, fully swollen, and solvent cycled. The most notable result of these experiments being the apparent loss of viscoelasticity in the response due to the uptake of solvent.

Additionally, through solvent cycling, our measurements show the reappearance of viscoelasticity, suggesting the process is reversible.

In addition, we have developed a continuum-level constitutive model for viscoelastic polymeric gels. Our model is successfully calibrated against the obtained experimental data, thus proving capable to replicate the major features of viscoelastic gel behavior observed in our experiments. The calibration of our constitutive model showed (i) low utilization of the time-dependent stress contribution for the samples fully swollen in n-Pentane; (ii) almost complete absence of the time-dependent stress contribution for samples fully swollen with o-Xylene and Toluene.

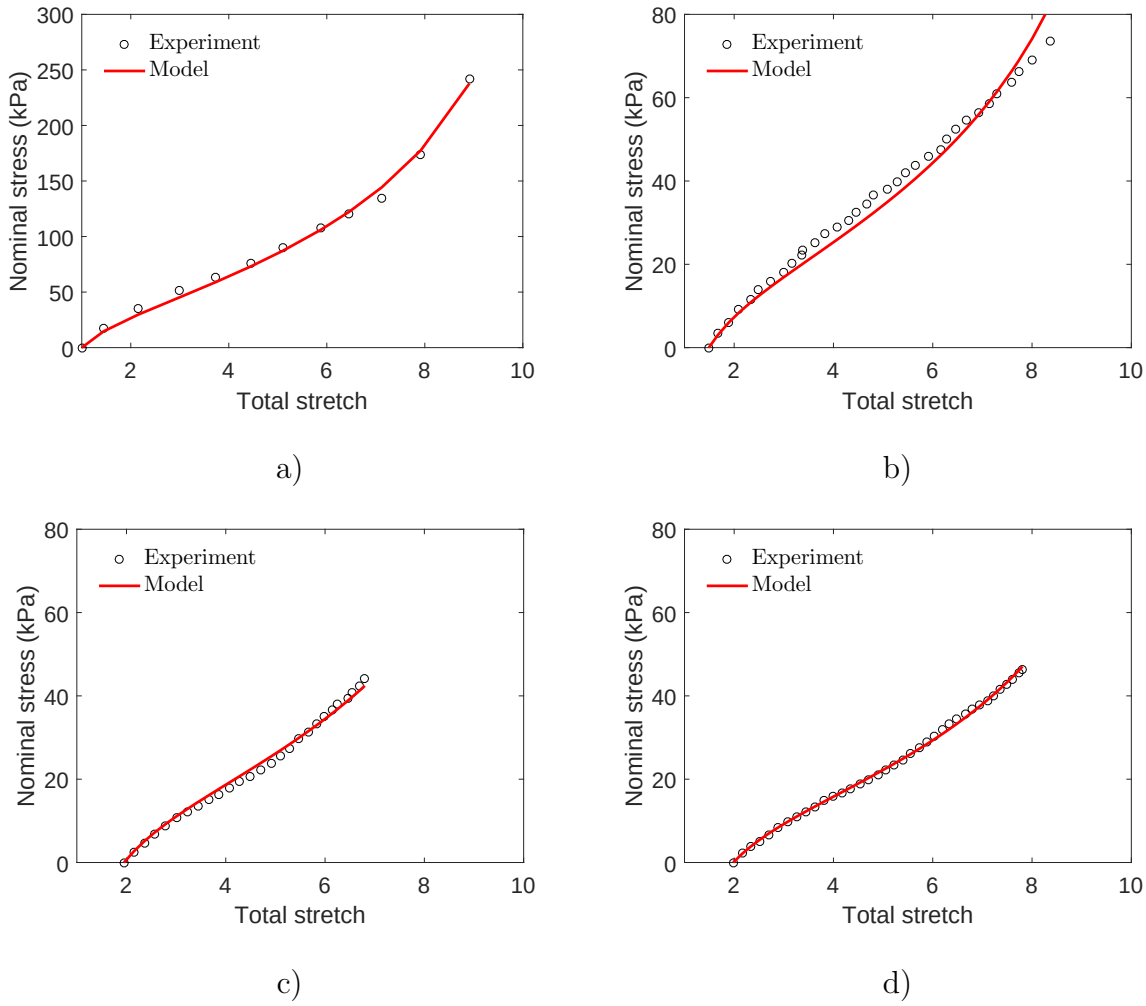

Figure 2.16 Calibration of the time-independent behavior for VHB 4910 when (a) virgin, and and fully swollen with (b) n-Pentane, (c) o-Xylene and (d) Toluene. Here, G_0 and λ_L is obtained from virgin calibration and it's held constant throughout. The model is then calibrated for q against the fully swollen data.

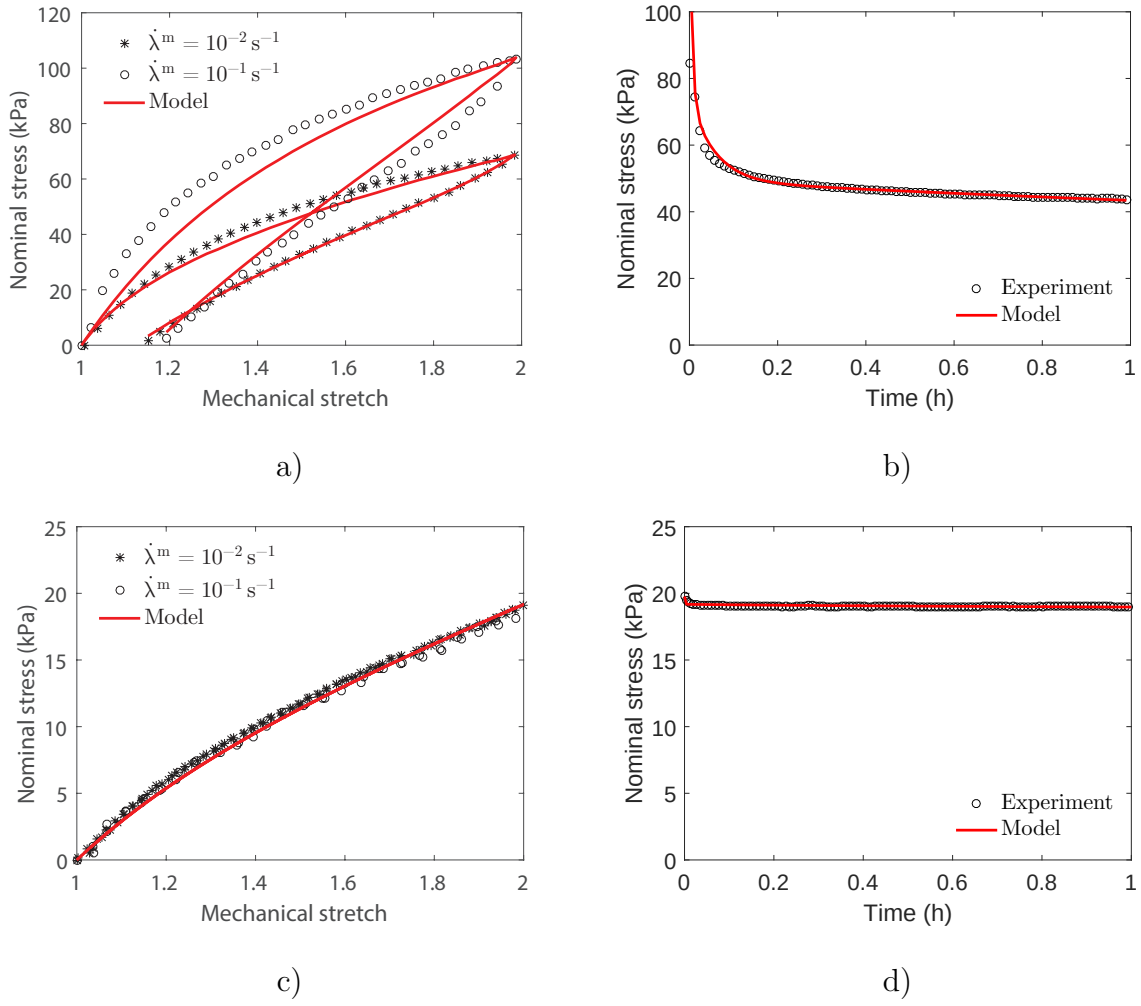

Figure 2.17 Calibration of the time-dependent behavior for VHB 4910: a) and b) are virgin ; c) and d) fully swollen with n-Pentane.

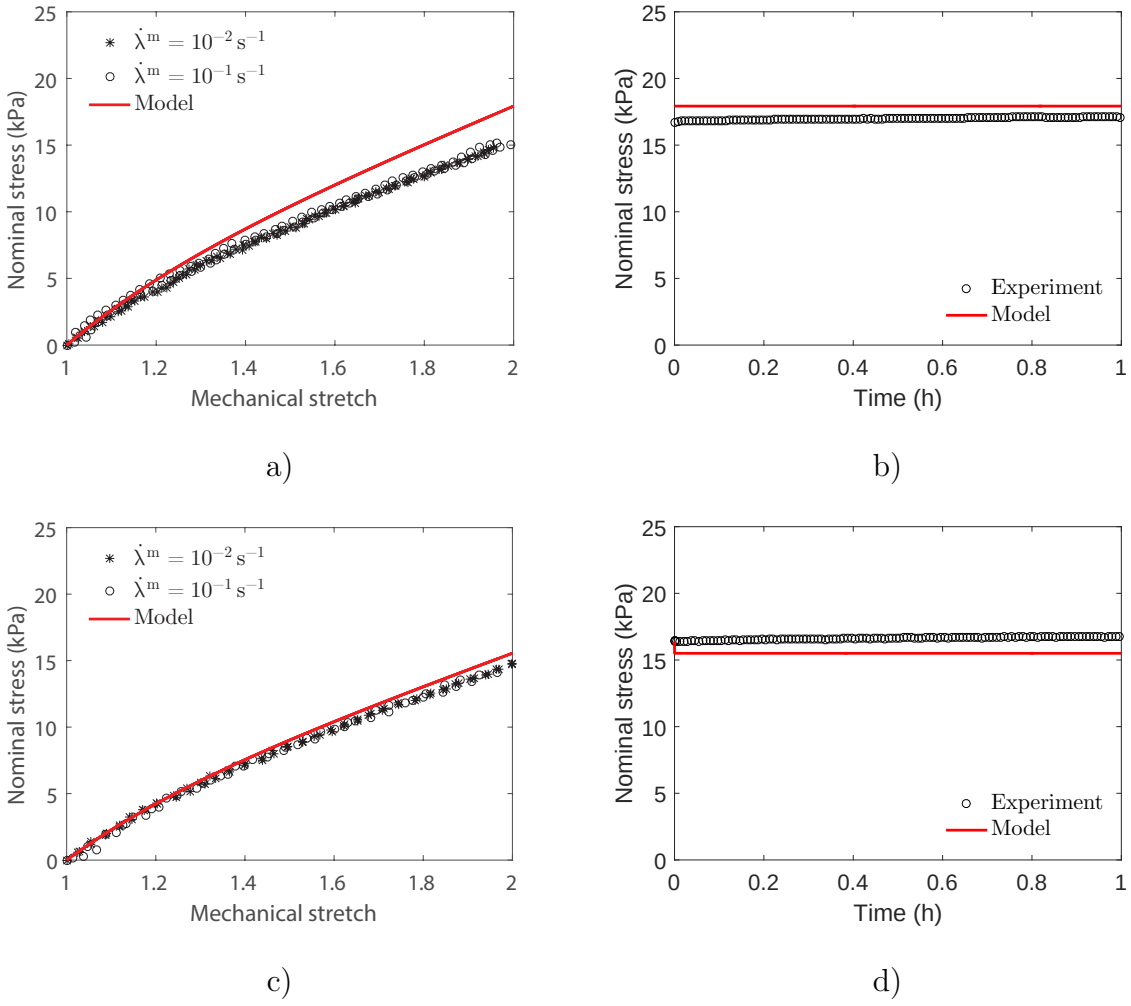

Figure 2.18 Calibration of the time-dependent behavior for VHB 4910: a) and b) fully swollen with o-Xylene; c) and d) fully swollen with Toluene.

CHAPTER 3

FIBER-REINFORCED POLYMERIC GELS

3.1 Introduction

The objective of the work presented in this chapter is to develop a continuum level coupled deformation-diffusion constitutive model for fiber-reinforced polymeric gels. The novelty of the model is that it builds upon previous work by taking into account the mechanical influence of fibers, as well as the anisotropic diffusion they may impart. The behavior of the dry polymer matrix is modeled using a non-Gaussian statistical mechanics based model that takes limited chain extensibility into account. In addition to the behavior of dry polymer matrix, we include the contribution of embedded fibers with a volume fraction and modulus. The mechanical behavior of polymer network is coupled with the diffusion of solvent by implementing Flory-Huggins model for mixing free energy between polymer network and solvent. We assume the embedded fibers do not imbibe solvent, and accordingly there is no mixing between the fiber and solvent. Further, we numerically implemented our multiphysics constitutive model in commercially available finite element software package [1] by writing a user element subroutine (UEL). The numerical implementation allows for the behavior and capabilities of the model to be presented through boundary value problems. Lastly, to show the usefulness of the model and it's implementation, a qualitative comparison is made between the model and an experimentally realized soft robotic gripper.

The remainder of this chapter is organized as follows. Section 3.2 summarizes the continuum level framework, in Section 3.3 we presented the overview of thermodynamics of the system, in Section 3.4 we provide basic constitutive equations and in Section 3.5 we show the specialization of free energy for fiber-reinforced polymeric gels. Section 3.7 shows the usefulness of our constitutive model and

numerical simulation procedure. In Section 3.8 we show a comparison between the operation of our diffusion activated soft gripper and its numerical simulation. We finish with some concluding remarks in Section 4.9. In the Appendix C, we present the governing equations and the numerical solution procedure using finite elements required for numerical implementation.

3.2 Continuum Framework

We begin by summarizing the governing continuum level equations for coupled solvent diffusion and large deformation of soft polymeric gels. For further details, the reader is referred to our previous work in the literature (cf., e.g., [18]).

3.2.1 Kinematics

Consider a *dry* body $\mathcal{B}_{\mathrm{R}}$ identified with the region of space it occupies in a fixed reference configuration, and denote by $\mathbf{x}_{\mathrm{R}}$ an arbitrary material point of $\mathcal{B}_{\mathrm{R}}$. The dry referential body $\mathcal{B}_{\mathrm{R}}$ then undergoes a motion $\mathbf{x} = \boldsymbol{\chi}(\mathbf{x}_{\mathrm{R}}, t)$ to the deformed body $\mathcal{B}_t$ with deformation gradient given by[1]

$$\mathbf{F} = \nabla\boldsymbol{\chi}, \text{ such that } J = \det\mathbf{F} > 0. \tag{3.1}$$

The right and left Cauchy-Green deformation tensors are given by $\mathbf{C} = \mathbf{F}^{\top}\mathbf{F}$ and $\mathbf{B} = \mathbf{F}\mathbf{F}^{\top}$, respectively. Additionally, to model the fibers, we assume γ different fiber orientations may be present in the dry reference body, denoted by the term *family*. Each fiber family is characterized by a direction $\mathbf{a}_{\mathrm{R}}^{(\gamma)}$ (a unit vector), and volume fraction $f_{\mathrm{R}}^{(\gamma)}$ in $\mathcal{B}_{\mathrm{R}}$. *At the outset, we assume that the fibers do not absorb any solvent and remain dry, and are perfectly bonded to the polymer matrix.* Following the approach in [56], a pseudo-invariant is introduced for each family of fibers, which as

[1]The symbols ∇, Div and Curl denote the gradient, divergence and curl with respect to the material point $\mathbf{x}_{\mathrm{R}}$ in the reference configuration; grad, div and curl denote these operators with respect to the point $\mathbf{x} = \boldsymbol{\chi}(\mathbf{x}_{\mathrm{R}}, t)$ in the deformed configuration.

previously noted has been used to model the anisotropic response of fiber-reinforced soft materials [137, 95, 96]. Specifically, we use the pseudo-invariant

$$I_4^{(\gamma)} = \mathbf{a}_{\mathrm{R}}^{(\gamma)} \cdot \mathbf{C}\mathbf{a}_{\mathrm{R}}^{(\gamma)} = \left(\lambda^{(\gamma)}\right)^2 , \tag{3.2}$$

where $\lambda^{(\gamma)}$ has the physical interpretation of the stretch along the fiber family direction $\mathbf{a}_{\mathrm{R}}^{(\gamma)}$ for each γ.

The theory is based upon a multiplicative decomposition

$$\mathbf{F} = \mathbf{F}^m\mathbf{F}^s, \text{ with } \mathbf{F}^s = \lambda^s\mathbf{1}, \tag{3.3}$$

of the deformation gradient $\mathbf{F}$ into a mechanical part, $\mathbf{F}^m$, and a swelling part $\mathbf{F}^s$, with λ^s the swelling stretch. Further, this allows us to rewrite the right Cauchy-Green tensor in the form

$$\mathbf{C} = \left(\mathbf{F}^m\mathbf{F}^s\right)^\top \left(\mathbf{F}^m\mathbf{F}^s\right) = \left(\lambda^s\right)^2 \mathbf{F}^{m\top}\mathbf{F}^m = \left(\lambda^s\right)^2 \mathbf{C}^m . \tag{3.4}$$

Based on (3.3), the relative volume change is given by

$$J = \det \mathbf{F} = \det\left(\mathbf{F}^m\mathbf{F}^s\right) = J^m J^s, \text{ with} \det \mathbf{F}^m = J^m > 0, \text{ and } \det \mathbf{F}^s = J^s > 0 , \tag{3.5}$$

where J^m is the volume change due to mechanical effects, and J^s the volume change due to swelling. As is typical in the literature [58, 16] we assume the volume change due to swelling is given by

$$J^s = 1 + \Omega c_{\mathrm{R}}, \quad \text{and therefore} \quad \lambda^s = \left(1 + \Omega c_{\mathrm{R}}\right)^{1/3} . \tag{3.6}$$

Here c_{R} represents the *solvent content* measured in moles of solvent per unit reference volume of the dry polymer, and Ω the volume of a mole of solvent.

Further, using (3.1) and (3.3), we write velocity gradient

$$\mathbf{L} = \dot{\mathbf{F}}\mathbf{F}^{-1} = \mathbf{L}^m + \mathbf{F}^m\mathbf{L}^s\mathbf{F}^{m-1} \tag{3.7}$$

with $\mathbf{L}^m$ and $\mathbf{L}^s$, mechanical and swelling part, respectively, given by

$$\mathbf{L}^m = \dot{\mathbf{F}}^m \mathbf{F}^{m-1} \quad \text{and} \quad \mathbf{L}^s = \dot{\mathbf{F}}^s \mathbf{F}^{s-1}\,. \tag{3.8}$$

Next, we define the mechanical and swelling stretching and spin tensors

$$\begin{aligned} \mathbf{D}^m &= \operatorname{sym} \mathbf{L}^m, \quad \mathbf{W}^m = \operatorname{skw} \mathbf{L}^m, \\ \mathbf{D}^s &= \operatorname{sym} \mathbf{L}^s, \quad \mathbf{W}^s = \operatorname{skw} \mathbf{L}^s, \end{aligned} \tag{3.9}$$

so that $\mathbf{L}^m = \mathbf{D}^m + \mathbf{W}^m$ and $\mathbf{L}^s = \mathbf{D}^s + \mathbf{W}^s$.

Recalling (3.3), (3.8) and (3.9) we obtain

$$\mathbf{D}^s = \left(\dot{\lambda}^s \lambda^{s-1}\right) \mathbf{1} \quad \text{and} \quad \mathbf{W}^s = \mathbf{0}\,, \tag{3.10}$$

and since

$$\dot{J}^s = J^s \operatorname{tr} \mathbf{D}^s, \tag{3.11}$$

we may write

$$\mathbf{D}^s = \frac{1}{3}\left(\dot{J}^s J^{s-1}\right) \mathbf{1}. \tag{3.12}$$

3.2.2 Balance of Forces and Moments

Neglecting inertial effects, the balance of forces and moments in the referential body $\mathcal{B}_{\mathrm{R}}$ are expressed as

$$\operatorname{div} \mathbf{T}_{\mathrm{R}} + \mathbf{b}_{\mathrm{R}} = \mathbf{0} \quad \text{and} \quad \mathbf{T}_{\mathrm{R}} \mathbf{F}^{\top} = \mathbf{F} \mathbf{T}_{\mathrm{R}}^{\top} \tag{3.13}$$

respectively, where $\mathbf{T}_{\mathrm{R}}$ is first Piola stress and $\mathbf{b}_{\mathrm{R}}$ is an external body force per unit referential volume. The boundary of the referential body has outward unit normal $\mathbf{n}_{\mathrm{R}}$. The surface traction on an element of the referential surface is given by $\mathbf{t}_{\mathrm{R}} = \mathbf{T}_{\mathrm{R}} \mathbf{n}_{\mathrm{R}}$. As common in continuum mechanics, the Piola stress is related to Cauchy stress $\mathbf{T}$

in the deformed body by

$$\mathbf{T}_{\mathrm{R}} = J\mathbf{T}\mathbf{F}^{-\top}, \quad \text{therefore,} \quad \mathbf{T} = J^{-1}\mathbf{T}_{\mathrm{R}}\mathbf{F}^{\top}. \tag{3.14}$$

In the current configuration the balance of forces and moments is given in the deformed body $\mathcal{B}_t$ by

$$\operatorname{div}\mathbf{T} + \mathbf{b} = \mathbf{0} \quad \text{and} \quad \mathbf{T} = \mathbf{T}^{\top}, \tag{3.15}$$

where $\mathbf{b}$ is the external body force per unit current volume. Lastly, the surface traction on the boundary of deformed body with outward unit normal $\mathbf{n}$ is $\mathbf{t} = \mathbf{T}\mathbf{n}$.

3.2.3 Balance of Solvent Content

We assume that the intake and outflow of solvent does not involve any chemical reactions. Therefore, the balance of solvent content in the referential and current configurations takes the form

$$\dot{c}_{\mathrm{R}} = -\operatorname{Div}\mathbf{j}_{\mathrm{R}} \quad \text{and} \quad \dot{c}_{\mathrm{R}} = -J\operatorname{div}\mathbf{j}, \tag{3.16}$$

where $\mathbf{j}_{\mathrm{R}}$ and $\mathbf{j}$ are the fluid flux in referential and current configuration, respectively.

Defining the *polymer volume fraction*

$$\phi \overset{\text{def}}{=} \frac{1}{1 + \Omega c_{\mathrm{R}}} = (\lambda^s)^{-3} = (J^s)^{-1} \tag{3.17}$$

which lies in the range $0 < \phi < 1$, the balance of solvent content (3.16) may be rewritten in the referential and current forms

$$\frac{\dot{\phi}}{\Omega\phi^2} - \operatorname{Div}\mathbf{j}_{\mathrm{R}} = 0 \quad \text{and} \quad \frac{\dot{\phi}}{J\Omega\phi^2} - \operatorname{div}\mathbf{j} = 0. \tag{3.18}$$

Here $\phi \to 1$ is simply a dry polymer, while $\phi < 1$ is a locally swollen state. Lastly, the surface flux into an element of the referential and current surface is given by $j_{\mathrm{R}} = -\mathbf{j}_{\mathrm{R}} \cdot \mathbf{n}_{\mathrm{R}}$ and $j = -\mathbf{j} \cdot \mathbf{n}$, respectively.

3.3 Thermodynamics

A complete thermodynamic derivation of a model for polymeric gels is thoroughly discussed in the earlier research published by our group. For more details regarding thermodynamics, the reader is referred to [16, 17, 15].

Let the body $\mathcal{B}_{\mathrm{R}}$ contain an arbitrary part $\mathcal{P}_{\mathrm{R}}$. Under isothermal conditions, the first two laws of thermodynamics may be combined into a single free energy imbalance. The free energy imbalance requires that the temporal increase in free energy in any part be less than or equal to the power expended plus that which is brought into that part from fluid transport. Specifically the free energy imbalance takes the form

$$\dot{\overline{\int_{\mathcal{P}_{\mathrm{R}}} \psi_{\mathrm{R}} dv_{\mathrm{R}}}} \leq \int_{\partial\mathcal{P}_{\mathrm{R}}} \mathbf{T}_{\mathrm{R}}\mathbf{n}_{\mathrm{R}} \cdot \dot{\boldsymbol{\chi}} da_{\mathrm{R}} + \int_{\mathcal{P}_{\mathrm{R}}} \mathbf{b}_{\mathrm{R}} \cdot \dot{\boldsymbol{\chi}} dv_{\mathrm{R}} - \int_{\partial\mathcal{P}_{\mathrm{R}}} \mu \mathbf{j}_{\mathrm{R}} \cdot \mathbf{n}_{\mathrm{R}} da_{\mathrm{R}} \,, \tag{3.19}$$

with μ the chemical potential of the solvent. Applying the divergence theorem to the terms in (3.19), we obtain

$$\int_{\mathcal{P}_{\mathrm{R}}} \big(\dot{\psi}_{\mathrm{R}} - (\mathrm{Div}\,\mathbf{T}_{\mathrm{R}} + \mathbf{b}_{\mathrm{R}}) \cdot \dot{\chi} - \mathbf{T}_{\mathrm{R}} : \dot{\mathbf{F}} + \mu \mathrm{Div}\mathbf{j}_{\mathrm{R}} + \mathbf{j}_{\mathrm{R}} \cdot \nabla\mu\big) dv_{\mathrm{R}} \leq 0 \,. \tag{3.20}$$

Using (3.13) and (3.16), since (3.20) must hold for every part $\mathcal{P}_{\mathrm{R}}$, we write

$$\dot{\psi}_{\mathrm{R}} - \mathbf{T}_{\mathrm{R}} : \dot{\mathbf{F}} - \mu \dot{c}_{\mathrm{R}} + \mathbf{j}_{\mathrm{R}} \cdot \nabla\mu \leq 0 \,. \tag{3.21}$$

Recalling (3.3) and (3.8), we decompose the stress power

$$\mathbf{T}_{\mathrm{R}} : \dot{\mathbf{F}} = \big(J\mathbf{T}\mathbf{F}^{m-\top}\big) : \dot{\mathbf{F}}^{m} + \big(J\mathbf{F}^{m\top}\mathbf{T}\mathbf{F}^{m-\top}\big) : \mathbf{L}^{s} \,. \tag{3.22}$$

Here, we introduce two new stress measures

$$\mathbf{S}^{m} \stackrel{\mathrm{def}}{=} J\mathbf{T}\mathbf{F}^{m-\top} \quad \text{and} \quad \mathbf{M}^{m} \stackrel{\mathrm{def}}{=} J\mathbf{F}^{m\top}\mathbf{T}\mathbf{F}^{m-\top} \,, \tag{3.23}$$

as a mechanical Piola stress and Mandell stress, respectively. Further, using (3.23), we can write (3.22) in the form

$$\mathbf{T}_{\mathrm{R}} : \dot{\mathbf{F}} = \mathbf{S}^m : \dot{\mathbf{F}}^m + \mathbf{M}^m : \mathbf{L}^s \tag{3.24}$$

In addition, we introduce mechanical second Piola stress

$$\mathbf{T}^m = J\mathbf{F}^{m-1}\mathbf{T}\mathbf{F}^{m-\top} \tag{3.25}$$

and since the rate of change of mechanical right Cauchy-Green tensor is $\dot{\mathbf{C}}^m = \mathbf{F}^{m\top}\dot{\mathbf{F}}^m + \dot{\mathbf{F}}^{m\top}\mathbf{F}^m$, we can write

$$\mathbf{T}^m : \dot{\mathbf{C}}^m = 2\left(\mathbf{F}^m\mathbf{T}^m\right) : \dot{\mathbf{F}}^m = 2\mathbf{S}^m : \dot{\mathbf{F}}^m. \tag{3.26}$$

Employing (3.10) and (3.12) we can write the stress-power (3.22) in the form

$$\mathbf{T}_{\mathrm{R}} : \dot{\mathbf{F}} = \frac{1}{2}\mathbf{T}^m : \dot{\mathbf{C}}^m - \overline{p}J^s, \tag{3.27}$$

where we have defined the mean normal pressure, $\bar{p}$, as $\bar{p} \overset{\text{def}}{=} -\frac{1}{3}J^m \mathrm{tr}\,\mathbf{T}$.

Applying the kinematical constraint between c_{R} and J^s given by (3.6), in (3.19), and using (3.27), we obtain the free energy imbalance in the form

$$\dot{\psi}_{\mathrm{R}} - \frac{1}{2}\mathbf{T}^m : \dot{\mathbf{C}}^m - \mu_{\mathrm{act}}c_{\mathrm{R}} + \mathbf{j}_{\mathrm{R}} \cdot \nabla\mu \leq 0\,, \tag{3.28}$$

where the active chemical potential is defined as $\mu_{\mathrm{act}} \overset{\text{def}}{=} \mu - \bar{p}\Omega$.

3.4 Basic Constitutive Equations

Based on (3.28), and considering frame indifference, the basic constitutive equations are

$$\left.\begin{aligned} \psi_{\mathrm{R}} &= \bar{\psi}_{\mathrm{R}}\left(\mathbf{C}^m, c_{\mathrm{R}}\right) \\ \mathbf{T}^m &= \bar{\mathbf{T}}^m\left(\mathbf{C}^m, c_{\mathrm{R}}\right) \\ \mu_{act} &= \bar{\mu}_{act}\left(\mathbf{C}^m, c_{\mathrm{R}}\right) \end{aligned}\right\} \tag{3.29}$$

along with a Darcy-type relation for the spatial solvent flux

$$\mathbf{j} = -\bar{\mathbf{M}}(\mathbf{C}^m, c_{\mathrm{R}})\mathrm{grad}\,\mu\,, \tag{3.30}$$

where $\bar{\mathbf{M}}(\mathbf{C}^m, c_{\mathrm{R}})$ is the mobility tensor. Here, to account for any anisotropy due to the embedded fibers, or other sources of anisotropy, the mobility retains it's tensorial characteristic, and not simplified to a scalar in this work. Pushed back to the reference body, using the standard relations $\mathbf{j}_{\mathrm{R}} = J\mathbf{F}^{-1}\mathbf{j}$ and $\nabla\mu = \mathbf{F}^{\top}\mathrm{grad}\,\mu$, we may rewrite (3.30) in the referential form

$$\mathbf{j}_{\mathrm{R}} = -J\mathbf{F}^{-1}\bar{\mathbf{M}}(\mathbf{C}^m, c_{\mathrm{R}})\mathbf{F}^{-\top}\nabla\mu\,. \tag{3.31}$$

Sufficient conditions to satisfy (3.28) using (3.29) yield relations for the Cauchy stress

$$\mathbf{T} = J^{-1}\Big[2\mathbf{F}^m\frac{\partial\bar{\psi}_{\mathrm{R}}(\mathbf{C}^m, c_{\mathrm{R}})}{\partial\mathbf{C}^m}\mathbf{F}^{m\top}\Big]\,, \tag{3.32}$$

and the chemical potential

$$\mu = \frac{\partial\bar{\psi}_{\mathrm{R}}(\mathbf{C}^m, c_{\mathrm{R}})}{\partial c_{\mathrm{R}}} + \Omega\bar{p}\,. \tag{3.33}$$

We further note that to satisfy the thermodynamic imbalance in (3.28), the mobility tensor $\bar{\mathbf{M}}(\mathbf{C}^m, c_{\mathrm{R}})$ has to be positive definite in the presence of solvent and whenever $\nabla\mu \neq \mathbf{0}$.

3.5 Specialized Constitutive Equations

3.5.1 Free Energy

For ease of notation, and following the approach used to include the fiber volume fraction in [104], we define

$$f_{\mathrm{R}} = \sum_{\gamma} f_{\mathrm{R}}^{(\gamma)} \tag{3.34}$$

such that f_{R} is the sum of the volume fractions of all families of fibers in $\mathcal{B}_{\text{R}}$, and therefore $(1 - f_{\text{R}})$ is the total volume fraction of swellable polymer matrix in $\mathcal{B}_{\text{R}}$. Next, we assume total free energy of the system to be additively decomposed

$$\psi_{\text{R}} = (1 - f_{\text{R}})\, \psi_{\text{R}}^{\text{matrix}} + (1 - f_{\text{R}}) \psi_{\text{R}}^{\text{mixing}} + \sum_{\gamma} f_{\text{R}}^{(\gamma)} \psi_{\text{R}}^{(\gamma),\text{fiber}}\,, \tag{3.35}$$

where $\psi_{\text{R}}^{\text{matrix}}$ is the free energy of polymer matrix, $\psi_{\text{R}}^{\text{mixing}}$ is the free energy of mixing between polymer matrix and solvent, and $\psi_{\text{R}}^{(\gamma),\text{fiber}}$ is the free energy of each fiber family.

Mechanical Free Energy of the Polymer Matrix Following the literature and using (3.6), we define the effective stretch, $\bar{\lambda}$, which includes both mechanical and swelling deformation, as

$$\bar{\lambda} \overset{\text{def}}{=} \sqrt{\frac{1}{3}\text{tr}\,\mathbf{C}} = \frac{1}{\sqrt{3}}\,(1 + \Omega c_{\text{R}})^{1/3}\,\sqrt{\text{tr}\,\mathbf{C}^m}. \tag{3.36}$$

For capturing the mechanical behavior of the polymer matrix, we use a non-Gaussian statistical mechanics based model [5, 3], which takes into account limited extensibility of polymer chains (also known as locking),

$$\begin{aligned}\psi_{\text{R}}^{\text{matrix}} = G_0 \lambda_L^2 \Big[\Big(\frac{\bar{\lambda}}{\lambda_L}\Big)\beta + \ln\Big(\frac{\beta}{\sinh\beta}\Big) - \Big(\frac{1}{\lambda_L}\Big)\beta_0 - \ln\Big(\frac{\beta_0}{\sinh\beta_0}\Big)\Big] \\ - G_0 \left(\frac{\lambda_L}{3}\ln J\beta_0\right) + J^s \left[\frac{1}{2} K \ln J^m\right]\,,\end{aligned} \tag{3.37}$$

with $\beta = \mathcal{L}^{-1}\Big(\frac{\bar{\lambda}}{\lambda_L}\Big)$ and $\beta_0 = \mathcal{L}^{-1}\Big(\frac{1}{\lambda_L}\Big)$, where $\mathcal{L}^{-1}$ is the inverse of the Langevin function $\mathcal{L}(\bullet) = \coth(\bullet) - (\bullet)^{-1}$. This form of mechanical free energy includes two material parameters, the initial shear modulus G_0, and the locking stretch λ_L. The locking stretch λ_L has the physical interpretation of the limiting value of the effective stretch $\bar{\lambda}$, when the chains are fully extended.

Mixing Free Energy For our estimate of mixing free energy, we implement the well known Flory-Huggins model [43, 64] which takes into account mixing of solvent molecules and the polymer matrix in the form

$$\psi_{\mathrm{R}}^{\mathrm{mixing}} = \mu^0 c_{\mathrm{R}} + R\vartheta c_{\mathrm{R}} \left(\ln\Big(\frac{\Omega c_{\mathrm{R}}}{1+\Omega c_{\mathrm{R}}}\Big) + \chi\Big(\frac{1}{1+\Omega c_{\mathrm{R}}}\Big)\right). \tag{3.38}$$

Here, μ^0 is a reference chemical potential, R is the gas constant, ϑ is absolute temperature, and χ is a dimensionless polymer-solvent interaction parameter.

Mechanical Free Energy for the Fibers To account for mechanical free energy for the embedded fibers, we adopt the form found in [56] which is also used in [95]. Following the approach discussed in Subsection 3.2.1, the contribution due to the fibers is modeled using

$$\psi_{\mathrm{R}}^{(\gamma),\mathrm{fiber}} = \frac{1}{2} E^{(\gamma)} (I_4^{(\gamma)} - 1)^2 , \tag{3.39}$$

with $E^{(\gamma)}$ the fiber modulus for each fiber family γ. Also, recall that $I_4^{(\gamma)}$ defined in (3.2) includes the dependence on orientation. Thereby, we incorporate the influence of different fiber families, which may have a different fiber modulus and/or orientation, and volume fraction through $f_{\mathrm{R}}^{(\gamma)}$ as seen in (3.35).

Total Free Energy Combining the mechanical free energy of the polymer matrix (3.37), the mechanical free energy of the embedded fibers (3.39), along with the mixing free energy (3.38) into (3.35), we obtain the total free energy

$$\begin{aligned}\psi_{\mathrm{R}} = (1-f_{\mathrm{R}})\Bigg\{ & G_0\lambda_L^2\Big[\Big(\frac{\bar{\lambda}}{\lambda_L}\Big)\beta + \ln\Big(\frac{\beta}{\sinh\beta}\Big) - \Big(\frac{1}{\lambda_L}\Big)\beta_0 - \ln\Big(\frac{\beta_0}{\sinh\beta_0}\Big)\Big] \\ & - G_0\left(\frac{\lambda_L}{3}\ln J\beta_0\right) + \mu^0 c_{\mathrm{R}} + R\vartheta c_{\mathrm{R}}\left(\ln\Big(\frac{\Omega c_{\mathrm{R}}}{1+\Omega c_{\mathrm{R}}}\Big) + \chi\Big(\frac{1}{1+\Omega c_{\mathrm{R}}}\Big)\right) + J^s\left[\frac{1}{2}K\ln J^m\right]\Bigg\} \\ & + \sum_{\gamma} f_{\mathrm{R}}^{(\gamma)} \frac{1}{2} E^{(\gamma)} (I_4^{(\gamma)} - 1)^2 . \end{aligned} \tag{3.40}$$

3.5.2 Cauchy Stress

Following (3.32), and using (3.40), we obtain the Cauchy stress

$$\begin{aligned}\mathbf{T} &= J^{-1}\left(2\mathbf{F}^m\frac{\partial\bar{\psi}_{\mathrm{R}}(\mathbf{C}^m,c_{\mathrm{R}})}{\partial\mathbf{C}^m}\mathbf{F}^{m\top}\right)\\ &= J^{-1}\underbrace{(1-f_{\mathrm{R}})\left(G_0\left(\zeta\phi^{-2/3}\mathbf{B}^m-\zeta_0\mathbf{1}\right)+J^sK(\ln J^m)\mathbf{1}\right)}_{\text{contribution due to the polymer matrix}}\\ &+ J^{-1}\underbrace{\sum_{\gamma}2f_{\mathrm{R}}^{(\gamma)}E^{(\gamma)}(\lambda^s)^2(I_4^{(\gamma)}-1)\mathbf{F}^m(\mathbf{a}_{\mathrm{R}}^{(\gamma)}\otimes\mathbf{a}_{\mathrm{R}}^{(\gamma)})\mathbf{F}^{m\top}}_{\text{contribution due to the fibers}},\end{aligned}\tag{3.41}$$

with

$$\zeta\overset{\text{def}}{=}\Big(\frac{\lambda_L}{3\bar{\lambda}}\Big)\mathcal{L}^{-1}\Big(\frac{\bar{\lambda}}{\lambda_L}\Big)\text{ and }\zeta_0\overset{\text{def}}{=}\Big(\frac{\lambda_L}{3}\Big)\mathcal{L}^{-1}\Big(\frac{1}{\lambda_L}\Big).\tag{3.42}$$

From (3.41) it is clear that the volume fraction of embedded fibers $f_{\mathrm{R}}^{(\gamma)}$ determines the contribution of each constituent of the system. The influence of the polymer matrix to the Cauchy stress decreases with f_{R}, however, the importance of the embedded fibers increases with f_{R}. Further, the stiffness of the polymer matrix decreases with solvent concentration through terms related to ϕ. In addition, since there is no mixing between the solvent and the embedded fibers, the embedded fibers tend to constrain the swelling process. Lastly, it is worth noting that due to relations found in (3.3) and (3.2), the embedded fibers have an affect on both swelling and mechanical deformation.

3.5.3 Chemical Potential

Next, using (3.40) and (3.33), we obtain the chemical potential in the form

$$\begin{aligned}\mu &= \frac{\partial \psi_{\mathrm{R}}}{\partial c_{\mathrm{R}}} - \Omega \frac{1}{3} J^m \mathrm{tr}\,\mathbf{T} \\ &= \underbrace{(1-f_{\mathrm{R}})\left[\mu^0 + R\vartheta\Big(\ln(1-\phi) + \phi + \chi\phi^2\Big)\right]}_{\text{mixing contribution}} \\ &\underbrace{-(1-f_{\mathrm{R}})\left[\Omega K(\ln J^m) - \frac{1}{2}K\Omega(\ln J^m)^2\right]}_{\text{matrix ``mechanical'' contribution}} \\ &\underbrace{+f_{\mathrm{R}}\left[\frac{2}{3}E\Omega\,(1+\Omega c_{\mathrm{R}})\,I_4(I_4-1)\right]}_{\text{fiber ``mechanical'' contribution}}\,. \end{aligned} \tag{3.43}$$

Here, it can be observed that the chemical potential is not only affected by the mixing of polymer matrix and solvent, but also by the mechanical deformation of the fiber-reinforced polymeric gel. The mechanical pressure and its energy, along with the deformation of embedded fibers, contributes to the chemical potential of the system, thus fully coupling the mechanical and chemical aspects of gel behavior.

3.5.4 Mobility Tensor

The solvent mobility tensor, which takes into account any possible anisotropy in diffusion, is assumed to be temperature and concentration dependent, and is given in the form

$$\mathbf{M} = \mathbf{D}\frac{c}{R\vartheta} = \mathbf{D}\frac{c_{\mathrm{R}}}{JR\vartheta}\,, \tag{3.44}$$

where $\mathbf{D}$ and $c = J^{-1}c_{\mathrm{R}}$ represent the tensorial diffusivity and the solvent concentration per unit spatial volume, respectively. The tensorial form of the diffusivity allows for the inclusion of anisotropic diffusion response. In practice, it is generally more convenient to use ϕ in place of c since ϕ is bounded, $0 < \phi \leq 1$. Accordingly,

using (3.17) we rewrite (3.44) in the form

$$\mathbf{M} = \mathbf{D}\left(\frac{1-\phi}{R\vartheta J\Omega\phi}\right). \tag{3.45}$$

Also, as previously mentioned in Section 3.4, the mobility tensor $\mathbf{M}$ must be positive definite based on the free energy imbalance (3.28). As a further consequence, we take the diffusivity tensor $\mathbf{D}$ to be positive definite.

3.6 Numerical Implementation

In the absence of body forces and inertial effects, the governing partial differential equations, expressed in the deformed body $\mathcal{B}_t$, consist of the balance of forces and the balance of solvent content. The balance of forces yields

$$\operatorname{div}\mathbf{T} = \mathbf{0} \quad \text{in} \quad \mathcal{B}_t, \tag{3.46}$$

with the Cauchy stress $\mathbf{T}$ given by (3.41). And the balance of solvent content yields

$$\frac{\dot{\phi}}{J\Omega\phi^2} + \operatorname{div}\mathbf{j} = 0 \quad \text{in} \quad \mathcal{B}_t, \tag{3.47}$$

with the fluid flux $\mathbf{j}$ given by (3.30) and the mobility by (3.45). With the displacement denoted by $\mathbf{u}(\mathbf{x}, t)$, the mechanical boundary conditions on $\partial\mathcal{B}_t$ are given by

$$\mathbf{u} = \breve{\mathbf{u}} \quad \text{on} \quad \mathcal{S}_{\mathbf{u}}, \quad \text{and} \quad \mathbf{T}\mathbf{n} = \breve{\mathbf{t}} \quad \text{on} \quad \mathcal{S}_{\mathbf{t}}, \tag{3.48}$$

where $\breve{\mathbf{u}}$ and $\breve{\mathbf{t}}$ are the prescribed displacements and spatial surface tractions, respectively, and $\mathcal{S}_{\mathbf{u}}$ and $\mathcal{S}_{\mathbf{t}}$ are complementary subsurfaces of $\partial\mathcal{B}_t$. The chemical boundary conditions on $\partial\mathcal{B}_t$ are given by

$$\mu = \breve{\mu} \quad \text{on} \quad \mathcal{S}_{\mu}, \quad \text{and} \quad -\mathbf{j}\cdot\mathbf{n} = \breve{j} \quad \text{on} \quad \mathcal{S}_{\mathbf{j}}, \tag{3.49}$$

where $\breve{\mu}$ and $\breve{j}$ are the prescribed chemical potential and spatial surface flux, respectively, and $\mathcal{S}_{\mu}$ and $\mathcal{S}_{\mathbf{j}}$ are another set of complementary subsurfaces of $\partial\mathcal{B}_t$.

The initial conditions are taken as

$$\mathbf{u}(\mathbf{x}_{\mathrm{R}}, 0) = \mathbf{u}_0 \quad \text{and} \quad \mu(\mathbf{x}_{\mathrm{R}}, 0) = \mu_0 \quad \text{in} \quad \mathcal{B}_{\mathrm{R}}\,. \tag{3.50}$$

The coupled set of equations (3.46) and (3.47), along with the boundary conditions (3.48) and (3.49), and initial conditions (3.50), represents the strong form of the initial boundary value problem for the displacement field and the chemical potential field.

With $\mathbf{w}_1$ and w_2 denoting two weighting fields, the weak form of the boundary-value problem (3.46) through (3.49) is

$$\begin{cases} \displaystyle\int_{\mathcal{B}_t} \left(\mathbf{T} : \frac{\partial \mathbf{w}_1}{\partial \mathbf{x}} \right) dv = \int_{\mathcal{S}_{\mathbf{t}}} \left(\mathbf{w}_1 \cdot \breve{\mathbf{t}} \right) da, \\ \displaystyle\int_{\mathcal{B}_t} \left(\frac{w_2 \dot{\phi}}{J\Omega\phi^2} \right) dv = \int_{\mathcal{B}_t} \left(\mathbf{j} \cdot \frac{\partial w_2}{\partial \mathbf{x}} \right) dv + \int_{\mathcal{S}_\omega} \left(w_2 \breve{j} \right) da\,. \end{cases}$$

Following our previous work [17, 18], the deformed body is approximated using finite elements, $\mathcal{B}_t = \cup \mathcal{B}_t^{\mathrm{e}}$, and the nodal degrees of freedom are the displacement and the chemical potential, which are interpolated inside each element by

$$\mathbf{u} = \sum \mathbf{u}^A N^A \quad \text{and} \quad \mu = \sum \mu^A N^A, \tag{3.51}$$

with the index $A = 1, 2, \ldots$ denoting the nodes of the element, $\mathbf{u}^A$ and μ^A the nodal displacements and chemical potentials, and N^A the shape functions. Employing a standard Galerkin approach, in which the weighting fields $\mathbf{w}_1$ and w_2 are interpolated by the same shape functions, leads to the following element-level residuals

$$\left.\begin{aligned} (\mathbf{R}_{\mathbf{u}})^A &= -\int_{\mathcal{B}_t^e} \left(\mathbf{T} \frac{\partial N^A}{\partial \mathbf{x}} \right) dv + \int_{\mathcal{S}_{\mathbf{t}}^e} \left(N^A \breve{\mathbf{t}} \right) da, \\ (R_\mu)^A &= \int_{\mathcal{B}_t^e} \left(\frac{N^A \dot{\phi}}{J\Omega\phi^2} \right) dv + \int_{\mathcal{B}_t^e} \left(\mathbf{j} \cdot \frac{\partial N^A}{\partial \mathbf{x}} \right) dv \\ &\quad + \int_{\mathcal{S}_{\mathbf{j}}^e} \left(N^A \breve{j} \right) da. \end{aligned}\right\} \tag{3.52}$$

These element-level residuals are assembled into a global residual, which represents a non-linear system of equations for the nodal degrees of freedom.

Correspondingly, four element level tangents are required for the iterative Newton-Raphson solution procedure. The first tangent accounts for changes in the displacement residual with respect to the displacement, and is given by

$$K^{AB}_{u_i u_k} = -\frac{\partial R^A_{u_i}}{\partial u^B_k} = \int_{\mathcal{B}^e_t} \frac{\partial N^A}{\partial x_j} \mathbb{A}_{ijkl} \frac{\partial N^B}{\partial x_l} dv - \int_{\mathcal{S}^e_{\mathbf{t}}} N^A N^B \frac{\partial \breve{t}}{\partial u_k} da \,, \tag{3.53}$$

where the spatial tangent modulus $\mathbb{A}$ is related to the referential tangent modulus $\mathbb{A}_{\mathrm{R}}$ through

$$\mathbb{A}_{ijkl} = J^{-1} F_{jm} F_{ln} \left(\mathbb{A}_{\mathrm{R}}\right)_{imkn} \,, \tag{3.54}$$

and the referential tangent modulus is given by $\mathbb{A}_{\mathrm{R}} \overset{\text{def}}{=} \dfrac{\partial \mathbf{T}_{\mathrm{R}}}{\partial \mathbf{F}}$. And further,

$$K^{AB}_{u_i \mu} = -\frac{\partial R^A_{u_i}}{\partial \mu^B} = \int_{\mathcal{B}^e} \frac{\partial N^A}{\partial x_j} \Big(\frac{\partial T_{ij}}{\partial \phi} \frac{\partial \phi}{\partial \mu} \Big) N^B dv \,, \tag{3.55}$$

$$K^{AB}_{\mu u_k} = -\frac{\partial R^A_{\mu}}{\partial u^B_k} = -\int_{\mathcal{B}^e} \frac{\partial N^A}{\partial x_i} \Big(M_{il} \frac{\partial \mu}{\partial x_k} \Big) \frac{\partial N^B}{\partial x_l} dv \,, \tag{3.56}$$

and

$$K^{AB}_{\mu \mu} = -\frac{\partial R^A_{\mu}}{\partial \mu^B} = -\int_{\mathcal{B}^e} \frac{N^A N^B}{J \Omega \phi^2} \Big(2 \frac{\dot{\phi}}{\phi} \frac{\partial \phi}{\partial \mu} - \frac{\partial \dot{\phi}}{\partial \mu} \Big) dv - \int_{\mathcal{B}^e} \Big(\frac{\partial j_i}{\partial \mu} \frac{\partial N^A}{\partial x_i} \Big) dv - \int_{\mathcal{S}^e_{\mathbf{j}}} \Big(N^A N^B \frac{\partial \breve{j}}{\partial \mu} \Big) da \,. \tag{3.57}$$

Our finite-element procedures have been implemented in commercially available software package [1] using a user-element subroutine (UEL). We have developed a four-noded isoparametric quadrilateral plane-strain user-element, and an eight-noded continuum brick user-element. In order to avoid issues related to volumetric-locking, we utilize the F-bar method of [26] for fully-integrated elements. For complete details regarding the implementation of Abaqus user-element subroutines for multi-physics problems, readers are referred to [18].

Table 3.1 Material Parameters Used in the Numerical Simulations.

	Parameter	Value
Polymer Matrix	G_0	$1\,\mathrm{MPa}$
	K	$100\,\mathrm{MPa}$
	λ_L	10.0
Solvent	Ω	$1 \times 10^{-4}\,\mathrm{m}^3/\mathrm{mol}$
	μ^0	$0.0\,\mathrm{J/mol}$
Interaction	χ	0.2
Fibers	$E^{(\gamma)}$	$1\,\mathrm{GPa}$

3.7 Model Behavior Through Numerical Simulations

In this section, we present the capabilities of our anisotropic deformation-diffusion constitutive model for polymeric gels with embedded fibers by solving various boundary value problems. We note that details for the governing equations and finite element implementation are provided in an Appendix C. In this section, we consider both two dimensional plane strain swelling, and three-dimensional free swelling. Specifically, we consider an initial dry body with a square/cube shape having an edge length of 2 mm under a constant isothermal temperature of 298 K. In both cases the body is traction free, undergoing essentially free swelling; however, in plane strain the third dimension is constrained. The specific simulations that follow first probe the constitutive model when i) the diffusion is anisotropic without fibers, ii) a single family of fibers are present and the diffusion is isotropic, and lastly iii) when a single family of fibers and anisotropic diffusion are present. Specific values for the material parameters that remain unchanged across all the numerical simulations that follow are provided in Table 3.1.

3.7.1 Boundary Value Problem Setup

Here, we define the boundary value problem which will be solved to present the model behavior. Figure 3.1 shows both plane strain and three-dimensional situations. As shown in Figure 3.1, the body is symmetric, and therefore we only model 1/4 in plane strain, or 1/8 in three dimensions. We note that in all simulations that follow, fiber directions are chosen to maintain this symmetry throughout.

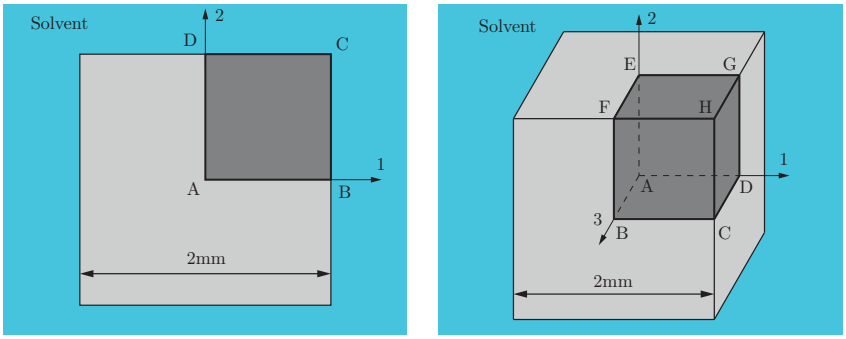

a) b)

Figure 3.1 Schematic of a initially dry 2 mm a) square and b) cube, immersed in solvent. For the numerical simulation, due to symmetry, we only mesh the portion of the body indicated in dark grey.

For these swelling simulations, the initial dry body is immersed into a solvent bath at a constant temperature of 298 K. With reference to Figure 3.1, the corresponding mechanical boundary conditions are:

- symmetry on all relevant planes — faces AB and AD in plane strain, and faces ABCD, ABEF, and ADGE in 3D;
- traction free on all other faces — faces BC and CD in plane strain, and faces BCHF, CDHG, and EFGH in 3D;

and the corresponding chemical boundary conditions are:

- no flux on all symmetry planes — faces AB and AD in plane strain, and faces ABCD, ABEF, and ADGE in 3D;

- a prescribed chemical potential $\breve{\mu}(t) = \mu^0 + \mu_0 \exp(-t/t_d)$ on faces in contact with solvent — faces BC and CD in plane strain, and faces BCHF, CDHG, and EFGH in 3D. Here $t_d = 200\,\mathrm{s}$ is a decay time used to apply the chemical potential boundary condition smoothly, and μ_0 is the initial chemical potential at time $t = 0$, obtained using (3.43).

3.7.2 Anisotropic Diffusion in the Absence of Fibers

To emphasize the affect that anisotropic diffusion has on the deformation, we simulate a polymeric gel without embedded fibers. Thus, we take $f_{\mathrm{R}} = 0$ and prescribe the diffusivity tensor in the form (referring to the coordinate basis as shown in Figure 3.1)

$$\begin{aligned} \mathbf{D} &= \begin{bmatrix} 10 & 0 \\ 0 & 1 \end{bmatrix} \times 10^{-9}\mathrm{m}^2/\mathrm{s} \quad \text{and} \\ \mathbf{D} &= \begin{bmatrix} 10 & 0 & 0 \\ 0 & 1 & 0 \\ 0 & 0 & 10 \end{bmatrix} \times 10^{-9}\mathrm{m}^2/\mathrm{s} \end{aligned} \tag{3.58}$$

for plane strain and 3D, respectively. For comparison, we show the results using an isotropic diffusivity, $\mathbf{D} = (1 \times 10^{-8}\mathbf{1})\,\mathrm{m}^2/\mathrm{s}$, with the same boundary conditions mentioned above.

Figure 3.2 shows contours of ϕ at a few snapshots in time for the isotropic and anisotropic simulations. The simulation results in Figure 3.2 show the clear difference between the behavior of the isotropic and anisotropic diffusivity in the deformation-diffusion behavior of the polymeric gel. The decreased diffusivity in the $\mathbf{e}_2$ direction leads to noticeably slower diffusion and corresponding swelling along that direction, leading to an observable anisotropy in the overall response of a gel.

However, as expected, after long times, where diffusion is no longer driving solvent at equilibrium, there is no difference between the isotropic and anisotropic results.

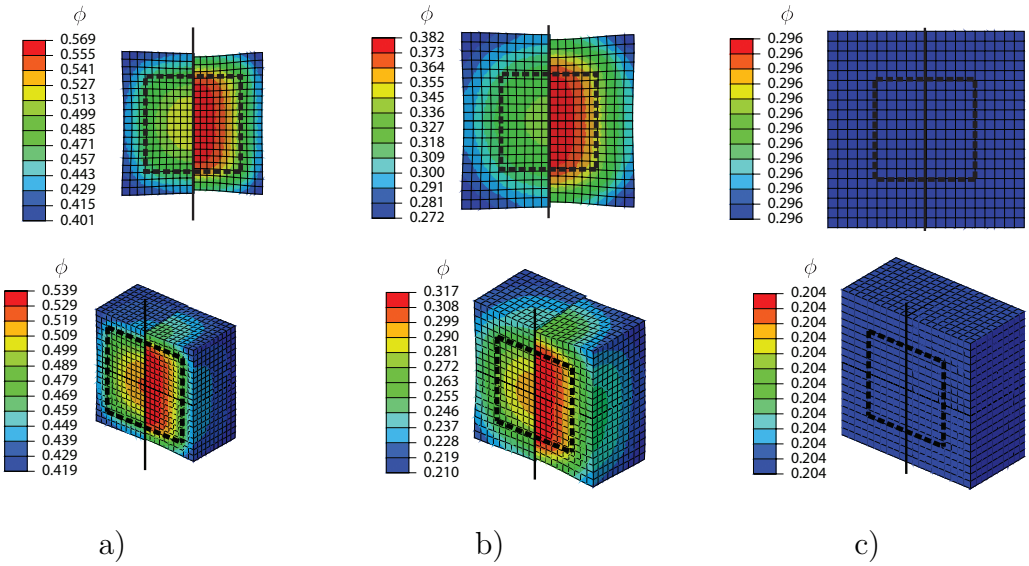

Figure 3.2 Simulation results showing ϕ at a) 900 s, b) 1800 s, and c) 6 hours, in plane strain (top) and 3D (bottom). In all cases, to help with comparison, the left portion is the isotropic simulation, while the right portion is anisotropic diffusion in the absence of fibers. Further, the thick dotted line indicates the initial dry body.

3.7.3 Isotropic Diffusion with Embedded Fibers

Next, we consider isotropic diffusion, but with the influence of embedded fibers. To observe the influence of the fiber volume fraction, we consider only a single fiber family with a fiber direction $\mathbf{a}_{\mathrm{R}} = \mathbf{e}_1$ (referring to the coordinate basis as shown in Figure 3.1), for both plane strain and three-dimensional simulations. For comparison, we show the results using an isotropic gel without any fibers, and, in all cases we take $\mathbf{D} = (1 \times 10^{-8}\mathbf{1})\,\mathrm{m}^2/\mathrm{s}$. Then, we vary the fiber volume fraction, choosing

$$f_{\mathrm{R}} = \{\, 1 \times 10^{-3},\, 5 \times 10^{-3},\, 1 \times 10^{-2},\, 5 \times 10^{-2},\, 1 \times 10^{-1} \}\,.$$

in the simulations that follow.

Figure 3.3 shows contours of ϕ at a few snapshots in time for the isotropic and anisotropic simulations with $f_{\mathrm{R}} = 1 \times 10^{-1}$. The results of numerical simulation in Figure 3.3 clearly show that, due to the constrained swelling caused by the embedded fibers, the swelling stretch along the fiber direction is significantly lower than that in the other directions. That difference is further quantified in Figure 3.4, where the stretch along the fiber direction $\lambda^{\parallel}$ decreases with the increase in fiber volume fraction. This is accompanied by an increase in the swelling stretch along the other directions, indicated by $\lambda^{\perp}$.

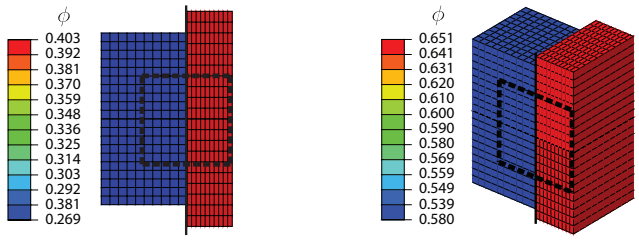

a) b)

Figure 3.3 Simulation results showing ϕ at 6 hours for a) plane strain, and b) 3D. In both cases, to help with comparison, the left portion is the isotropic simulation, while the right portion is anisotropic, with fiber direction $\mathbf{a}_{\mathrm{R}} = \mathbf{e}_1$ and volume fraction $f_{\mathrm{R}} = 10^{-1}$. Further, the thick dotted line indicates the initial dry body.

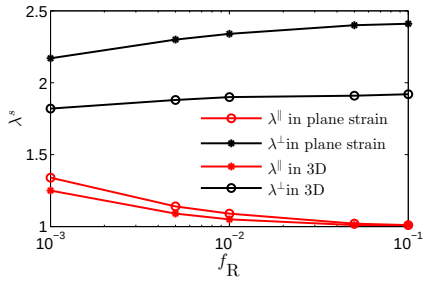

Figure 3.4 Simulation results showing the stretch along the fiber direction, $\lambda^{\parallel}$, and that perpendicular to it $\lambda^{\perp}$ near equilibrium at 6 hours for various fiber volume fractions.

3.7.4 Anisotropic Diffusion with Embedded Fibers

In this section, we perform simulations that include both embedded fibers and anisotropic diffusion. To keep results easy to interpret, we take a single fiber direction with $\mathbf{a}_{\text{R}} = \mathbf{e}_2$ at a volume fraction of $f_{\text{R}} = 1 \times 10^{-1}$, and assume the diffusivity to be (referring to the coordinate basis as shown in Figure 3.1)

$$\begin{aligned} \mathbf{D} &= \begin{bmatrix} 10 & 0 \\ 0 & 1 \end{bmatrix} \times 10^{-9}\text{m}^2/\text{s} \quad \text{and} \\ \mathbf{D} &= \begin{bmatrix} 10 & 0 & 0 \\ 0 & 1 & 0 \\ 0 & 0 & 10 \end{bmatrix} \times 10^{-9}\text{m}^2/\text{s} \end{aligned} \tag{3.59}$$

for plane strain and 3D, respectively. As previously mentioned, we assume the embedded fibers unable to swell, causing the solvent transport to be impeded along the fiber direction. Accordingly, we take the solvent diffusivity to be significantly slower in the direction of embedded fibers. Similar to the simulation results presented thus far, we again compare against an isotropic polymeric gel in the absence of embedded fibers, using an isotropic diffusivity $\mathbf{D} = (1 \times 10^{-8}\mathbf{1})\,\text{m}^2/\text{s}$.

Figure 3.5 shows contours of ϕ at a few snapshots in time for the isotropic and anisotropic simulations. The simulation results, under both plane stain and three-dimensional conditions, display pronounced anisotropy which is easily observed in Figure 3.5. Due to the combined influence of solvent diffusion anisotropy and the mechanical response of embedded fibers, the deformation is significantly constrained along the $\mathbf{e}_2$ direction, while the gel is allowed to freely swell in the other directions. Opposed to the example in Subsection 3.7.2, even when the equilibrium is reached, after 6 hours of free swelling there is a significant difference between isotropic and anisotropic simulations, due entirely to the presence of embedded fibers.

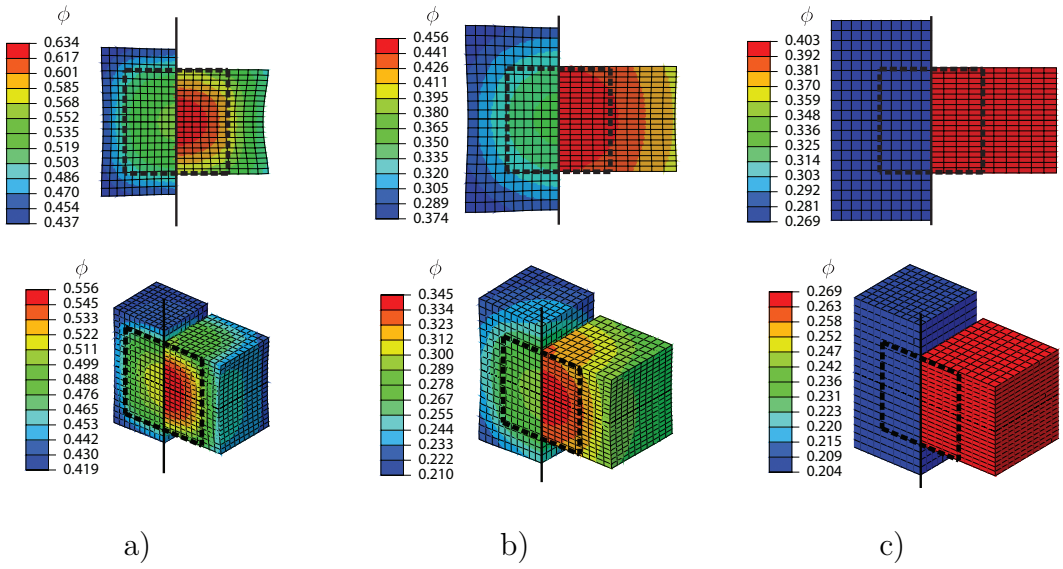

Figure 3.5 Simulation results showing ϕ at a) 900 s, b) 1800 s, and c) 6 hours, in plane strain (top) and 3D (bottom). In all cases, to help with comparison, the left portion is the isotropic simulation, while the right portion is anisotropic diffusion with fiber direction $\mathbf{a}_{\mathrm{R}} = \mathbf{e}_2$ and $f_{\mathrm{R}} = 10^{-1}$. Further, the thick dotted line indicates the initial dry body.

3.8 Diffusion Activated Soft Gripper: Qualitative Comparison Between Experiment and Simulation

As a final exercise of the model, we qualitatively compare our simulation results with experiments of a soft robotic gripper. Since the materials used in the experiment have not yet been characterized, our comparison is only qualitative, and we continue using the material parameters provided in Table 3.1.

The construction of the diffusion activated soft gripper consists of two arms of fiber-reinforced polymer gel connected to a rigid glass plate. The two arms are composed of polyethylene glycol diacrylate (PEGDA 700) and off-the-shelf medical gauze to used for the embedded fibers. To manufacture the soft gripper, a photo-curable precursor solution is prepared by mixing PEGDA 700, as a monomer, and 43 mM of phenylbis(2,4,6-trimethylbenzoyl) phosphine oxide as a photo-initiator. A piece of medical gauze, with approximately a 0.5 mm thickness is placed on a transparent glass mold. The precursor solution is then poured into the mold, up to

1.5 mm from the bottom, and polymerized using ultraviolet (UV) illumination, with an exposure energy of 250 mJ/cm^2. As a result, a 1.5 mm thick composite polymer film is formed, with a 0.5 mm thick fiber network embedded on the bottom as can be seen in Figure 3.6a. The composite polymer film is cut into the 57 mm long and 3.5 mm wide strips as in Figure 3.6b. Two fiber-embedded composite polymer strips, serving as gripper arms, are bonded to a glass plate using super glue. The arms are oriented with the fiber-reinforced side facing downward, with the angle between the arms 70° as shown in Figure 3.7.

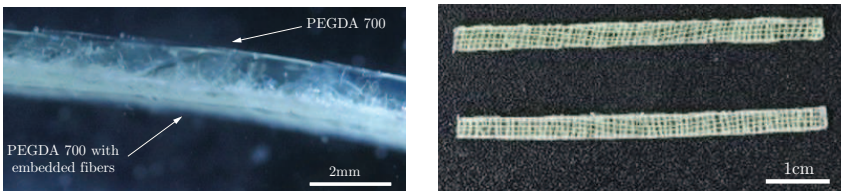

a) b)

Figure 3.6 Manufacture of the composite gripper arm. a) Shows medical gauze embedded in the lower portion of the body, and b) shows the two strips used to construct the soft gripper, prior to bonding in the initial dry state.

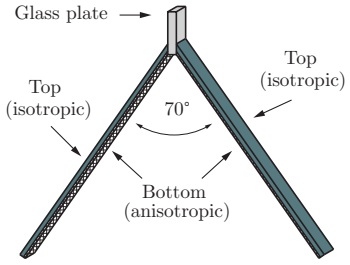

Figure 3.7 Schematic of the soft gripper assembly. The gripper arms are bonded to a glass plate with the fiber-reinforced side facing downward.

In the experiment, shown in Figure 3.8, the full gripper is submerged into solvent, in this case water, and the subsequent diffusion and anisotropic swelling due to the embedded fibers causes the gripper arms to bend and close onto a block. This mode of deformation is utilized for grabbing and subsequently moving the block.

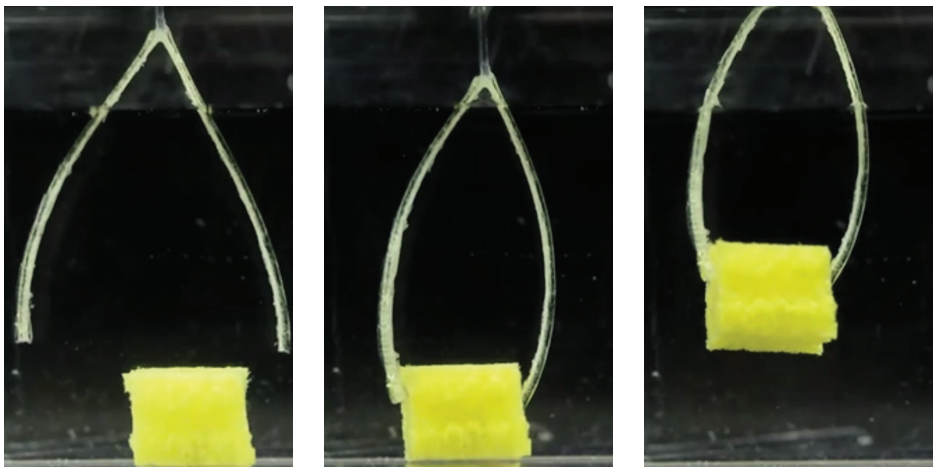

a) b) c)

Figure 3.8 Experimental results showing the operation of diffusion activated soft gripper. a) Initially after immersion into water, b) the embedded fibers cause anisotropic swelling to make the gripper arms close in and grab the block, and c) lifting the block.

For the finite element simulation, due to the symmetry of the gripper, we mesh only a quarter of the geometry, i.e., a half of one arm. The structured finite element mesh of the gripper consists of 6,958 three-dimensional 8-node brick user-elements. Also, since the gripper arms are constructed with embedded fibers only close to the bottom of the arms, we model two distinct layers through the thickness — the bottom with fibers embedded; and an isotropic top layer without fibers. Specifically, the top layer is taken to be 1 mm thick as shown in Figure 3.9; and since there are no embedded fibers, $f_{\text{R}} = 0$, with an isotropic solvent diffusivity $\mathbf{D} = (1.5 \times 10^{-8}\mathbf{1})\,\text{m}^2/\text{s}$. The bottom layer is taken to be 0.5 mm thick, and contains two families of embedded fibers oriented perpendicular to each other with directions, $\mathbf{a}_{\text{R}}^{(1)} = \mathbf{e}_{1'}$ and $\mathbf{a}_{\text{R}}^{(2)} = \mathbf{e}_{3'}$, written in the local coordinate system as shown in Figure 3.9. Additionally, we choose the fiber volume fraction to be the same for both orientations, and relatively small based on Figure 3.6c, specifically $f_{\text{R}}^{(1)} = f_{\text{R}}^{(2)} = 10^{-2}$. Since the bottom layer contains

fibers, we assume the diffusivity to be slightly anisotropic, and we take

$$\mathbf{D} = \begin{bmatrix} 1.0 & 0.0 & 0.0 \\ 0.0 & 1.5 & 0.0 \\ 0.0 & 0.0 & 1.0 \end{bmatrix} \times 10^{-8} \mathrm{m}^2/\mathrm{s} \tag{3.60}$$

in the local $1' - 2' - 3'$ coordinate system as shown in Figure 3.9.[2]

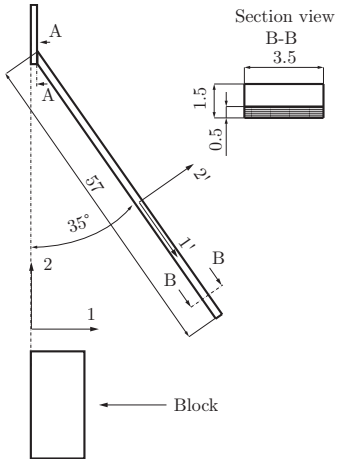

Figure 3.9 Schematic of the soft gripper assembly that is used in the numerical simulation, indicating the local coordinate system used for material properties, as well as the layers with and without fibers.

To realistically simulate the experiment, we include a non-swellable block with edge length 2 mm that will be picked up by the soft gripper. We assume the block is much stiffer than the soft gripper and model the block as linear elastic with modulus 5 GPa. The interaction between the soft gripper and the block is modeled with a rough contact interaction, meaning no slip. For visualization purposes, a rigid body is included in the simulation to model the glass plate from the experiment, and the soft gripper is bonded to this glass plate in the simulation such that it may swell along $\mathbf{e}_2$, but is fully constrained in $\mathbf{e}_1$.

[2]We note that both the fiber directions, and diffusivity, given here in local coordinate system $1'-2'-3'$, are later rotated to the global coordinate system $1-2-3$ inside the finite element simulation.

Considering Figure 3.9, the mechanical boundary conditions prescribed for this simulation are:

- Symmetry boundary conditions are prescribed on the 1-2 and 2-3 planes.
- The displacement on face A-A is mechanically constrained along the 1-direction. In addition, the top node on face A-A is pinned.
- The glass plate is fully constrained, while the block is traction free on all faces.

Next, to account for the immersion in solvent, the chemical potential is prescribed on the external faces of the gripper, except for the face bonded to the glass plate. As before, the chemical potential is prescribed in the form $\breve{\mu}(t) = \mu^0 + \mu_0 \exp(-t/t_d)$ to smoothly apply the chemical potential boundary condition.

Figure 3.10 shows contours of ϕ in the simulation of the soft gripper working at various snapshots in time. The initially dry soft gripper, shown in Figure 3.10a, is immersed in solvent and through diffusion begins to swell and deform. The bottom layer of the gripper, which contains the embedded fibers and has an anisotropic diffusivity, swells less than the top layer. This constrained swelling of the bottom layer, forces the arms to bend, and eventually close in and grab the block. Finally, the block is picked up and may be moved elsewhere.

Comparing our numerical simulation with the experimentally observed operation of a soft gripper, we have qualitative agreement between the two. In both cases, the presence of the embedded fibers on the bottom side of the soft gripper leads to constrained swelling, which in turn causes the gripper to close and grab the block. Therefore, the constitutive model and it's numerical implementation may provide a qualitative tool for the design of soft robotic devices.

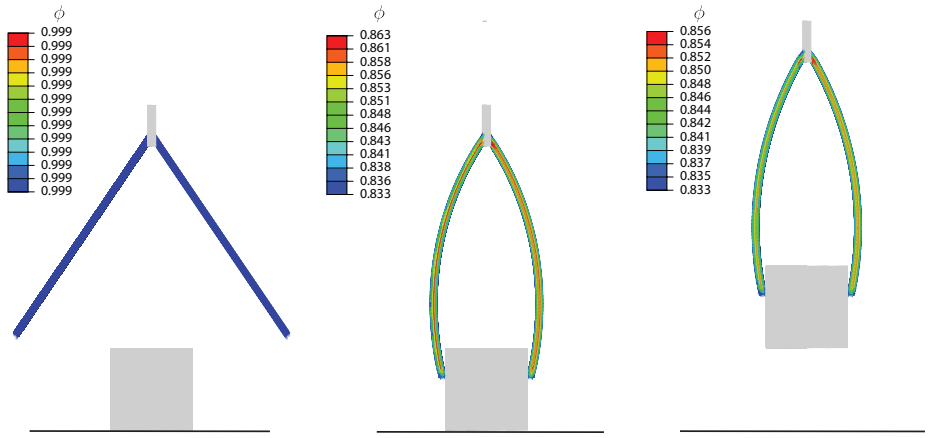

Figure 3.10 Simulation results showing ϕ during operation of diffusion activated soft gripper. a) The initial state immediately after immersion in water, b) the embedded fibers cause anisotropic swelling to make the gripper arms close in and grab the block, and c) lifting the block.

3.9 Concluding Remarks

We have developed a continuum-level model to capture the major features of fiber-reinforced polymeric gel behavior. The anisotropic aspects of the model are i) the influence of non-linear elastic embedded fibers that do not swell inside the polymer matrix, and ii) anisotropic diffusion of solvent within the polymer matrix. The mechanical response of the polymer matrix is described using a non-Gaussian statistical-mechanical model, along with Flory-Huggins model for mixing free energy.

The constitutive model has been numerically implemented in a commercially available software package [1] by writing a user element subroutine (UEL). That numerical implementation was utilized for solving boundary-value problems which showcase the capabilities of the model to simulate the behavior of fiber-reinforced polymeric gels.

Lastly, we have constructed a diffusion activated soft gripper and experimentally observed its operation. Using the numerical implementation of the constitutive model, we were able to simulate the operation of our soft gripper. Qualitative comparison of

experiment and simulation shows good agreement between the two, thus displaying the capabilities of our model to account for the major features of fiber-reinforced polymeric gel behavior.

CHAPTER 4

PHOTO-SENSITIVE POLYMERIC GELS

4.1 Introduction

The objective of this chapter is to develop a continuum-level constitutive model to account for the photochemically driven changes in the swelling of polymeric gels. In addition, we numerically implement the continuum model, for use in finite element software allowing for the solution of general boundary value problems. This approach enables robust and reliable finite element analysis of various devices involving photo-sensitive polymeric gels.

To model the mechanical behavior of photo-sensitive polymeric gels, we consider a free energy form that use the classical statistical mechanics based inverse Langevin model for rubber-like hyperelastic materials (cf., e.g., [5, 3]). The chemical mixing of polymeric network with the solvent is included employing the well-known Flory-Huggins model ([42, 64]).

The photo-chemo-mechanical continuum framework involves three balance laws, (i) the balance of forces and moments, (ii) the balance of active species, and (iii) radiative transfer. For solving this coupled set of equations, we employ the finite element method and numerically implement the framework in the finite element software Abaqus/Standard ([1]) as a user element (UEL) subroutine. This finite element implementation provides a robust simulation capability for the multiphysics response of photo-sensitive polymeric gels.

The remainder of this chapter is organized as follows. Section 4.2 provides the molecular mechanisms and motivate the constitutive model by providing an overview of relevant data from the literature. Section 4.3 provides a description of the continuum framework. Sections 4.4 and 4.5 provides the basic constitutive forms,

thermodynamic restrictions, and the specialized constitutive relations. In Section 4.7 we present the approach for the numerical implementation of the continuum framework and the constitutive model for use in the finite element analysis. Section 4.8 shows the results of representative numerical simulations.

4.2 Experimental Observations and Mechanisms of Photo-Activation

4.2.1 Macroscopic Experimental Results

As previously mentioned, a change in the degree of swelling has been the most widely observed aspect of photo-activation of polymeric gels. Both the photo-induced *trans-cis* isomerization of azobenzene and the photoiosomerization of spirobenzopyran affect the swelling of gels (cf., e.g., [118, 123]). A subset of experimental data reproduced from [24] is presented in Figure 4.1b, and shows a noticeable change in the amount of swelling due to irradiation. To achieve this behavior, [24] used a p(PNIPAAm) hydrogel functionalized with spirobenzopyran chromophores, thus forming a hybrid material – p(SPNIPAAm) hydrogel. As seen in Figure 4.1b, in the absence of light, different variations of p(SPNIPAAm) undergo swelling until equilibrium, which is observed as the increase in the uniaxial swelling stretch. When irradiated, spirobenzopyran chromophores form a hydrophobic closed ring, causing deswelling of p(SPNIPAAm) and the decrease in the uniaxial swelling stretch. Also, after removing the light source, the p(SPNIPAAm) swells again until equilibrium is reached, thus showcasing the reversibility of this photoisomerization reaction.

In addition, the degree of swelling is well known to affect the mechanical behavior of polymeric gels (cf., e.g., [67, 100]). These authors, among other things, clearly point out how the degree of swelling affects the apparent stiffness of a swollen polymeric gel at equilibrium. However, there is still a dearth of experimental data on the large deformation changes to the mechanical behavior of photo-active gels. Accordingly, to keep our attention focused on the objective, and only based on known

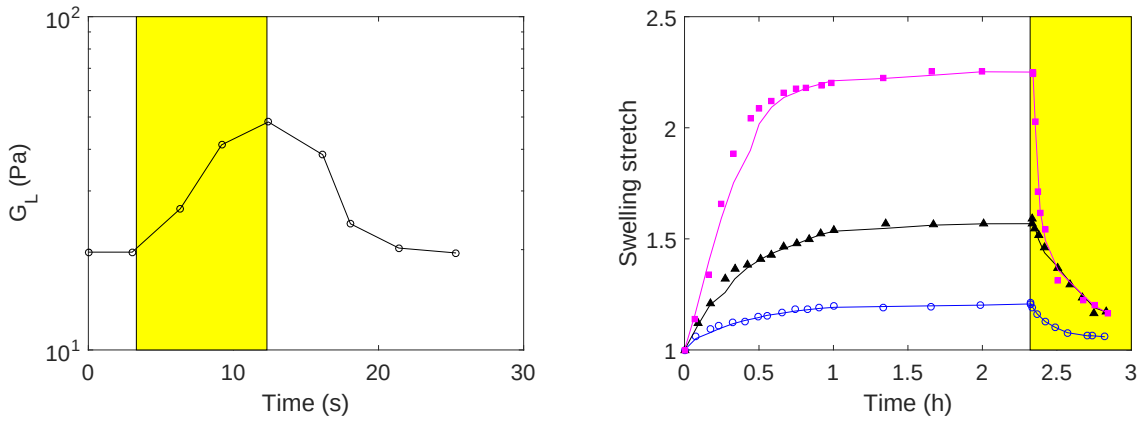

Figure 4.1 a) Experimentally observed change in loss modulus (G_L) due to irradiation (data reproduced from [92]). b) Experimental data from [24] showing the change in the amount of swelling in the absence of light and while irradiated. The measurements were performed on p(SPNPIMAAm) gel swollen with 3 different solvents. In both plots the yellow region indicates the period of active irradiation.

experimental results, we only seek to model the photo-chemo-mechanically coupled behavior related to changes in degree of swelling due to irradiation.

4.2.2 Mechanisms of Photo-Activation

One of the most common approaches for achieving the photo-activation in polymeric gels is through tethering azobenzene groups to the polymeric backbone (cf., e.g., [118, 115, 132, 119]). Upon irradiation with a blue light (wavelength 400-450 nm), the azobenzene group undergoes *cis-trans* photoisomerization that induces a change in shape, size, and polarity, as shown in Figure 4.2a. Further, the change in the chemical structure generates a decrease in available volume in the polymeric network, leading to loss of solvent and deswelling ([84]). On the other hand, when irradiated with a UV light, the azobenzene reverts to *cis* configuration, and the gel swells again.

Another approach for for achieving the photo-activation is to anchor spirobenzopyran groups to the polymeric backbone (cf., e.g., [124, 123]. In the absence of light, the spirobenzopyran chromophores assume a hydrophilic open ring configuration. Irradiation of these chromophores by a blue light, yields a hydrophobic closed ring,

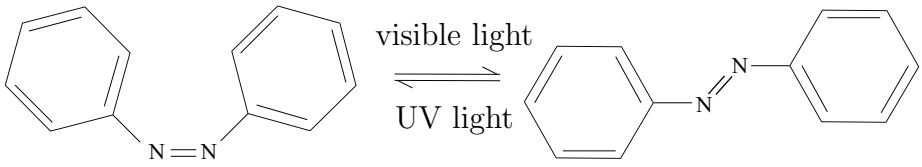

a)

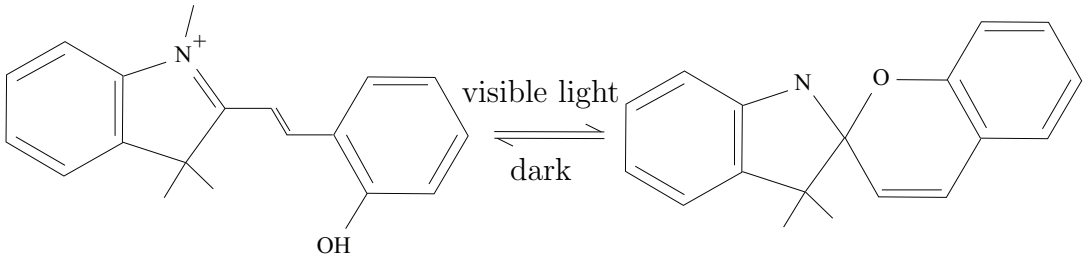

b)

Figure 4.2 a) Azobenzene undergoing the *cis-trans* photoisomerization upon activation with a blue light, and also *trans-cis* photoisomerization under a UV light. b) Spirobenzopyran group going from hydrophilic open ring configuration to a hydrophobic closed ring when irradiated with a blue light. In the absence of light, the spirobenzopyran reverts to an open ring configuration.

as in Figure 4.2b, thus causing the polymeric gel to undergo deswelling [78, 41]). In addition, after removing the light, the spirobenzopyran returns to an open ring configuration and swells again.

4.3 Continuum Framework

Following the previous work by our group (cf., e.g., [16, 17, 15, 51, 9]), in this section we summarize the kinematic relations and the balance laws for the photo-chemo-mechanically coupled behavior of polymeric gels.

4.3.1 Kinematics

We assume the initially dry body $\mathcal{B}_{\mathrm{R}}$ in its referential or undeformed configuration occupies the fixed region of space, with an arbitrary material point $\mathbf{x}_{\mathrm{R}}$. This body then undergoes a motion leading to the current or deformed configuration $\mathcal{B}_t$, which can be expressed as $\mathbf{x} = \chi(\mathbf{x}_{\mathrm{R}}, \mathbf{t})$. Consequently, the deformation gradient takes the

form

$$\mathbf{F} = \nabla \boldsymbol{\chi}, \text{ such that } J = \det \mathbf{F} > 0, \tag{4.1}$$

where J represents the volumetric deformation. In addition, the right and left Cauchy-Green deformation tensors are

$$\mathbf{C} = \mathbf{F}^{\top}\mathbf{F} \text{ and } \mathbf{B} = \mathbf{F}\mathbf{F}^{\top}, \tag{4.2}$$

respectively. Following a widely used approach in modeling the mechanics of gels (cf., e.g., [34, 16]), we employ the multiplicative decomposition of deformation gradient into mechanical and swelling part

$$\mathbf{F} = \mathbf{F}^m\mathbf{F}^s, \text{ with } \mathbf{F}^s = \lambda^s\mathbf{1}. \tag{4.3}$$

Here, $\mathbf{F}^m$ is the mechanical part of the deformation gradient, $\mathbf{F}^s$ is the swelling part of the deformation gradient, and λ^s the spherical swelling stretch.

Next, using (4.2) and (4.3), the right and left Cauchy-Green tensor can be rewritten in the forms

$$\mathbf{C} = (\mathbf{F}^m\mathbf{F}^s)^{\top}(\mathbf{F}^m\mathbf{F}^s) = (\lambda^s)^2\,\mathbf{F}^{m\top}\mathbf{F}^m = (\lambda^s)^2\,\mathbf{C}^m\,, \tag{4.4}$$

$$\mathbf{B} = (\mathbf{F}^m\mathbf{F}^s)(\mathbf{F}^m\mathbf{F}^s)^{\top} = (\lambda^s)^2\,\mathbf{F}^m\mathbf{F}^{m\top} = (\lambda^s)^2\,\mathbf{B}^m\,, \tag{4.5}$$

where $\mathbf{C}^m$ and $\mathbf{B}^m$ represent the mechanical part of the right and left Cauchy-Green tensor, respectively.

With respect to the decomposition of deformation gradient in (4.3), the volumetric deformation is decomposed in the form

$$J = \det \mathbf{F} = \det(\mathbf{F}^m\mathbf{F}^s) = J^m J^s, \tag{4.6}$$

where J^m and J^s are the volumetric deformations due to mechanical deformation and swelling, respectively. Before moving along, we note that based on (4.3), we have

$$J^s = (\lambda^s)^3\,, \quad \text{and therefore} \quad \lambda^s = (J^s)^{1/3}\,. \tag{4.7}$$

Additionally, as is standard, one typically finds the decomposition

$$\mathbf{F} = \mathbf{F}_{\text{vol}}\mathbf{F}_{\text{dis}}, \quad \text{with} \quad \mathbf{F}_{\text{vol}} = J^{1/3}\mathbf{1}\,, \quad \text{and} \quad \mathbf{F}_{\text{dis}} = J^{-1/3}\mathbf{F} \tag{4.8}$$

of the deformation gradient into volumetric and distortional components. Further consideration of the distortional term, and using (4.3) and (4.7), we define the mechanical part of the distortional deformation gradient

$$\mathbf{F}_{\text{dis}} = \left(J^{s-1/3}J^{m-1/3}\right)\left(\lambda^s\mathbf{F}^m\right) = J^{m-1/3}\mathbf{F}^m \overset{\text{def}}{=} \mathbf{F}^m_{\text{dis}}\,. \tag{4.9}$$

Further, using (4.9) the distortional part of the right Cauchy-Green tensor is given by

$$\mathbf{C}_{\text{dis}} = \mathbf{C}^m_{\text{dis}} = \mathbf{F}^{\top}_{\text{dis}}\mathbf{F}_{\text{dis}}\,. \tag{4.10}$$

Next, using (4.1) and (4.3), the velocity gradient can be written as

$$\mathbf{L} = \dot{\mathbf{F}}\mathbf{F}^{-1} = \mathbf{L}^m + \mathbf{F}^m\mathbf{L}^s\left(\mathbf{F}^m\right)^{-1}\,, \tag{4.11}$$

where

$$\mathbf{L}^m = \dot{\mathbf{F}}^m\left(\mathbf{F}^m\right)^{-1} \quad \text{and} \quad \mathbf{L}^s = \dot{\mathbf{F}}^s\left(\mathbf{F}^s\right)^{-1}\,, \tag{4.12}$$

represent the mechanical and swelling part of the velocity gradient, respectively.

We also define the mechanical and swelling stretching and spin tensors

$$\left.\begin{aligned} \mathbf{D}^m &= \operatorname{sym}\mathbf{L}^m \qquad \mathbf{W}^m = \operatorname{skw}\mathbf{L}^m\,, \\ \mathbf{D}^s &= \operatorname{sym}\mathbf{L}^s \qquad \mathbf{W}^s = \operatorname{skw}\mathbf{L}^s \end{aligned}\right\} \tag{4.13}$$

such that

$$\mathbf{L}^m = \mathbf{D}^m + \mathbf{W}^m \quad \text{and} \quad \mathbf{L}^s = \mathbf{D}^s + \mathbf{W}^s \,. \tag{4.14}$$

Recalling (4.3), (4.6) and (4.13), the swelling velocity gradient in (4.14) can be rewritten as

$$\mathbf{L}^s = \mathbf{D}^s = \left(\dot{\lambda}^s \lambda^{s-1}\right) \mathbf{1} = \frac{1}{3}\left(\dot{J}^s J^{s-1}\right) \mathbf{1} \tag{4.15}$$

4.3.2 Extent of Reaction

Following the recent literature ([86, 87, 117]), we take the extent of the chemical reaction lying in the range

$$0 \leq \xi^{(\delta)}(\mathbf{x}, t) \leq 1 \,, \tag{4.16}$$

for each reaction δ.

To account for the change in the concentration of each chemical species β, we introduce the rate of production/consumption for each species

$$r^{(\beta)} = \sum_{\delta} \nu_{\beta\delta} \dot{\xi}^{(\delta)} \,. \tag{4.17}$$

Here, $\nu_{\beta\delta}$ represent the stoichiometric coefficients in moles per unit volume, determining the production/consupmtion of each chemical species β due to the reaction δ.

4.3.3 Swelling Constraint and the Solvent Content

The volumetric deformation caused by swelling is assumed to be only due to the solvent uptake, and because the solvent causes such large volume changes, we denote it specifically by

$$c_{\mathrm{R}} \stackrel{\mathrm{def}}{=} c_{\mathrm{R}}^{(1)} \,, \tag{4.18}$$

and therefore

$$J^s = 1 + \Omega c_{\mathrm{R}}, \quad \text{and therefore} \quad \lambda^s = (1 + \Omega c_{\mathrm{R}})^{1/3}\,, \tag{4.19}$$

where Ω is the molar volume of solvent, and c_{R} is the solvent content expressed as moles per unit reference volume of the dry polymer. Implicit in this statement is that all other chemical species do not cause any volume change. In the literature, one often finds the *polymer volume fraction*, ϕ, which is defined as

$$\phi \overset{\text{def}}{=} \frac{1}{1 + \Omega c_{\mathrm{R}}} = (\lambda^s)^{-3} = (J^s)^{-1}\,, \tag{4.20}$$

and takes the range $0 < \phi \leq 1$. Here $\phi = 1$ refers to a dry polymer and $\phi < 1$ indicates the presence of solvent.

4.3.4 Balance Laws

The photo-chemo-mechanically coupled response of light-activated polymeric gels is affected by the (i) mechanical state (e.g., stress, deformation, etc.), (ii) the solvent content, and (iii) the propagation of light through the body radiative transfer does not directly take the extent of reaction into account. Therefore, we assume the response of a light-activated polymeric gel is determined by the balance of forces and moments, the balance of solvent content, and radiative transfer.

Balance of Forces and Moments Neglecting inertial effects, the balance of forces and moments in the referential body $\mathcal{B}_{\mathrm{R}}$ takes the well known relations

$$\operatorname{div} \mathbf{T}_{\mathrm{R}} + \mathbf{b}_{\mathrm{R}} = \mathbf{0} \quad \text{and} \quad \mathbf{T}_{\mathrm{R}}\mathbf{F}^{\top} = \mathbf{F}\mathbf{T}_{\mathrm{R}}^{\top}\,. \tag{4.21}$$

Here $\mathbf{T}_{\mathrm{R}}$ is the first Piola stress and $\mathbf{b}_{\mathrm{R}}$ is the external body force per unit reference volume.

Further, the first Piola stress in the undeformed body is related to the Cauchy stress in the deformed body by

$$\mathbf{T}_{\mathrm{R}} = J\mathbf{T}\mathbf{F}^{-\top}. \tag{4.22}$$

Additionally, in the current configuration the balance of forces and moments in the deformed body $\mathcal{B}_t$ takes the well known relations

$$\operatorname{div}\mathbf{T} + \mathbf{b} = \mathbf{0} \quad \text{and} \quad \mathbf{T} = \mathbf{T}^{\top}, \tag{4.23}$$

where $\mathbf{b}$ is the external body force acting on the unit current volume.

Lastly, the traction acting on the surface with the outward unit normal $\mathbf{n}_{\mathrm{R}}$ in the referential configuration, and $\mathbf{n}$ in the current configuration is given by

$$\mathbf{t}_{\mathrm{R}} = \mathbf{T}_{\mathrm{R}}\mathbf{n} \quad \text{and} \quad \mathbf{t} = \mathbf{T}\mathbf{n}. \tag{4.24}$$

Balance of Species In general, a photo-chemically reacting polymeric gel may contain several chemical species, such as the solvent or photosensitive groups, which possibly diffuse and/or partake in chemical reactions causing causing swelling/deswelling and other novel behaviors. To account for the overall balance of species in photo-sensitive gels, we first introduce the concentration of species $c^{(\beta)}$ as the amount of moles per unit deformed volume, where the superscript"β" represents each of the species.

The balance of chemical species keeps track of the concentration of species, and we denote an arbitrary subregion of the body $\mathcal{P}_t$ in the deformed body $\mathcal{B}_t$. At this stage of development, we allow for all species to be mobile, and all species to partake in reactions, specific forms will be provided later in Section 4.5. Considering a region of the body $\mathcal{P}_t$, the balance of chemical species for each active mobile species is given by

$$\overline{\int_{\mathcal{P}_t} c^{(\beta)} dv}^{\cdot} = -\int_{\partial\mathcal{P}_t} \mathbf{j}^{(\beta)} \cdot \mathbf{n} da + \int_{\mathcal{P}_t} r^{(\beta)} dv \quad \forall\beta \tag{4.25}$$

where $\mathbf{j}^{(\beta)}$ is the flux, and $r^{(\beta)}$ the production/consumption rate of species β and is constrained by the stoichiometry of the chemical reaction as mentioned in (4.17). Use of the divergence theorem, along with the relation $c_{\mathrm{R}}^{(\beta)} = Jc^{(\beta)}$ for the concentration of species in moles per unit reference volume, leads to the local balance of chemical species

$$\frac{\dot{c}_{\mathrm{R}}^{(\beta)}}{J} = -\mathrm{div}\mathbf{j}^{(\beta)} + r^{(\beta)} \quad \forall\beta\,. \tag{4.26}$$

Lastly, using (4.17) we may rewrite (4.26) into the form

$$\frac{\dot{c}_{\mathrm{R}}^{(\beta)}}{J} = -\mathrm{div}\mathbf{j}^{(\beta)} + \sum_{\delta} \nu_{\beta\delta}\dot{\xi}^{(\beta)} \quad \forall\beta \tag{4.27}$$

where we have made use of ξ as opposed to r.

We also define the species flux acting on the surface with an outward normal $\mathbf{n}$ in the current configuration as

$$j^{(\beta)} = -\mathbf{j}^{(\beta)} \cdot \mathbf{n} \quad \forall\beta\,. \tag{4.28}$$

Radiative Transfer When a surface of a polymeric gel is exposed to light irradiation, a portion of the light rays will be reflected from the surface, while the other portion is refracted and starts propagating through the body. While the light is propagating inside the body, the energy is being carried in the form of photons. Following the recent literature ([89, 27]) we follow a radiometric description where electromagnetic waves are considered as a flow of radiative energy or photons.

In general, light can propagate in any direction, and at any frequency (or equivalently wavelength) inside the body. As is typically done, the spectral radiative intensity $I_{\nu\omega}(\mathbf{x}, t)$ is defined as the amount of energy at solid angle ω and frequency ν. Integration over all solid angles and frequencies yields the total radiative energy flux vector having units of power per unit deformed area, $\mathbf{h}(\mathbf{x}, t)$,

$$\mathbf{h} = \int_{\nu}\int_{4\pi} I_{\nu\omega}\mathbf{s}d\omega\, d\nu\,, \tag{4.29}$$

where $\mathbf{s}$ is the direction of propagation (determined by the solid angle ω). Based on the experiments provided in Section 4.2, typically the light is unpolarized with only a single frequency of light is active at a time, and along a single direction $\mathbf{d}$. Accordingly, (4.29) may be simplified to

$$\mathbf{h} = \int_{\nu} \int_{4\pi} I\delta(\nu - \nu_0)\delta(\omega - \omega_0)\mathbf{d}d\omega\, d\nu = I\mathbf{d} \tag{4.30}$$

where $I(\mathbf{x}, t)$ is the radiative intensity and δ the Dirac delta function. After applying the product rule for divergence, we may rewrite (4.30) in the form

$$\operatorname{div}\mathbf{h} = \operatorname{div}(I\mathbf{d}) = \underbrace{I\operatorname{div}(\mathbf{d})}_{=0} + \mathbf{d}\cdot\operatorname{grad} I\,. \tag{4.31}$$

The balance of energy for a ray of light is described by radiative transfer, in a general multidimensional form, radiative transfer is given by ([13])

$$\frac{1}{c}\frac{\partial I}{\partial t} + \mathbf{d}\cdot\operatorname{grad} I = -\underbrace{k_s I}_{\text{out-scattering}} + \underbrace{\frac{1}{4\pi c}k_s \int_{\mathcal{B}_t} I dv}_{\text{in-scattering}} - \underbrace{k_a I}_{\text{absorption}} + \underbrace{\iota}_{\text{emission}}\,. \tag{4.32}$$

And one can notice the light intensity along the direction $\mathbf{d}$ is being attenuated by out-scattering and absorption, with the corresponding coefficients k_s and k_a. Also the emission ι and the in-scattering increase the light intensity.

Following the previous work by our group, found in [51], as well as the approach found in [88] and [27], we propose a simplified form for the radiative transfer. The typical time scale for transient behaviors of the light are set by the speed of light in that medium, compared to mechanical deformations, and photo-chemical reactions, we assume steady state conditions for light propagation. Next, we assume the scattering and the emission to be negligible, which is true for many polymers in use ([36, 71, 75]). Therefore, with these simplifying assumptions, (4.32) can be rewritten as

$$\mathbf{d}\cdot\operatorname{grad} I + \Lambda I = 0\,, \tag{4.33}$$

where Λ represents the extinction field, which takes into account the attenuation of light in a lumped manner.

Free Energy Imbalance The first two laws of thermodynamics under isothermal conditions take the form of the free energy imbalance, which requires the temporal increase in the free energy to be less or equal of the power expanded on a part $\mathcal{P}_t$ of the body, along with any brought into $\mathcal{P}_t$ though solvent diffusion or light irradiation, as well as the photo-chemical reactions. Therefore, the free energy imbalance in the current configuration takes the form

$$\dot{\overline{\int_{\mathcal{P}_t} \rho\psi dv}} \leq \int_{\partial\mathcal{P}_t} \mathbf{T}\mathbf{n}\cdot\mathbf{v}da + \int_{\mathcal{P}_t} \mathbf{b}\cdot\mathbf{v}dv - \sum_\beta \int_{\partial\mathcal{P}_t} \mu^{(\beta)}\mathbf{j}^{(\beta)}\cdot\mathbf{n}da + \sum_\beta \int_{\mathcal{P}_t} \mu^{(\beta)} r^{(\beta)} dv - \int_{\partial\mathcal{P}_t} \mathbf{h}\cdot\mathbf{n}da\,, \quad (4.34)$$

where ψ is the free energy density per unit deformed mass, ρ the mass density, $\mu^{(\beta)}$ is the chemical potential of each chemical species, and $\mathbf{h}$ is the radiative flux.

Next, noting that the part $\mathcal{P}_t$ is arbitrary, in the absence of body forces and inertial affects, and after applying the divergence theorem on (4.34), we arrive at the local form

$$\rho\dot{\psi} \leq \mathbf{T}:\mathbf{L} - \sum_\beta \mathbf{j}^{(\beta)}\cdot\operatorname{grad}\mu^{(\beta)} - \sum_\beta \mu^{(\beta)}\operatorname{div}\mathbf{j}^{(\beta)} + \sum_\beta \mu^{(\beta)} r^{(\beta)} - \operatorname{div}\mathbf{h}\,. \quad (4.35)$$

Next, using (4.27) in (4.35), we obtain

$$\rho\dot{\psi} \leq \mathbf{T}:\mathbf{L} - \sum_\beta \mathbf{j}^{(\beta)}\cdot\operatorname{grad}\mu^{(\beta)} + \sum_\beta J^{-1}\mu^{(\beta)}\dot{c}_{\mathrm{R}}^{(\beta)} - \operatorname{div}\mathbf{h}\,. \quad (4.36)$$

Since the free-energy density per unit reference volume is related to it's spatial counterpart by

$$\psi_{\mathrm{R}} = \rho J\psi \quad (4.37)$$

we may write the dissipation per unit reference volume,

$$\dot{\psi}_{\mathrm{R}} - J\mathbf{T}:\mathbf{L} + J\mathrm{div}\,\mathbf{h} + \sum_{\beta} J\mathbf{j}^{(\beta)} \cdot \mathrm{grad}\,\mu^{(\beta)} - \sum_{\beta} \mu^{(\beta)} \dot{c}_{\mathrm{R}}^{(\beta)} \leq 0\,. \tag{4.38}$$

Following standard arguments, the stress power per unit reference volume, $J\mathbf{T}:\mathbf{L}$, admits the decomposition

$$\begin{aligned}
J\mathbf{T}:\mathbf{L} &= J\mathbf{T}:\left(\mathbf{L}^m + \mathbf{F}^m\mathbf{L}^s\mathbf{F}^{m-1}\right)\\
&= J\mathbf{T}:\left(\dot{\mathbf{F}}^m\mathbf{F}^{m-1}\right) + J\mathbf{T}:\left(\mathbf{F}^m\mathbf{L}^s\mathbf{F}^{m-1}\right)\\
&= \left(J\mathbf{T}\mathbf{F}^{m-\top}\right):\dot{\mathbf{F}}^m + \left(J\mathbf{F}^{m\top}\mathbf{T}\mathbf{F}^{m-\top}\right):\mathbf{L}^s\\
&= \left(J\mathbf{F}^{m-1}\mathbf{T}\mathbf{F}^{m-\top}\right):\left(\mathbf{F}^{m\top}\dot{\mathbf{F}}^m\right) + \left(J\mathbf{F}^{m\top}\mathbf{T}\mathbf{F}^{m-\top}\right):\left(\frac{1}{3}J^{s-1}\dot{J}^s\mathbf{1}\right)\\
&= \mathbf{T}^m:\frac{1}{2}\dot{\mathbf{C}}^m + \frac{1}{3}J^{s-1}\mathrm{tr}\,\mathbf{M}^m\dot{J}^s\,.
\end{aligned} \tag{4.39}$$

Where we have defined two new stress measures

$$\mathbf{T}^m \overset{\mathrm{def}}{=} J\mathbf{F}^{m-1}\mathbf{T}\mathbf{F}^{m-\top} \quad \text{and} \quad \mathbf{M}^m \overset{\mathrm{def}}{=} J\mathbf{F}^{m\top}\mathbf{T}\mathbf{F}^{m-\top}\,, \tag{4.40}$$

where $\mathbf{T}^m$ is a mechanical second Piola stress, and $\mathbf{M}^m$ is a mechanical Mandel stress. We also introduce a mean normal pressure in the form

$$\bar{p} \overset{\mathrm{def}}{=} -\frac{1}{3}J^{s-1}\mathrm{tr}\,\mathbf{M}^m = -\frac{1}{3}J^{s-1}\mathrm{tr}\,\left(J\mathbf{F}^{m\top}\mathbf{T}\mathbf{F}^{m-\top}\right) = -\frac{1}{3}J^m\mathrm{tr}\,\mathbf{T} \tag{4.41}$$

such that (4.39) becomes

$$J\mathbf{T}:\mathbf{L} = \mathbf{T}^m:\frac{1}{2}\dot{\mathbf{C}}^m - \bar{p}\dot{J}^s\,. \tag{4.42}$$

Finally, using (4.42), the free energy imbalance (4.38) takes the form

$$\dot{\psi}_{\mathrm{R}} - \frac{1}{2}\mathbf{T}^m:\dot{\mathbf{C}}^m - \bar{p}\dot{J}^s + J\mathrm{div}\,\mathbf{h} + \sum_{\beta} J\mathbf{j}^{(\beta)} \cdot \mathrm{grad}\,\mu^{(\beta)} - \sum_{\beta} \mu^{(\beta)} \dot{c}_{\mathrm{R}}^{(\beta)} \leq 0\,. \tag{4.43}$$

In light of (4.19), we have $\dot{J}^s = \Omega \dot{c_{\mathrm{R}}}^{(s)}$, and therefore (4.38) can be written in the form

$$\dot{\psi}_{\mathrm{R}} - \frac{1}{2}\mathbf{T}^m : \dot{\mathbf{C}}^m - \left(\mu^{(s)} + \Omega\bar{p}\right)\dot{c}_{\mathrm{R}}^{(s)} + J\mathrm{div}\,\mathbf{h} + \sum_{\beta} J\mathbf{j}^{(\beta)} \cdot \mathrm{grad}\,\mu^{(\beta)} - \sum_{\beta\neq 1} \mu^{(\beta)}\dot{c}_{\mathrm{R}}^{(\beta)} \leq 0\,. \tag{4.44}$$

4.4 Basic Constitutive Equations and Thermodynamic Restrictions

Considering frame indifference and the free energy imbalance (4.44), the set basic constitutive equations consists of

$$\left.\begin{aligned} \psi_{\mathrm{R}} &= \bar{\psi}_{\mathrm{R}}\left(\mathbf{C}^m, c_{\mathrm{R}}^{(\beta)}, \xi^{(\delta)}\right) \\ \mathbf{T}^m &= \bar{\mathbf{T}}^m\left(\mathbf{C}^m, c_{\mathrm{R}}^{(\beta)}, \xi^{(\delta)}\right) \\ \mu^{(\beta)} &= \bar{\mu}^{(\beta)}\left(\mathbf{C}^m, c_{\mathrm{R}}^{(\beta)}, \xi^{(\delta)}\right) \end{aligned}\right\} \tag{4.45}$$

along with a Darcy-type relation for the spatial species flux

$$\mathbf{j}^{(\beta)} = -\bar{\mathbf{M}}^{(\beta)}(\mathbf{C}^m, c_{\mathrm{R}}^{(\beta)}, \xi^{(\delta)})\mathrm{grad}\,\mu^{(\beta)} \quad \forall\beta\,. \tag{4.46}$$

where $\mathbf{M}^{(\beta)}$ is the mobility tensor for each species.

Since

$$\dot{\psi}_{\mathrm{R}}(\mathbf{C}^m, c_{\mathrm{R}}^{(\beta)}, \xi^{(\delta)}) = \frac{\partial\psi_{\mathrm{R}}}{\partial\mathbf{C}^m} : \dot{\mathbf{C}}^m + \sum_{\beta}\frac{\partial\psi_{\mathrm{R}}}{\partial c_{\mathrm{R}}^{(\beta)}}\dot{c}_{\mathrm{R}}^{(\beta)} + \sum_{\delta}\frac{\partial\psi_{\mathrm{R}}}{\partial\xi^{(\delta)}}\dot{\xi}^{(\delta)} \tag{4.47}$$

use of (4.47) and (4.46) in (4.44) provides

$$\begin{aligned} &\left(\frac{\partial\bar{\psi}_{\mathrm{R}}}{\partial\mathbf{C}^m} - \frac{1}{2}\mathbf{T}^m\right) : \dot{\mathbf{C}}^m + \sum_{\beta\neq 1}\left(\frac{\partial\bar{\psi}_{\mathrm{R}}}{\partial c_{\mathrm{R}}^{(\beta)}} - \mu^{(\beta)}\right)\dot{c}_{\mathrm{R}}^{(\beta)} + \left(\frac{\partial\bar{\psi}_{\mathrm{R}}}{\partial c_{\mathrm{R}}^{(s)}} - \mu^{(s)} - \Omega\bar{p}\right)\dot{c}_{\mathrm{R}}^{(s)} \\ &\qquad + \sum_{\delta}\frac{\partial\bar{\psi}_{\mathrm{R}}}{\partial\xi^{(\delta)}}\dot{\xi}^{(\delta)} + J\mathrm{div}\,\mathbf{h} - \sum_{\beta} J\left[\mathrm{grad}\,\mu^{(\beta)} \cdot \left(\mathbf{M}^{(\beta)}\mathrm{grad}\,\mu^{(\beta)}\right)\right] \leq 0\,, \end{aligned} \tag{4.48}$$

which must hold for all valid constitutive equations and motions of the body. Further, sufficient conditions for the constitutive equations to satisfy (4.48) provide the state

relations, for the stress

$$\mathbf{T} = J^{-1}\Big[2\mathbf{F}^m \frac{\partial \bar{\psi}_{\mathrm{R}}(\mathbf{C}^m, c_{\mathrm{R}}^{(\beta)}, \xi^{(\delta)})}{\partial \mathbf{C}^m}\mathbf{F}^{m\mathrm{T}}\Big]\,, \tag{4.49}$$

the chemical potential of the solvent

$$\mu^{(s)} = \frac{\partial \bar{\psi}_{\mathrm{R}}(\mathbf{C}^m, c_{\mathrm{R}}^{(\beta)}, \xi^{(\delta)})}{\partial c_{\mathrm{R}}} + \Omega\bar{p}\,, \tag{4.50}$$

and the chemical potential of all other chemical species

$$\mu^{(\beta)} = \frac{\partial \bar{\psi}_{\mathrm{R}}(\mathbf{C}^m, c_{\mathrm{R}}^{(\beta)}, \xi^{(\delta)})}{\partial c_{\mathrm{R}}^{(\beta)}}\,, \quad \forall\beta \neq 1\,. \tag{4.51}$$

Next, we introduce the chemical affinity as the tendency of chemical species to participate in reactions, given as

$$A^{(\delta)} = -\frac{\partial \bar{\psi}_{\mathrm{R}}}{\partial \xi^{(\delta)}}\,. \tag{4.52}$$

Leaving the dissipation inequality

$$\sum_{\delta} A^{(\delta)}\dot{\xi}^{(\delta)} - J\mathrm{div}\,\mathbf{h} + \sum_{\beta} J\left[\mathrm{grad}\,\mu^{(\beta)} \cdot \left(\mathbf{M}^{(\beta)}\mathrm{grad}\,\mu^{(\beta)}\right)\right] \geq 0\,. \tag{4.53}$$

To satisfy (4.53), we assume the response is strictly dissipative,

$$\mathrm{grad}\,\mu^{(\beta)} \cdot \left(\mathbf{M}^{(\beta)}\mathrm{grad}\,\mu^{(\beta)}\right) > 0 \quad \text{when} \quad \mathrm{grad}\,\mu^{(\beta)} \neq \mathbf{0} \quad \forall\beta\,, \tag{4.54}$$

so that the mobility tensor is positive definite for all chemical species. Further, using (4.31) and (4.33), the second term provides

$$\Lambda I > 0 \quad \text{when} \quad \mathrm{grad}\,I \neq \mathbf{0}\,, \tag{4.55}$$

so therefore Λ must be positive, and

$$\sum_{\delta} A^{(\delta)}\dot{\xi}^{(\delta)} > 0 \quad \text{when} \quad \dot{\xi}^{(\delta)} \neq 0\,. \tag{4.56}$$

4.5 Specialized Constitutive Equations

4.5.1 Specific Photo-Chemical Reactions

In this work we consider two representative chemical mechanisms towards achieving the photo-responsiveness of a gel. These reactions are the *trans-cis* isomerization of azobenzene groups and the photo-isomerization of spirobenzopyran shown in Figures 4.2a and 4.2b, respectively.

Isomerization Reaction In this case, there is a single reaction, which is reversible, and the molecular structure undergoes a change in configuration, while the chemical composition remains unaltered. Therefore, we consider the chemical reaction in the form

$$A \rightleftharpoons B \tag{4.57}$$

where A represents the reactant and B is the product after isomerization. It is also worthwhile noting that many isomerization reactions can be thermally activated, however, we are not considering thermal effects in this work.

Accordingly, in this special case we have three chemical species to keep track of, the imbibed solvent and the concentrations of isomers A and B, and there is only a single reaction. While solvent is allowed to diffuse throughout the polymeric network, however it does not partake in chemical reactions. In contrast, both isomers A and B are anchored to the polymeric network and therefore do not diffuse, and therefore $\mathbf{j}^{(A)} = \mathbf{j}^{(B)} = \mathbf{0}$, however does partake in the reaction. Lastly, since there is only a single reaction, and the stoichiometric coefficients in (4.57) are ± 1, meaning a single A turns into a single B and vise versa, we have a single extent of reaction ξ. Therefore

(4.27) in this special case reduces to a set of 3 equations

$$\left.\begin{aligned} \dot{c}_{\mathrm{R}}^{(s)} &= J\mathrm{div}\,\mathbf{j}^{(s)} \\ \dot{c}_{\mathrm{R}}^{(A)} &= -\dot{\xi} \\ \dot{c}_{\mathrm{R}}^{(B)} &= \dot{\xi} \end{aligned}\right\}, \tag{4.58}$$

subject to the constraint

$$c_{\mathrm{R}}^{(A)} + c_{\mathrm{R}}^{(B)} = c_0^{(A)}\,, \tag{4.59}$$

Where we assume that the initial conditions for concentrations of A and B are $c_{\mathrm{R}}^{(A)} = c_0^{(A)}$ and $c_{\mathrm{R}}^{(B)} = 0$ everywhere in $\mathcal{B}_{\mathrm{R}}$.

4.5.2 Free Energy

To model this coupled problem, the free energy consists of multiple contributions that we assume are additively decomposed. The overall free energy per unit reference volume is given by

$$\psi_{\mathrm{R}} = \psi_{\mathrm{R}}^{\mathrm{mechanical}} + \psi_{\mathrm{R}}^{\mathrm{mix}} + \psi_{\mathrm{R}}^{\mathrm{reaction}}\,, \tag{4.60}$$

where $\psi_{\mathrm{R}}^{\mathrm{mechanical}}$ is the mechanical contribution, $\psi_{\mathrm{R}}^{\mathrm{mix}}$ the mixing contribution between the polymer network and solvent, and $\psi_{\mathrm{R}}^{\mathrm{reaction}}$ is the chemical reaction contribution.

Mechanical Contribution to the Free Energy We take the mechanical contribution following a non-Gaussian statistical mechanics based model ([5, 3]), which accounts for the limited extensibility of polymer chains,

$$\begin{aligned} \psi_{\mathrm{R}}^{\mathrm{mechanical}} = G_0\lambda_L^2\Big[\Big(\frac{\bar{\lambda}}{\lambda_L}\Big)\beta + \ln\Big(\frac{\beta}{\sinh\beta}\Big) - \Big(\frac{1}{\lambda_L}\Big)\beta_0 - \ln\Big(\frac{\beta_0}{\sinh\beta_0}\Big)\Big] \\ - G_0\left(\frac{\lambda_L}{3}\ln J\beta_0\right) + J^s\left[\frac{1}{2}K\ln J^m\right]. \end{aligned} \tag{4.61}$$

Here, we introduce the effective stretch

$$\bar{\lambda} \stackrel{\text{def}}{=} \sqrt{\frac{1}{3}\text{tr}\,\mathbf{C}} = \frac{1}{\sqrt{3}}\,(1+\Omega c_{\text{R}})^{1/3}\,\sqrt{\text{tr}\,\mathbf{C}^m}\,, \tag{4.62}$$

which is a scalar representation of the three dimensional state of deformation which includes the combined effects of mechanical and swelling deformation. Further, $\beta = \mathcal{L}^{-1}\Big(\frac{\bar{\lambda}}{\lambda_L}\Big)$, and $\beta_0 = \mathcal{L}^{-1}\Big(\frac{1}{\lambda_L}\Big)$, where $\mathcal{L}^{-1}$ is the inverse of the Langevin function, given by $\mathcal{L}(\bullet) = \coth(\bullet) - (\bullet)^{-1}$. This particular form accounts for locking behavior of the polymeric network at large stretches. This specific form employs two material parameters, the initial shear modulus G_0 and the locking stretch λ_L.

In the current literature there has been no evidence of photoisomerization directly affecting the mechanical response of gels directly. The evidence points to affecting the degree of swelling only. Therefore, we consider the mechanical material parameters constant throughout the photoisomerization reaction.

Mixing Contribution to the Free Energy The mixing contribution to the free energy arises as a result of mixing between the polymeric network, the solvent and the remaining chemical species. In general for the mixing free energy of standard gels the widely used Flory-Huggins model ([43, 64]) is used, which takes into account the difference in size and chemical interaction between the solvent molecules and the polymer chains. It is given by

$$\psi_{\text{R}}^{\text{mix}} = \mu^0 c_{\text{R}} + R\vartheta c_{\text{R}}\left(\ln\Big(\frac{\Omega c_{\text{R}}}{1+\Omega c_{\text{R}}}\Big) + \chi\Big(\frac{1}{1+\Omega c_{\text{R}}}\Big)\right), \tag{4.63}$$

where, μ^0 is the reference chemical potential of the solvent, R is the gas constant and θ is the absolute temperature. Here, χ is the polymer-solvent interaction parameter, which accounts for the disaffinity between the solvent molecules and the polymer network. In other words, χ determines the amount of swelling in a polymeric gel in the presence of a specific solvent.

In this case, there is ample experimental evidence that isomerization affects the degree of swelling. Accordingly, to model the experimentally observed change in the mixing response due to irradiation shown in Section 4.2, and consider the polymer-solvent interaction to be affected by the extent of the photochemical reaction

$$\chi(\xi) = \frac{1}{2}\left(\chi_L + \chi_H\right) - \frac{1}{2}\left(\chi_L - \chi_H\right)\tanh\left(\frac{\xi - \xi_T}{\Delta}\right) \tag{4.64}$$

where χ_L and χ_H represent the polymer-solvent interactions below and above the transition extent of photochemical reaction ξ_T, and Δ is the width in transition. A similar approach was employed to model the temperature-dependent polymer-solvent interaction in [17].

To take into account the amount photo-sensitive groups tethered onto the polymeric backbone, and consequently the impact on photo-activation, we speculate $\chi_H = \chi_H(c_{\mathrm{R}}^{(B)})$. And since we currently do not have experimental evidence at hand, we assume a very simple form

$$\chi_H = \chi_0 + \chi_1 c_{\mathrm{R}}^{(B)} \tag{4.65}$$

such that χ_H is linearly affected by the concentration of photo-sensitive groups. Using this form, a gel with a relatively small amount of photo-senesitive groups will deswell less than the same gel with relatively more photo-sensitive groups.

Reaction Contribution to the Free Energy Following our previous work (cf., e.g., [117]), we introduce a simple form for the reaction contribution to the free energy

$$\psi_{\mathrm{R}}^{\mathrm{reaction}} = \frac{1}{2}H(\nu - \xi)^2 \tag{4.66}$$

where H represents the chemical modulus, and ν the state that minimizes energy.

4.5.3 Stress

Based on the state relation (4.49), and the specialized free energy forms (4.61), (4.63) and (4.66), we obtain the relation for Cauchy stress

$$\mathbf{T} = J^{-1}\left[G_0\left(\zeta\phi^{-2/3}\mathbf{B}^m - \zeta_0\mathbf{1}\right) + J^s K(\ln J^m)\mathbf{1}\right], \tag{4.67}$$

where

$$\zeta \overset{\text{def}}{=} \left(\frac{\lambda_L}{3\bar{\lambda}}\right)\mathcal{L}^{-1}\left(\frac{\bar{\lambda}}{\lambda_L}\right) \text{ and } \zeta_0 \overset{\text{def}}{=} \left(\frac{\lambda_L}{3}\right)\mathcal{L}^{-1}\left(\frac{1}{\lambda_L}\right). \tag{4.68}$$

4.5.4 Chemical Potential

Following (4.50), and the specialized free energy forms (4.61), (4.63) and (4.66), the chemical potential of the solvent takes the form

$$\mu^{(s)} = \mu^0 + R\vartheta\Big(\ln(1-\phi) + \phi + \chi\phi^2\Big) - \Omega K(\ln J^m) + \frac{1}{2}K\Omega(\ln J^m)^2. \tag{4.69}$$

Similarly, with respect to (4.51), the chemical potential of all remaining chemical species is

$$\mu^{(\beta)} = 0 + \frac{\partial\psi_{\mathrm{R}}^{\text{reaction}}}{\partial c_{\mathrm{R}}^{(\beta)}} (\text{maybe, but we'll have to choose a specific form for reaction free energy.}) \tag{4.70}$$

4.5.5 Chemical Affinity

Following the state relation (4.52) and the overall sum of the free energy (4.60), the general form of the chemical affinity can be written as

$$A = -\left(\frac{\partial\psi_{\mathrm{R}}^{\mathrm{TI}}}{\partial\xi} + \frac{\partial\psi_{\mathrm{R}}^{\mathrm{TD}}}{\partial\xi} + \frac{\partial\psi_{\mathrm{R}}^{\text{mixing}}}{\partial\xi} + \frac{\partial\psi_{\mathrm{R}}^{\text{reaction}}}{\partial\xi}\right). \tag{4.71}$$

Considering the mechanical free energy unaltered by the photoisomerization, as well as the specialized forms for the polymer-solvent interaction (4.64) and reaction

free energy (4.66), the chemical affinity is given by

$$\begin{aligned} A &= -\left(0 + 0 + \frac{\partial \psi_{\mathrm{R}}^{\mathrm{mix}}}{\partial \xi} + \frac{\partial \psi_{\mathrm{R}}^{\mathrm{reaction}}}{\partial \xi}\right) \\ &= R\vartheta c_{\mathrm{R}} \Big(\frac{1}{1+\Omega c_{\mathrm{R}}}\Big) \frac{1}{2} \left(\chi_L - \chi_H\right) \operatorname{sech}^2 \left(\frac{\xi - \xi_T}{\Delta}\right) \frac{1}{\Delta} + H(\kappa - \xi)\,. \end{aligned} \tag{4.72}$$

4.5.6 Extinction Field

The polymeric gel is a solid mixture of a polymer and a solvent, each with unique attenuation properties. Since the polymeric network involves the polymeric backbone, along with the tethered *cis* and *trans* isomers, the polymer network extinction field can be written as

$$\Lambda^{\mathrm{p}} = \Lambda^{\mathrm{backbone}} + c^{\mathrm{A}}\Lambda^{\mathrm{A}} + c^{\mathrm{B}}\Lambda^{\mathrm{B}}\,, \tag{4.73}$$

where $\Lambda^{\mathrm{backbone}}$ is the extinction field of the polymeric backbone, and Λ^{A} and Λ^{B} represent the extinction field of each isomer. Weighted based on the polymer volume fraction, we take the overall gel extinction field at a material point in the form

$$\begin{aligned} \Lambda &= (1-\phi)\,\Lambda^{\mathrm{s}} + \phi\Lambda^{\mathrm{p}} \\ &= (1-\phi)\,\Lambda^{\mathrm{s}} + \phi\left(\Lambda^{\mathrm{backbone}} + c^{\mathrm{A}}\Lambda^{\mathrm{A}} + c^{\mathrm{B}}\Lambda^{\mathrm{B}}\right)\,, \end{aligned} \tag{4.74}$$

where Λ^{s} is the solvent extinction field.

4.5.7 Mobility Tensor

The mobility tensor for each chemical species is assumed to be dependent on the concentration (or solvent content) and the temperature, as is typical. Following the literature ([16, 9]), we take the mobility in the form

$$\mathbf{M}^{(\beta)} = \frac{c^{(\beta)} D^{(\beta)}}{R\vartheta}\mathbf{1} = \frac{c_{\mathrm{R}}^{(\beta)} D^{(\beta)}}{JR\vartheta}\mathbf{1}\,, \tag{4.75}$$

where $D^{(\beta)}$ represents the scalar diffusivity for each chemical species.

We note that for the typical isomerization reaction, only the solvent is able to diffuse. Accordingly, the only mobility is that of the solvent and it takes the obvious form

$$\mathbf{M}^{(s)} = \frac{c_{\mathrm{R}}^{(s)} D^{(s)}}{JR\vartheta}\mathbf{1}\,.$$

4.5.8 Photochemical Reaction Rate

The propagation of suitable light through a polymeric gel activates the photochemical groups attached to the polymeric network, thus initiating photochemical reactions. To capture the reaction kinetics, we introduce the photochemical reaction rate, and specialize the forms for isomerization.

When irradiated with a UV light, the azobenzene chromophores undergo *cis-trans* photoisomerization, and the reverse is true, undergoing a *trans-cis* photoisomerization when irradiated with a visible light. For azobenzene, we denote the *cis-trans* photoisomerization as the forward reaction, and the *trans-cis* photoisomerization as the reverse reaction.

On the other hand, spirobenzopyran chromophores undergo a transformation from the open ring configuration to the closed configuration when irradiated with a visible light, and from the closed ring configuration to the open configuration in the absence of irradiation. For spirobenzopyran, we denote the open-to-closed ring as the forward reaction, and the closed-to-open ring as the reverse reaction.

As mentioned in Section 4.4, we assume the chemical affinity as the tendency of chemical species to participate in the reactions, and thus we consider it the driving force for the photochemical reactions. Following [89], and considering the balance of reactants/products in (4.27), we assume the rate of the photochemical reaction in the form

$$\dot{\xi} = k_f \frac{c^{(A)}}{N_A ch\nu} IA \; - k_b I^n c^{(B)}. \tag{4.76}$$

where k_f and k_b are the reaction rate coefficients of forward and backward photochemical reactions, respectively. In (4.76) N_A is Avogadro's number, c is the propagation speed of the radiation, and $h\nu$ is the energy of one photon with the frequency ν. Note that we introduce the exponent n in the reverse reaction term to account for the different mechanisms driving the reverse reaction mentioned above. For azobenzene (and other photosensitive groups that are reversed by irradiation), we take $n = 1$ and for spirobenzopyran (and other photosensitive groups that are active in the absence of irradiation) we take $n = 0$.

4.6 Governing Equations

The initial boundary value problem consists of the governing differential equations (4.23), (4.58) and (4.33), along with the boundary and initial conditions. Thus, in the absence of body forces, and neglecting the inertial effects, the governing equations in the deformed body $\mathcal{B}_t$ are:

- Balance of forces and moments

$$\begin{cases} \operatorname{div}\mathbf{T} = \mathbf{0} & \text{in } \mathcal{B}_t, \\ \mathbf{u} = \breve{\mathbf{u}} & \text{on } \mathcal{S}_{\mathbf{u}}, \\ \mathbf{T}\mathbf{n} = \breve{\mathbf{t}} & \text{on } \mathcal{S}_{\mathbf{t}}, \end{cases} \tag{4.77}$$

  Here, $\breve{\mathbf{u}}$ and $\breve{\mathbf{t}}$ are the prescribed displacement and surface traction on two complementary surfaces $\mathcal{S}_{\mathbf{u}}$ and $\mathcal{S}_{\mathbf{t}}$, respectively.

- Balance of species

  – Photoisomerization

$$\begin{cases} \dot{c}_{\mathrm{R}}^{(s)} = J\operatorname{div}\mathbf{j} & \text{in } \mathcal{B}_t, \\ \mu^{(s)} = \breve{\mu} & \text{on } \mathcal{S}_{\mu}, \\ \mathbf{j}^{(s)} \cdot \mathbf{n} = \breve{j} & \text{on } \mathcal{S}_{\mathbf{j}}, \end{cases} \tag{4.78}$$

Along with the evolution equations at each material point

$$\begin{aligned} \dot{c}_{\mathrm{R}}^{(A)} &= -\dot{\xi} \\ \dot{c}_{\mathrm{R}}^{(B)} &= \dot{\xi} \end{aligned} \tag{4.79}$$

- Radiative transfer

$$\begin{cases} \mathbf{d} \cdot \operatorname{grad} I + \Lambda I = 0 \quad \text{in } \mathcal{B}_t \,. \\ I = \breve{I} \quad \text{on } \mathcal{S}_- \,, \end{cases} \,. \tag{4.80}$$

Here, $\breve{I}$ is the prescribed light intensity on the irradiated surface $\mathcal{S}_-$

And the initial conditions are taken as

$$\mathbf{u}(\mathbf{x}_{\mathrm{R}}, t=0) = \mathbf{u}_0(\mathbf{x}_{\mathrm{R}}) \,, \quad \text{and} \quad \mu(\mathbf{x}_{\mathrm{R}}, t=0) = \mu_0(\mathbf{x}_{\mathrm{R}}) \tag{4.81}$$

in $\mathcal{B}_{\mathrm{R}}$, and there is no initial condition on $I(\mathbf{x}_{\mathrm{R}}, t=0)$ since (4.80) is steady and only depends on time via boundary conditions.

All together, this serves as a coupled initial boundary value problem for the displacement $\mathbf{u}(\mathbf{x}, t)$, the chemical potential $\mu(\mathbf{x}, t)$, and light intensity $I(\mathbf{x}, t)$.

4.7 Numerical Implementation

The balance laws presented in Subsection 4.3.4, form the governing set of coupled non-linear partial differential equations (PDEs). This set of coupled non-linear PDEs is solved numerically, employing the Newton-Raphson iterative procedure. Newton-Raphson method typically requires the development of weak forms for the boundary-velue problem and specification of the element-level residuals and tangents. The continuum framework, along with the constitutive model, is implemented in the [1] as a user element (UEL) subroutine.

4.7.1 Weak Forms

Based on the strong forms (4.77), (4.78) and (4.80), we obtain the relations more suitable for the numerical implementation, known as the weak forms. It is important to note that numerical solving the balance of forces and moments (4.77) and the balance of solvent content (4.78) we employ the standard Galerkin approach. However, due to the well known numerical difficulties concerning the first order hyperbolic PDEs, for the radiative transfer (4.80) we employ the stream upwind Petrov-Galerkin method (SUPG) (cf., e.g., [51]). The weak forms are as follows.

- Balance of forces and moments: First, we introduce the weighting field $\mathbf{w}_1$, such that it vanishes on $\mathcal{S}_{\mathbf{u}}$. Further, we apply the divergence theorem, and in the absence of body forces and inertial effects, we obtain the weak form of the boundary-value problem

$$\int_{\mathcal{B}_t} \left(\mathbf{T} : \frac{\partial \mathbf{w}_1}{\partial \mathbf{x}} \right) dv = \int_{\mathcal{S}_{\mathbf{t}}} \left(\mathbf{w}_1 \cdot \breve{\mathbf{t}} \right) da \,, . \tag{4.82}$$

- Balance of solvent content: Next to obtain the weak form for the balance of solvent content, we introduce a weighting field w_2, such that it vanishes on $\mathcal{S}_{\mu}$. After applying the divergence theorem, it can be rewritten in the form

$$\int_{\mathcal{B}_t} \left(\frac{w_2 \dot{\phi}}{J \Omega \phi^2} \right) dv = \int_{\mathcal{B}_t} \left(\mathbf{j} \cdot \frac{\partial w_2}{\partial \mathbf{x}} \right) dv + \int_{\mathcal{S}_{\omega}} \left(w_2 \breve{j} \right) da \,. \tag{4.83}$$

- Radiative transfer: Lastly, we develop the weak form for the radiative transfer

$$\int_{\mathcal{B}_t} \bar{w}_3 \left(\mathbf{d} \cdot \operatorname{grad} I + \Lambda I \right) dv = 0 \,. \tag{4.84}$$

  As previously mentioned, for numerical solving of first order hyperbolic PDE (4.80), we utilize the SUPG method, with the scalar weighting function

$$\bar{w}_3 = w_3 + \kappa \, \mathbf{d} \cdot \operatorname{grad} w_3 \,, \tag{4.85}$$

where w_3 is the weighting function used in the standard Galerkin approach, and κ is the stabilization parameter.

Element-Level Residuals Following the previous work by our group (cf., e.g., [18, 51, 9]), the body in its current configuration $\mathcal{B}_t$ is approximated using finite elements, such that $\mathcal{B}_t = \cup \mathcal{B}_t^e$. Further, the nodal degrees of freedom (DOF), displacement $\mathbf{u}$, chemical potential μ, and the light intensity I_0, are interpolated inside each element employing the shape functions

$$\mathbf{u} = \sum \mathbf{u}^A N^A \,, \quad \mu = \sum \mu^A N^A \quad \text{and} \quad I = \sum I^A N^A \,, \tag{4.86}$$

where the index $A = 1, 2, ...$ denotes the nodes of the element, $\mathbf{u}^A$ and μ^A are the nodal values of the displacement and the chemical potential, respectively, and N^A is the shape function.

First, following the standard Galerkin approach, in which the weighting functions $\mathbf{w}_1$ and w_2 are interpolated using the same shape functions,

$$\mathbf{w}_1 = \sum \mathbf{w}_1^A N^A \quad \text{and} \quad w_2 = \sum w_2^A N^A \,, \tag{4.87}$$

and based on the weak forms (4.82) and (4.83), we obtain the element-level residual for the displacement and the chemical potential

$$\begin{aligned} (\mathbf{R}_\mathbf{u})^A &= -\int_{\mathcal{B}_t^e} \left(\mathbf{T} \frac{\partial N^A}{\partial \mathbf{x}} \right) dv + \int_{\mathcal{S}_\mathbf{t}^e} \left(N^A \check{\mathbf{t}} \right) da \,, \\ (R_\mu)^A &= \int_{\mathcal{B}_t^e} \left(\frac{N^A \dot{\phi}}{J \Omega \phi^2} \right) dv + \int_{\mathcal{B}_t^e} \left(\mathbf{j} \cdot \frac{\partial N^A}{\partial \mathbf{x}} \right) dv + \int_{\mathcal{S}_\mathbf{j}^e} \left(N^A \check{j} \right) da \,. \end{aligned} \tag{4.88}$$

Next, employing the SUPG approach, the weighting field $\bar{w}_3$ is interpolated as

$$\bar{w}_3 = \sum \left(w_3^A N^A + w_3^A \, \kappa \, \mathbf{d} \mathrm{grad} \, N^A \right) \,. \tag{4.89}$$

Based on the weak form for the radiative transfer (4.84), the element-level residual for the light intensity takes the form

$$(R_I)^A = \int_{\mathcal{B}_t^e} N^A \left(\mathbf{d}\cdot\operatorname{grad} I + \Lambda I\right) dv + \int_{\mathcal{B}_t^e} \kappa \left(\mathbf{d}\cdot\operatorname{grad} N^A\right)\left(\mathbf{d}\operatorname{grad} I + \Lambda I\right) dv\,. \quad (4.90)$$

Element-Level Tangents In addition to the residuals, we provide the element-level tangents for the Newton-Raphson iterative solver. In case of the photo-chemo-mechanically coupled problem, we define nine tangents as follows.

$$\begin{aligned}
K^{AB}_{u_iu_k} &= -\frac{\partial R^A_{u_i}}{\partial u^B_k}\,, & K^{AB}_{u_i\mu} &= -\frac{\partial R^A_{u_i}}{\partial \mu^B}\,, & K^{AB}_{u_iI} &= -\frac{\partial R^A_{u_i}}{\partial I^B}\,,\\
K^{AB}_{\mu u_k} &= -\frac{\partial R^A_{\mu}}{\partial u^B_k}\,, & K^{AB}_{\mu\mu} &= -\frac{\partial R^A_{\mu}}{\partial \mu^B}\,, & K^{AB}_{\mu I} &= -\frac{\partial R^A_{\mu}}{\partial I^B}\,,\\
K^{AB}_{Iu_k} &= -\frac{\partial R^A_{I}}{\partial u^B_k}\,, & K^{AB}_{I\mu} &= -\frac{\partial R^A_{I}}{\partial \mu^B}\,, & K^{AB}_{II} &= -\frac{\partial R^A_{I}}{\partial I^B}\,.
\end{aligned} \quad (4.91)$$

Based on the displacement residual in (4.88), we obtain

$$\begin{aligned}
K^{AB}_{u_iu_k} &= \int_{\mathcal{B}_t^e} \frac{\partial N^A}{\partial x_j}\mathbb{A}_{ijkl}\frac{\partial N^B}{\partial x_l} dv - \int_{\mathcal{S}_{\mathfrak{t}}^e} N^A N^B \frac{\partial \breve{\mathfrak{t}}}{\partial u_k} da\,,\\
K^{AB}_{u_i\mu} &= \int_{\mathcal{B}^e} \frac{\partial N^A}{\partial x_j}\Big(\frac{\partial T_{ij}}{\partial \phi}\frac{\partial \phi}{\partial \mu}\Big) N^B dv\,.
\end{aligned} \quad (4.92)$$

Next, taking the derivatives of the chemical potential residual in the form presented in (4.88), the corresponding tangents are given as

$$\begin{aligned}
K^{AB}_{\mu u_k} &= -\int_{\mathcal{B}^e} \frac{\partial N^A}{\partial x_i}\Big(M_{il}\frac{\partial \mu}{\partial x_k}\Big)\frac{\partial N^B}{\partial x_l} dv\,,\\
K^{AB}_{\mu\mu} &= -\int_{\mathcal{B}^e} \frac{N^A N^B}{J\Omega\phi^2}\Big(2\frac{\dot\phi}{\phi}\frac{\partial \phi}{\partial \mu} - \frac{\partial \dot\phi}{\partial \mu}\Big) dv - \int_{\mathcal{B}^e}\Big(\frac{\partial j_i}{\partial \mu}\frac{\partial N^A}{\partial x_i}\Big) dv - \int_{\mathcal{S}_{\mathfrak{j}}^e}\Big(N^A N^B \frac{\partial \breve{\jmath}}{\partial \mu}\Big) da\,.
\end{aligned} \quad (4.93)$$

Finally, based on (4.90), we obtain the following set of tangents.

$$
\begin{aligned}
K_{Iu_i}^{AB} &= -\int_{\mathcal{B}^e} N^A \left[\left(d_i \frac{\partial I}{\partial x_j} + \Lambda I \right) \delta_{kl} - d_l \frac{\partial I}{\partial x_k} + \frac{\partial \Lambda}{\partial F_{kn}} F_{ln} I \right] \frac{\partial N^B}{\partial x_l} dv \\
&\quad - \int_{\mathcal{B}^e} \tau \left(d_i \frac{\partial N^A}{\partial x_i} \right) \left[\left(d_i \frac{\partial I}{\partial x_j} + \Lambda I \right) \delta_{kl} - d_l \frac{\partial I}{\partial x_k} + \frac{\partial \Lambda}{\partial F_{kn}} F_{ln} I \right] dv \,, \\
K_{II}^{AB} &= -\int_{\mathcal{B}^e} N^A \left(d_i \frac{\partial N^B}{\partial x_i} + \Lambda N^B + I \frac{\partial \Lambda}{\partial I} N^B \right) dv \\
&\quad - \int_{\mathcal{B}^e} \tau \left(d_i \frac{\partial N^A}{\partial x_i} \right) \left(d_i \frac{\partial N^B}{\partial x_i} + \Lambda N^B + I \frac{\partial \Lambda}{\partial I} N^B \right) dv \,.
\end{aligned}
\tag{4.94}
$$

It is worth noting the off-diagonal terms $K_{\mu I}$ and $K_{I\mu}$ have not been implemented here, since they only slightly contribute to the rate of convergence of the Newton-Raphson solver.

4.8 Numerical Simulations

4.8.1 Simulations Using Spirobenzopyran for Photoactivation

Material Point Level Simulations of Spirobenzopyran Isomerization Under Free Swelling Conditions In this section, we showcase the capabilities of our model to simulate the kinetics of photochemical reactions at a material point, along with its influence on the degree of swelling under free swelling conditions, for spirobenzopyran isomerization. The model is implemented in the form of a MATLAB code, and involves an explicit time integration for photochemical reactions.

Here, we employ our model to simulate the change in the amount of swelling due to irradiation, and calibrate the form for polymer-solvent interaction (4.64). In addition to our model, we utilize the MATLAB built-in least squares function `lsqnonlin` to determine the parameters χ_L, χ_H, Δ, and χ_T.

Experimental data The experimental data obtained by light irradiation of spirobenzopyran infused hydrogel from [81] is used to calibrate the model. The samples are irradiated with a light of intensity $I = 88.9\mathrm{W/m^2}$ over 45 minutes, and

during this period samples lost water and underwent shrinking. Next, after removing the light, the samples reswell, and are observed over the next 16 hours.

Here, we use the experimentally determined swelling stretch during irradiation, as well as the swelling stretch after removing the light source, shown in Figure 4.3a. Next, assuming chemical equilibrium $\mu = \mu_0$, and free swelling without mechanically applied deformation, the constitutive relation for chemical potential (4.69) yields

$$R\vartheta \left(\ln \left(1 - (\lambda^s)^{-3} \right) + (\lambda^s)^{-3} + \chi \, (\lambda^s)^{-6} \right) = 0 \, . \tag{4.95}$$

We then use (4.95) along with the experimentally measured swelling stretch to determine values of χ for all times in this experiment, and that data is shown in Figure 4.3b.

Simulation parameters To simulate the isomerization under free swelling conditions, initially the concentration of hydrophilic open-ring isomers is $c^{(\mathrm{A})}(\mathbf{x}_{\mathrm{R}}, t = 0) = 69.95$ mol/m^3, and we consider the concentration of hydrophobic closed-ring isomers $c^{(\mathrm{B})}(\mathbf{x}_{\mathrm{R}}, t = 0) = 0$ mol/m^3, and therefore the initial extent of the photochemical reaction $\xi(\mathbf{x}_{\mathrm{R}}, t = 0) = 0$. During the time interval $0 < t < 45$ min, the samples are being irradiated with the light intensity $I = 88.9$ W/m^2. At $t = 45$ min the light source is removed, and thus $I = 0$. And for the entire time $0 < t < 45$ min the photochemical reaction takes place and $\dot{\xi} > 0$. The parameters in use for the photochemical reaction kinetics in (4.76) are shown in Table 4.1.

Results The swelling stretch and the polymer-solvent interaction parameter obtained through model calibration are plotted on top of the experimental data in Figure 4.3a and 4.3b, respectively. The relative concentration of species and the extent of photochemical reaction are shown in Figures 4.3c and 4.3d, respectively. The calibrated polymer-solvent interaction parameters, along with the calibrated reaction coefficients, are shown in Table 4.2. As suggested by the experimental evidence,

Table 4.1 Photochemical Reaction Parameters.

N_A	$6.02{\cdot}10^{23}$ mol^{-1}
c	$2{\cdot}10^{8}$ m/s
h	$6.63{\cdot}10^{-34}$ J·s
ν	$1.11{\cdot}10^{15}$ Hz
n	0
H	$3.39{\cdot}10^{8}$ J/m^3

when irradiated, the spirobenzopyran chromophores undergo a transition from the open-ring to the closed-ring configuration. Our model successfully captured this process, and we notice the decrease in $c_{\mathrm{R}}^{(A)}$ during the irradiation, accompanied by the increase in $c_{\mathrm{R}}^{(B)}$. The simulated change in concentration of chemical species affects the polymer-solvent interaction, similar as in the experiments. Finally, the swelling stretch simulated by the calibrated model stands in a good agreement with the experimental observations.

Table 4.2 Calibrated Reaction Parameters, Along with the Polymer-Solvent Interaction Parameters for Photoisomerization of Spirobenzopyran Infused Hydrogel.

k_f	3.75 L^3·J^{-1}·mol^{-2}·s-1
k_b	$6\ {\cdot}10^{-5}$ L^2·J^{-1}·mol^{-1}·m^{-1}
χ_L	0.78
χ_H	6.64
ξ_T	0.99
Δ	0.37

Representative Simulation of a Photo-Activated Crawler With the constituive model calibrated for spirobenzopyram, we now move to showcase the usefulness of our model to simulate the motion of a photo-activated crawler developed by [81].

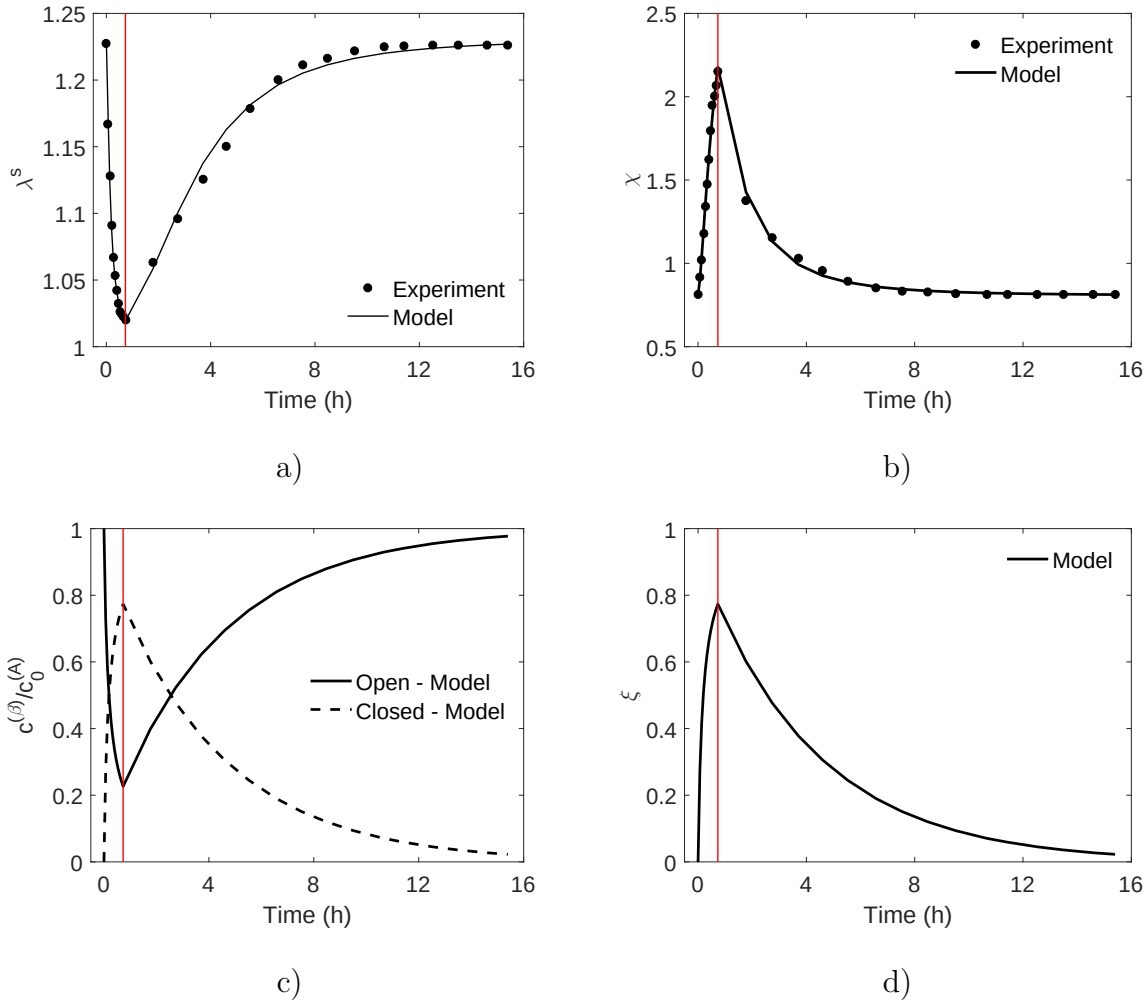

Figure 4.3 Calibration for spirobenzopyran photoisomerization. a) Experimentally determined swelling stretch from [81] with the calibrated model plotted on top of the experimental data. b) Experimentally based values for the polymer-solvent interaction parameter, along with the calibrated model. c) Relative concentration of the chemical species $c^{(\beta)}/c_0^{(A)}$. d) Extent of the photochemical reaction. In all cases, the red line marks the end of irradiation at $t = 45$ min on all four plots.

Design and operation In their recent study, [81] developed a 16 mm long and 0.5 mm thick crawler, with geometry shown in Figure 4.5. The device is manufactured from a hydrogel containing spiropyran photo-sensitive groups; and the operation of the photo-activated crawler consists of two distinct steps.

- Irradiation of the bottom surface for 30 minutes, with a light intensity of $I = 88.9\text{W/m}^2$. During this time period, the bottom surface begins to shrink, and the crawler undergoes bending due to the difference in the degree of swelling between the top and bottom surface.

- The light source is removed, and the motion of the crawler is observed over 10 hours. In the absence of light, the crawler undergoes reswelling, and during this time period the crawler flattens.

During the experiment, the crawler is placed on a ratcheted floor and utilizes the floor geometry to achieve the desired motion. The crawler motion is driven by the change in spacing between the crawler legs, which is coupled with the ratcheted floor to produce a one way motion.

Numerical simulation The finite element mesh consists of 104 three-dimensional user-defined elements applied on one quarter of the crawler geometry, with the boundary conditions shown in Figure 4.4. Symmetry boundary conditions are applied on the "1-3" and "2-3" planes denoted with dashed lines, and the displacement of node "N" is constrained along the "3" direction. As in the experiments, the crawler is swollen to equilibrium prior to light irradiation. It is then irradiated from the bottom over 30 minutes, with the light direction vector $\mathbf{d} = 1\mathbf{e}_3$ and intensity $I = 88.9\ \text{W/m}^2$. Lastly, the light is removed ($I = 0$ throughout the mesh) and the crawler is kept in dark for 10 hours.

In this simulation, we make use of the photochemical parameters and polymer-solvent interaction parameters obtained through calibration in Subsection 4.8.1.

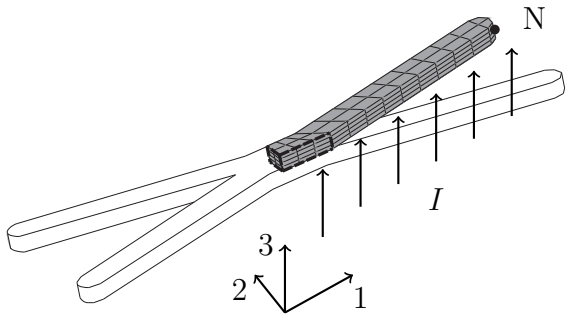

Figure 4.4 Crawler geometry ([81]), along with the finite element mesh and boundary conditions. The mesh is applied on one quarter of the crawler geometry, with the symmetry planes "1-3" and "2-3" denoted with dashed lines. Node "N" is located at the tip of the crawler leg and its displacement is constrained along the "3" direction. Light is applied along the "3" direction.

While the photochemical behavior has been thoroughly investigated, along with the small-deformation mechanical response, the large-deformation mechanical behavior is yet to be characterized. Therefore, based on the dynamic mechanical analysis (DMA) data found in [81] we choose the initial shear modulus of the same order of magnitude as the storage modulus $G_0 = 10$ kPa, along with the locking stretch $\lambda_L = 10$, which is very reasonable for this class of material. It is also worth noting the friction between the floor and the crawler legs is undetermined, and thus we neglect the ratcheted floor geometry and focus only on the overall body motion caused by the nonuniform drying and reswelling.

Results Numerical simulation results have shown the photo-activated crawler undergoing bending motion during 30 minutes of light irradiation. During this time period, the spacing between the crawler legs decreases from the initial 15.5 mm to approximately 8.52 mm, as in Figure 4.4a. A similar motion has also been experimentally observed in the operation of a photo-activated crawler. Further, after 10 hours in the absence of light, the crawler flattens as shown in the Figure 4.5b. The simulation have shown the spacing between the legs is restored to approximately 15.5

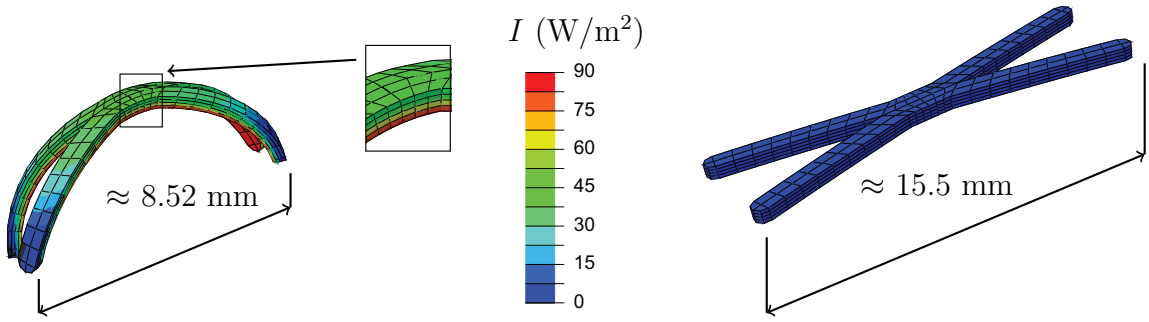

Figure 4.5 Numerical simulation of a crawler developed by [81] after a) 30 minutes of light iraddiation and b) 10 hours in the basence of light. During the light irradiation, the crawler bends and the spacing between the legs decreases from 15.5 mm to approximately 8.52 mm, similar to the one observed in the experiments. After 10 hours in the absence of light, the crawler flattens, and the spacing between the legs almost completely returns to the initial 15.5 mm. The contour represents the light intensity.

mm, as in the experiments, which produces a motion very similar to the experiments [81].

4.8.2 Simulations Using Azobenzene for Photoactivation

4.8.3 Material Point Level Simulation of Azobenzene Isomerization Under Free Swelling Conditions

In this section we employ the same approach as in Subsection 4.8.1 to simulate the photochemical reaction kinetics and calibrate for the polymer-solvent interaction parameters.

Experiments The experimental data from [118] is used for model calibration, and the obtained swelling stretch is shown in Figure 4.6a. The samples used in this set of experiments are 200 μm in diameter slide-rings containing 4.8 mol/m^3 of Azobenzene ([121]). The samples are first irradiated with a visible light for approximately 1 hour, undergoing shrinking. Subsequently, samples are irradiated with a UV light over 1 hour, and during this period the samples reswell. Further, spectroscopy measurements

determined the level of isomerization reaction around 80-90%, corresponding to an extent of the photochemical reaction similarly around $\xi = 0.8 - 0.9$.

It is important to note when reswelling reaches equilibrium (after approximately 15 minutes), the samples undergo gradual shrinking. This phenomenon is common in slide-rings, and the reader is referred to [118]. In this work, we neglect this phenomena, and strictly focus attention on the reswelling induced by UV irradiation.

Simulation parameters The isomerization of the azobenzene is simulated under free swelling conditions. The initial concentration of *cis* isomers is $\mathrm{c}^{(A)}(\mathbf{x}_{\mathrm{R}}, t = 0) = 4.8$ mol/m^3 as in the experiments; and the initial concentration of *trans* isomers is $\mathrm{c}^{(B)}(\mathbf{x}_{\mathrm{R}}, t = 0) = 0$ mol/m^3, leading to the initial extent of the photochemical reaction $\xi(\mathbf{x}_{\mathrm{R}}, t = 0) = 0$. Since the light intensity is not specified, we take $I = 100$ W/m^2 throughout the simulation. As mentioned in Subsection 4.5.8, we take $n = 1$ in this case to account tor the backward reaction rate that is only active due to UV irradiation. The remaining photochemical reaction parameters used in simulation are provided in Table 4.1.

Results In Figure 4.6a and 4.6b we show the swelling stretch and the polymer-solvent interaction parameter, respectively, with the calibrated model plotted on top of the experimental data. Figure 4.6c shows the relative concentration of chemical species. The extent of the photochemical reaction is presented in Figure 4.6d. The calibrated values for the forward and backward reaction coefficients, as well as the polymer-solvent interaction parameters, are shown in Table 4.3. The simulation successfully captures the *cis-trans* isomerization taking place when irradiated with a visible light, and also the *trans-cis* isomerization when irradiated with a UV light. However, the maximum extent of reaction $\xi_{\max} = 0.69$ is slightly lower then the one observed in spectroscopy measurements. Finally, the calibrated polymer-solvent

interaction parameter is in good agreement with the experimental data, as well as the swelling stretch predicted by the calibrated model.

4.8.4 Representative Simulation of a Photo-Responsive Actuator

In this section we utilize our calibrated model, along with the finite element code to simulate the operation of a photo-responsive actuator.

Design and operation Photo-responsive actuators are commonly used in literature to illustrate the capabilities and applications of photo-sensitive gels (cf., e.g., [125, 79]). These proof of concept devices are typically manufactured in the form of a sheet, clamped on one side, and irradiated from one light source, much like cantilever in Figure 4.7. The operation of these devices usually consists of two steps.

- Irradiation with visible light. During this step, the irradiated side shrinks, and the actuator undergoes a bending motion.
- Irradiataion with UV light. During this step the irradiated side reswells and the actuator moves back towards the initial configuration.

Numerical simulation We model the actuator as a 10 mm by 45 mm rectangular sheet, with a 2 mm thickness. The finite element mesh consists of 69 three-dimensional user elements applied on one half of the actuator geometry. The device is held on the right side, and the boundary conditions are shown in Figure 4.7, with the "2-3"symmetry plane denoted with a dashed line. The light is prescribed with an intensity $I = 100$ W/m^2 and a direction vector $\mathbf{d} = -\mathbf{e}_3$. First, the actuator is irradiated with a visible light over 60 seconds. Next, the device is irradiated with a UV light over 1400 seconds. The polymer-solvent interaction parameters, as well as the photochemical reaction coefficients, are obtained through model calibration in

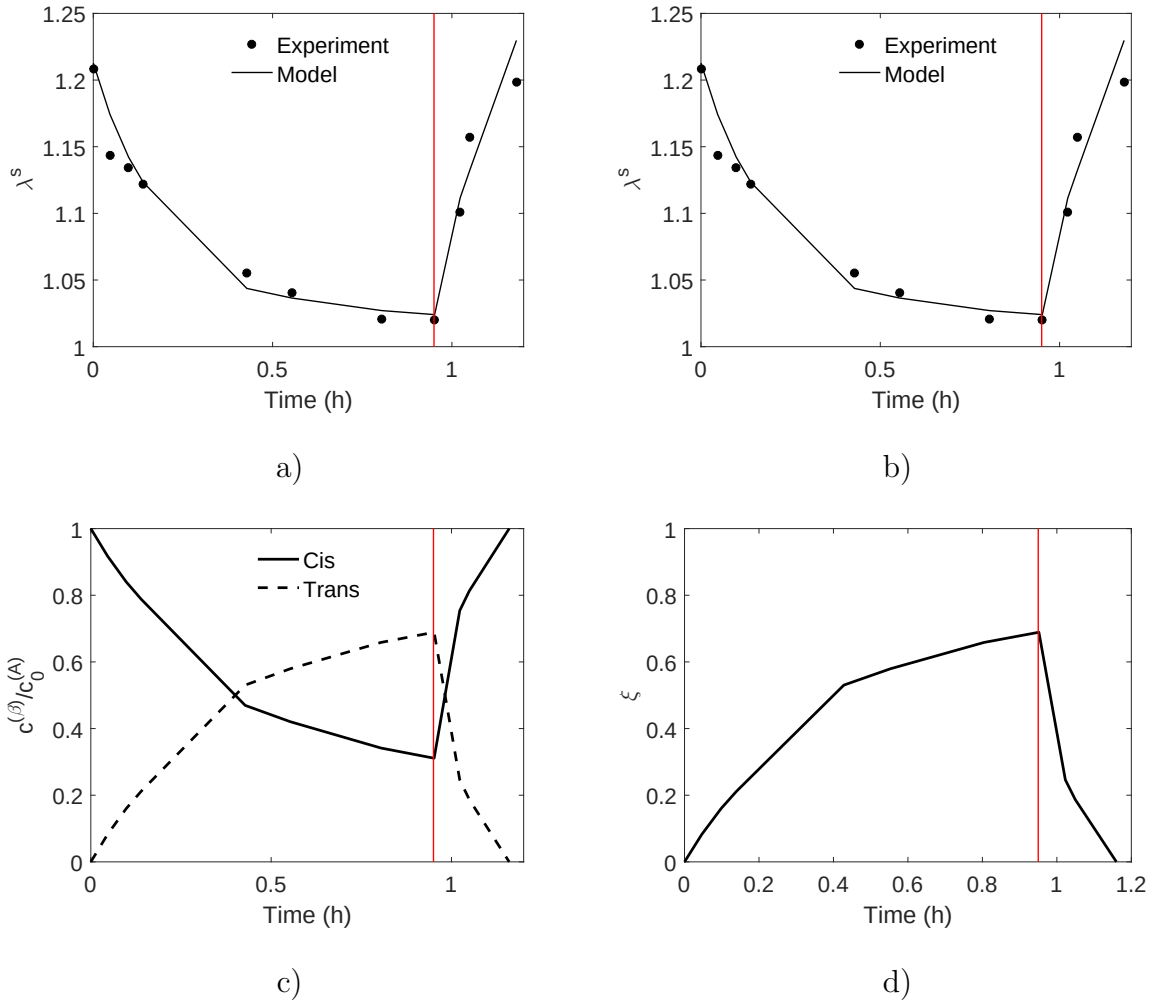

Figure 4.6 Calibration for azobenzene isomerization. a) Experimentally determined swelling stretch from [118]. Calibrated model is plotted on top of the experimental data. b) Experimentally based values for the polymer-solvent mixing parameter, along with the calibrated model. c) Relative concentration of chemical species $c^{(\beta)}/c_0^{(A)}$. d) Extent of the photochemical reaction. Red line denotes the end of irradiation with a visible light and the beginning of UV irradiation.

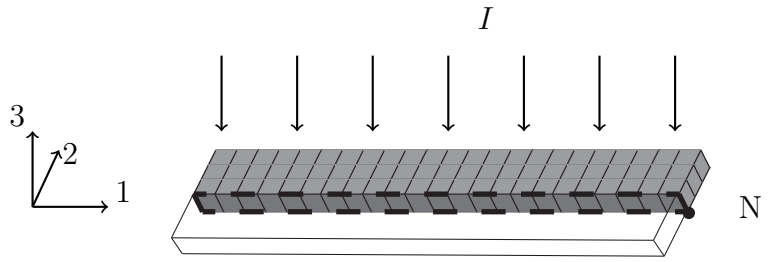

Figure 4.7 Actuator geometry, along with the finite element mesh and boundary conditions used to simulate its operation. The mesh is applied on one half of the geometry, with the symmetry plane "1-3" denoted with dashed lines. The displacement of the top surface is constrained along the "1" direction, and the displacement of node "N" is fully constrained. Light is applied along the "3" direction.

Subsection 4.8.3 and shown in Table 4.3. We take the mechanical material parameters to be the same as in Subsection 4.8.1, i.e. $G_0 = 1$ MPa and $\lambda_L = 10$.

Results The forward reaction takes place during 60 seconds of irradiation with a visible light. During this time period due to uneven shrinking between the top and bottom surface, the photo-responsive actuator undergoes a bending motion. The deformed configuration is shown in Figure 4.8a. Further, after 1400 seconds of UV irradiation the photo-actuator reswells and almost completely returns to the initial configuration, as in Figure 4.8b. Similar response has been observed in the experiments, and our numerical simulation successfully captures the operation of a photo-responsive actuator.

4.9 Concluding Remarks

We have developed a multiphysics continuum-level framework, along with the constitutive model which takes into account the photo-chemo-mechanically coupled behavior of polymeric gels. The developed model is aimed to capture the experimentally observed irradiation effects on the amount of swelling of polymeric gels.

The mechanical response of the polymeric gel is accounted for using the non-Gaussian statistical mechanics based model. To account for the mixing between the

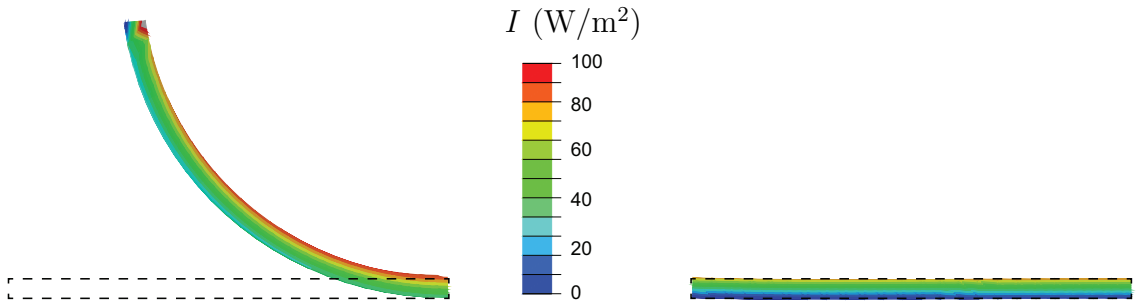

Figure 4.8 Numerical simulation of a photo-responsive actuator. a) Results are obtained after 60 seconds of irradiation with a visible light showing the device undergoing bending motion due to the difference in the degree of swelling between the top and bottom surfaces. b) Results after 1400 seconds under UV light irradiation. The actuator almost completely returns to the initial shape. In both, the contour represents the light intensity.

polymeric network and the solvent we employ the Flory-Huggins model. To model the kinetics of photochemical reactions we adopt a form which takes into account the light intensity, the concentration of chemical species and the chemical affinity.

The model is calibrated against the experimental data found in literature, and is in good agreement with the experimental observations. Further, the continuum framework, along with the constitutive model, is numerically implemented in the finite element software package Abaqus/Standard by writing a UEL subroutine. Finally, the numerical implementation allowed for reliable simulation of photo-sensitive gel response for use in a crawler and actuator device.

Table 4.3 Calibrated Reaction Parameters, Along with the Polymer-Solvent Interaction Parameters for Photoisomerization of Azobenzene Infused Hydrogel.

k_f	1.46 $L^3 \cdot J^{-1} \cdot mol^{-2} \cdot s-1$
k_b	2.51 $\cdot 10^{-5}$ $L^2 \cdot J^{-1} \cdot mol^{-1} \cdot m^{-1}$
χ_L	0.56
χ_H	5.30
ξ_T	0.97
Δ	0.70

APPENDIX A

VERIFICATION OF THE DIC PROCEDURE

To verify the validity of the DIC procedure applied for the testing inside the cylindrical fluid bath, we perform a set of mechanical tests both with and without the fluid bath. First, virgin samples without the fluid bath are tested using the same setup described in Subsection 2.3.1. Another set of virgin samples (without swelling in solvent) are tested using the fluid bath full of water, and tested using the same procedure. In all cases a prescribed displacement of $u = 20.32\,\text{mm}$ at a rate of $\dot{u} = 20.32 \times 10^{-4}\,\text{mm/s}$ is prescribed to the testing machine, which corresponds to a mechanical stretch of $\lambda^m = 2$ at a stretch rate of 10^{-4}s^{-1}. The results presented in Figure A.1 clearly show only a very small difference between the DIC measurements obtained with and without the cylindrical fluid bath, with a maximum error in the measured mechanical stretch of 0.025, which is 1.25%. Therefore, we freely use DIC to measure the deformation of samples with the fluid bath.

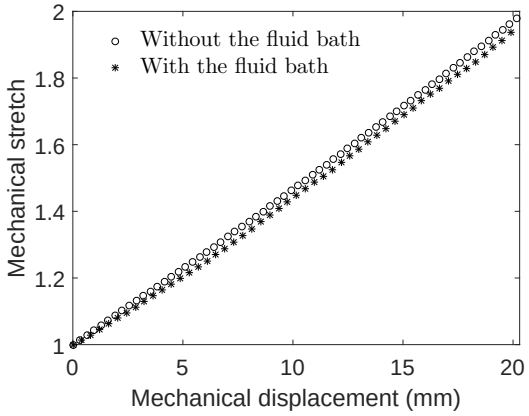

Figure A.1 Comparison of the the DIC measured mechanical stretch λ^m on unswollen samples as a function of the mechanical displacement prescribed to the testing machine with and without the fluid bath.

APPENDIX B

BUOYANCY CALIBRATION

To account for the effect of buoyancy due to the submerged grip, load train, and sample, we perform a calibration test to determine the change in force per unit depth (N/m) due to buoyancy. This calibration may then be applied to the measured force signal to remove the effect of buoyancy so our reported stress is only what is due to the material response. To perform the calibration, we keep the sample attached only to the top grip, and do not attach the sample to the bottom grip. The sample, along with the grip and load train is fully submerged inside the fluid bath, with the load cell recording the force due to buoyancy at various depths. Since the calibration depends on the water level, care must be taken to ensure the same fill level is used in the experiments as was used in the calibration.

Since the grips and the load train used for a 5-pound load cell are not the same as the one in use for the 100 gram load cell, the above mentioned procedure is applied for each of them separately. The measured calibration factor is 1.11 N/m for the 5 pound load cell setup, and 0.64 N/m for the 100 gram load cell setup.

APPENDIX C

FINITE-ELEMENT VERIFICATION

The UEL is verified by comparing analytically tractable solutions against our numerical simulations. Due to the complexity of the fully coupled-scheme in this work, the verifications are done separately on mechanical and diffusion part, respectively. Here, we put our emphasis on the mechanical verification for the inclusion of fibers since the details verifying the diffusion aspects of the UEL have been previously reported in [18].

For the mechanical verification, a simple shear motion is prescribed on a cubic gel embedded with one fiber family with a referential direction of $\mathbf{a}_{\mathrm{R}}$, the schematic is shown in Figure C.1a. According to [50], the corresponding deformation is given by

$$\left[\mathbf{F}\right] = \begin{bmatrix} 1 & \gamma & 0 \\ 0 & 1 & 0 \\ 0 & 0 & 1 \end{bmatrix}, \tag{C.1}$$

where $\gamma = \tan\theta$ denotes the amount of shear. The referential fiber's orientation may be written in the form

$$\mathbf{a}_{\mathrm{R}} = [a_1, a_2, 0]^{\top}, \tag{C.2}$$

with a_1 and a_2 denote components in the x_1 and x_2 directions, respectively. Also, to make $\mathbf{a}_{\mathrm{R}}$ a unit vector, the constraint of $\sqrt{a_1^2 + a_2^2} = 1$ has to be fulfilled. After taking the tensor product operation of $\mathbf{a}_{\mathrm{R}}$, the structure tensor $\mathbf{A}_{\mathrm{R}}$ is given by

$$\left[\mathbf{A}_{\mathrm{R}}\right] = \begin{bmatrix} a_1^2 & a_1 a_2 & 0 \\ a_1 a_2 & a_2^2 & 0 \\ 0 & 0 & 0 \end{bmatrix}. \tag{C.3}$$

Next, two further assumptions are made: 1) The complete incompressibility (i.e., $J = 1$) is assumed for the analytical solution, and 2) no fluid is present (i.e. $\phi = 1$). Under these assumptions, the Cauchy stress in (3.41) is now given by

$$\mathbf{T} = (1 - f_{\mathrm{R}})(G\mathbf{B} - P\mathbf{1}) + 2f_{\mathrm{R}}E(I_4 - 1)(\mathbf{F}\mathbf{A}_{\mathrm{R}}\mathbf{F}^{\top}) \tag{C.4}$$

with

$$\left.\begin{aligned} G &= \frac{1}{3}G_0\left(\frac{3 - (\bar{\lambda}/\lambda_L)^2}{1 - (\bar{\lambda}/\lambda_L)^2}\right) \text{ and } \\ I_4 &= a_1^2 + 2a_1a_2\gamma + (1 + \gamma^2)a_2^2. \end{aligned}\right\} \tag{C.5}$$

Note that P in (C.4) denotes a constitutively indeterminate pressure, which is introduced to satisfy the incompressibility constraint.

For material parameters, we again use the same parameters that are shown in Table 3.1 and a volume fraction $f_{\mathrm{R}} = 0.5$ for the fibers. On the numerical side, to approximate a nearly incompressible material we take $K = 10^3 G_0$. Since we are interested in verifying the mechanical response in the presence of fibers, we take three independent cases, $\mathbf{a}_{\mathrm{R}} = [1, 0, 0]^{\top}$, $\mathbf{a}_{\mathrm{R}} = [1/\sqrt{2}, 1/\sqrt{2}, 0]^{\top}$, and $\mathbf{a}_{\mathrm{R}} = [0, 1, 0]^{\top}$, to investigate different initial fiber orientations.

Figure C.1 compares the analytical with a single element (U3D8) simulation for the shear stress and normal stress difference given by

$$T_{12} = (1 - f_{\mathrm{R}})G\gamma + 2f_{\mathrm{R}}E(I_4 - 1)(a_1a_2 + a_2^2\gamma) \tag{C.6}$$

and,

$$T_{11} - T_{33} = (1 - f_{\mathrm{R}})G\gamma^2 + 2f_{\mathrm{R}}E(I_4 - 1)(a_1^2 + 2a_1a_2\gamma + a_2^2\gamma^2) \tag{C.7}$$

respectively, against the numerical solutions. We note that the stress is normalized by the initial shear modulus G_0, and the cases $\mathbf{a}_{\mathrm{R}} = [1, 0, 0]^{\top}$, $\mathbf{a}_{\mathrm{R}} = [1/\sqrt{2}, 1/\sqrt{2}, 0]^{\top}$, and $\mathbf{a}_{\mathrm{R}} = [0, 1, 0]^{\top}$, are shown in Figure C.1b, c and d, respectively. The solid and dashed

lines represent the analytical solutions, and the markers the numerically calculated results. It is worth mentioning that the case with the referential fiber orientation of $\mathbf{a}_{\mathrm{R}} = [1, 0, 0]^{\top}$ does not involve stretching along the fiber direction, which makes the model exhibit a pure hyperelastic response. Finally, the good agreement between analytical and numerical results indicate the mechanical portion including fibers of our finite element implementation is verified.

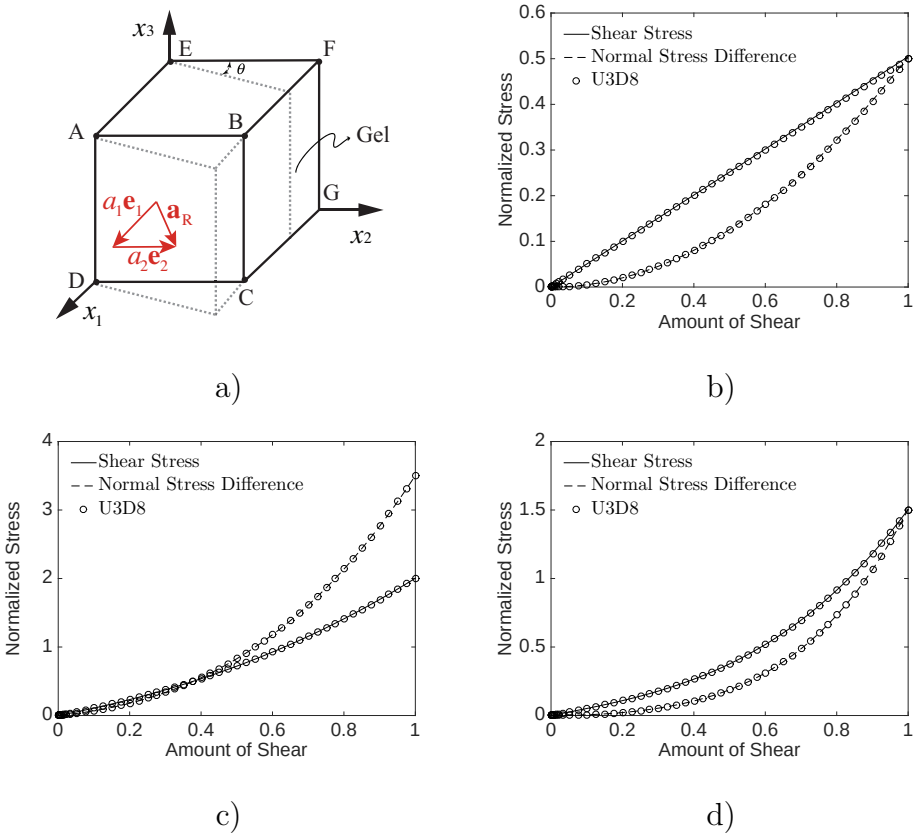

Figure C.1 Comparison between analytical and numerical solutions for simple shear deformation. a) Schematic of a cubic gel with a single fiber family embedded with referential orientation $\mathbf{a}_{\mathrm{R}}$ undergoing simple shear deformation. The normalized stress T_{12}/G_0 and normal stress difference $(T_{11} - T_{33})/G_0$ is plotted against the amount of shear $\gamma = \tan\theta$ for different fiber orientations b) $\mathbf{a}_{\mathrm{R}} = [1, 0, 0]^{\top}$, c) $\mathbf{a}_{\mathrm{R}} = [1/\sqrt{2}, 1/\sqrt{2}, 0]^{\top}$, and d) $\mathbf{a}_{\mathrm{R}} = [0, 1, 0]^{\top}$.

REFERENCES

[1] Abaqus/Standard. *Abaqus Reference Manuals*. Dassault Systemes Simulia, Providence, RI, 2018.

[2] M. Agoras, O. Lopez-Pamies, and P. P. Castañeda. A general hyperelastic model for incompressible fiber-reinforced elastomers. *Journal of the Mechanics and Physics of Solids*, 57(2):268–286, 2009.

[3] L. Anand. A constitutive model for compressible elastomeric solids. *Computational Mechanics*, 18(5):339–355, 1996.

[4] E. Andrzejewska. Photopolymerization kinetics of multifunctional monomers. *Progress in polymer science*, 26(4):605–665, 2001.

[5] E. M. Arruda and M. C. Boyce. A three-dimensional constitutive model for the large stretch behavior of rubber elastic materials. *Journal of the Mechanics and Physics of Solids*, 41(2):389–412, 1993.

[6] E. Bat, B. H. Kothman, G. A. Higuera, C. A. van Blitterswijk, J. Feijen, and D. W. Grijpma. Ultraviolet light crosslinking of poly (trimethylene carbonate) for elastomeric tissue engineering scaffolds. *Biomaterials*, 31(33):8696–8705, 2010.

[7] D. J. Beebe, J. S. Moore, J. M. Bauer, Q. Yu, R. H. Liu, C. Devadoss, and B.-H. Jo. Functional hydrogel structures for autonomous flow control inside microfluidic channels. *Nature*, 404(6778):588–590, 2000.

[8] M. A. Biot. Theory of stress-strain relations in anisotropic viscoelasticity and relaxation phenomena. *Journal of Applied Physics*, 25(11):1385–1391, 1954.

[9] N. Bosnjak, S. Wang, D. Han, H. Lee, and S. A. Chester. Modeling of fiber-reinforced polymeric gels. *Mechanics Research Communications*, 96:7–18, 2019.

[10] J. C. Breger, C. Yoon, R. Xiao, H. R. Kwag, M. O. Wang, J. P. Fisher, T. D. Nguyen, and D. H. Gracias. Self-folding thermo-magnetically responsive soft microgrippers. *ACS applied materials & interfaces*, 7(5):3398–3405, 2015.

[11] S. Cantournet, M. Boyce, and A. Tsou. Micromechanics and macromechanics of carbon nanotube-enhanced elastomers. *Journal of the Mechanics and Physics of Solids*, 55(6):1321–1339, 2007.

[12] V. Chan, K. Park, M. B. Collens, H. Kong, T. A. Saif, and R. Bashir. Development of miniaturized walking biological machines. *Scientific reports*, 2:857, 2012.

[13] S. Chandrasekhar. *Radiative transfer*. Courier Corporation, 2013.

[14] X. Chen, H. Li, and K. Lam. A multiphysics model of photo-sensitive hydrogels in response to light-thermo-ph-salt coupled stimuli for biomedical applications. *Bioelectrochemistry*, page 107584, 2020.

[15] S. A. Chester. A constitutive model for coupled fluid permeation and large viscoelastic deformation in polymeric gels. *Soft Matter*, 8(31):8223–8233, 2012.

[16] S. A. Chester and L. Anand. A coupled theory of fluid permeation and large deformations for elastomeric materials. *Journal of the Mechanics and Physics of Solids*, 58(11):1879–1906, 2010.

[17] S. A. Chester and L. Anand. A thermo-mechanically coupled theory for fluid permeation in elastomeric materials: application to thermally responsive gels. *Journal of the Mechanics and Physics of Solids*, 59(10):1978–2006, 2011.

[18] S. A. Chester, C. V. Di Leo, and L. Anand. A finite element implementation of a coupled diffusion-deformation theory for elastomeric gels. *International Journal of Solids and Structures*, 52:1–18, 2015.

[19] N. Cohen and R. M. McMeeking. On the swelling induced microstructural evolution of polymer networks in gels. *Journal of the Mechanics and Physics of Solids*, 125:666–680, 2019.

[20] N. Cohen, S. S. Oren, and G. deBotton. The evolution of the dielectric constant in various polymers subjected to uniaxial stretch. *Extreme Mechanics Letters*, 16:1–5, 2017.

[21] B. Coudrillier, C. Boote, H. A. Quigley, and T. D. Nguyen. Scleral anisotropy and its effects on the mechanical response of the optic nerve head. *Biomechanics and modeling in mechanobiology*, 12(5):941–963, 2013.

[22] B. Coudrillier, J. Tian, S. Alexander, K. M. Myers, H. A. Quigley, and T. D. Nguyen. Biomechanics of the human posterior sclera: age-and glaucoma-related changes measured using inflation testing. *Investigative ophthalmology & visual science*, 53(4):1714–1728, 2012.

[23] M. J. Crochet and P. M. Naghdi. A class of simple solids with fading memory. *International Journal of Engineering Science*, 7(12):1173–1198, 1969.

[24] M. Czugala, C. O'Connell, C. Blin, P. Fischer, K. J. Fraser, F. Benito-Lopez, and D. Diamond. Swelling and shrinking behaviour of photoresponsive phosphonium-based ionogel microstructures. *Sensors and Actuators B: Chemical*, 194:105–113, 2014.

[25] B. Davis. Diffusion in polymer gel implants. *Proceedings of the National Academy of Sciences*, 71(8):3120–3123, 1974.

[26] E. de Souza Neto, D. Perić, M. Dutko, and D. Owen. Design of simple low order finite elements for large strain analysis of nearly incompressible solids. *International Journal of Solids and Structures*, 33(20-22):3277–3296, 1996.

[27] M. Dehghany, H. Zhang, R. Naghdabadi, and Y. Hu. A thermodynamically-consistent large deformation theory coupling photochemical reaction and electrochemistry for light-responsive gels. *Journal of the Mechanics and Physics of Solids*, 116:239–266, 2018.

[28] K. Deligkaris, T. S. Tadele, W. Olthuis, and A. van den Berg. Hydrogel-based devices for biomedical applications. *Sensors and Actuators B: Chemical*, 147(2):765–774, 2010.

[29] M. Doi. Gel dynamics. *Journal of the Physical Society of Japan*, 78(5):052001–052001, 2009.

[30] A. Dorfmann and R. Ogden. Nonlinear electroelasticity. *Acta Mechanica*, 174(3-4):167–183, 2005.

[31] A. Drozdov et al. Thermo-viscoelastic and viscoplastic behavior of high-density polyethylene. *International Journal of Solids and Structures*, 45(14-15):4274–4288, 2008.

[32] A. D. Drozdov. A constitutive model for nonlinear viscoelastic media. *International Journal of Solids and Structures*, 34(21):2685–2707, 1997.

[33] A. D. Drozdov and A. Dorfmann. The nonlinear viscoelastic response of carbon black-filled natural rubbers. *International journal of solids and structures*, 39(23):5699–5717, 2002.

[34] F. P. Duda, A. C. Souza, and E. Fried. A theory for species migration in a finitely strained solid with application to polymer network swelling. *Journal of the Mechanics and Physics of Solids*, 58(4):515–529, 2010.

[35] C. Durning and K. Morman Jr. Nonlinear swelling of polymer gels. *The Journal of chemical physics*, 98(5):4275–4293, 1993.

[36] F.-R. Fan, L. Lin, G. Zhu, W. Wu, R. Zhang, and Z. L. Wang. Transparent triboelectric nanogenerators and self-powered pressure sensors based on micropatterned plastic films. *Nano letters*, 12(6):3109–3114, 2012.

[37] M. Farshad and M. Le Roux. Compression properties of magnetostrictive polymer composite gels. *Polymer testing*, 24(2):163–168, 2005.

[38] S. L. Fenn and R. A. Oldinski. Visible light crosslinking of methacrylated hyaluronan hydrogels for injectable tissue repair. *Journal of Biomedical Materials Research Part B: Applied Biomaterials*, 104(6):1229–1236, 2016.

[39] J. D. Ferry. *Viscoelastic properties of polymers*. John Wiley & Sons, 1980.

[40] L. Fetters, D. Lohse, D. Richter, T. Witten, and A. Zirkel. Connection between polymer molecular weight, density, chain dimensions, and melt viscoelastic properties. *Macromolecules*, 27(17):4639–4647, 1994.

[41] G. Filipcsei, K. Sumaru, T. Takagi, T. Kanamori, and M. Zrinyi. Swelling degree and shape change of photo-and thermo-response of spirobenzopyran-functionalized porous pnipaam hydrogels. *Journal of Molecular Liquids*, 189:63–67, 2014.

[42] P. Flory. Principles of polymer chemistry (cornell univ. press, ithaca, 1953); huggins p. *J. Chem. Phys*, 9:440, 1941.

[43] P. J. Flory. Thermodynamics of high polymer solutions. *The Journal of chemical physics*, 10(1):51–61, 1942.

[44] P. J. Flory and J. Rehner. Statistical mechanics of cross-linked polymer networks ii. swelling. *The journal of chemical physics*, 11(11):521–526, 1943.

[45] P. J. Flory and J. Rehner. Statistical theory of chain configuration and physical properties of high polymers. *Annals of the New York Academy of Sciences*, 44(4):419–429, 1943.

[46] R. Fuhrer, E. K. Athanassiou, N. A. Luechinger, and W. J. Stark. Crosslinking metal nanoparticles into the polymer backbone of hydrogels enables preparation of soft, magnetic field-driven actuators with muscle-like flexibility. *Small*, 5(3):383–388, 2009.

[47] M. Galli, K. S. Comley, T. A. Shean, and M. L. Oyen. Viscoelastic and poroelastic mechanical characterization of hydrated gels. *Journal of Materials Research*, 24(3):973–979, 2009.

[48] X. Gong, K. Yang, J. Xie, Y. Wang, P. Kulkarni, A. S. Hobbs, and A. D. Mazzeo. Rotary actuators based on pneumatically driven elastomeric structures. *Advanced Materials*, 28(34):7533–7538, 2016.

[49] M. Green and A. Tobolsky. A new approach to the theory of relaxing polymeric media. *The Journal of Chemical Physics*, 14(2):80–92, 1946.

[50] M. E. Gurtin, E. Fried, and L. Anand. *The mechanics and thermodynamics of continua*. Cambridge University Press, 2010.

[51] C. M. Hamel, F. Cui, and S. A. Chester. A finite element method for light activated shape-memory polymers. *International Journal for Numerical Methods in Engineering*, 111(5):447–473, 2017.

[52] D. Han, C. Farino, C. Yang, T. Scott, D. Browe, W. Choi, J. W. Freeman, and H. Lee. Soft robotic manipulation and locomotion with a 3d printed electroactive hydrogel. *ACS applied materials & interfaces*, 2018.

[53] D. Han, Z. Lu, S. A. Chester, and H. Lee. Micro 3d printing of a temperature-responsive hydrogel using projection micro-stereolithography. *Scientific reports*, 8(1):1963, 2018.

[54] M. Hasegawa. Photopolymerization of diolefin crystals. *Chemical Reviews*, 83(5):507–518, 1983.

[55] K. Hayamizu, Y. Aihara, S. Arai, and W. S. Price. Diffusion, conductivity and dsc studies of a polymer gel electrolyte composed of cross-linked peo, γ-butyrolactone and libf4. *Solid State Ionics*, 107(1-2):1–12, 1998.

[56] G. A. Holzapfel. *Nonlinear Solid Mechanics: A Continuum Approach for Engineering*. Wiley, 2000.

[57] G. A. Holzapfel and T. C. Gasser. A viscoelastic model for fiber-reinforced composites at finite strains: Continuum basis, computational aspects and applications. *Computer methods in applied mechanics and engineering*, 190(34):4379–4403, 2001.

[58] W. Hong, X. Zhao, J. Zhou, and Z. Suo. A theory of coupled diffusion and large deformation in polymeric gels. *Journal of the Mechanics and Physics of Solids*, 56(5):1779–1793, 2008.

[59] M. Hossain, D. K. Vu, and P. Steinmann. Experimental study and numerical modelling of vhb 4910 polymer. *Computational Materials Science*, 59:65–74, 2012.

[60] M. Hossain, D. K. Vu, and P. Steinmann. A comprehensive characterization of the electro-mechanically coupled properties of vhb 4910 polymer. *Archive of Applied Mechanics*, 85(4):523–537, 2015.

[61] Y. Hu and Z. Suo. Viscoelasticity and poroelasticity in elastomeric gels. *Acta Mechanica Solida Sinica*, 25(5):441–458, 2012.

[62] Y. Hu, X. Zhao, J. J. Vlassak, and Z. Suo. Using indentation to characterize the poroelasticity of gels. *Applied Physics Letters*, 96(12):121904, 2010.

[63] X. Huang and C. S. Brazel. On the importance and mechanisms of burst release in matrix-controlled drug delivery systems. *Journal of controlled release*, 73(2):121–136, 2001.

[64] M. L. Huggins. Some properties of solutions of long-chain compounds. *The Journal of Physical Chemistry*, 46(1):151–158, 1942.

[65] F. Ilievski, A. D. Mazzeo, R. F. Shepherd, X. Chen, and G. M. Whitesides. Soft robotics for chemists. *Angewandte Chemie*, 123(8):1930–1935, 2011.

[66] M. Jamal, S. S. Kadam, R. Xiao, F. Jivan, T.-M. Onn, R. Fernandes, T. D. Nguyen, and D. H. Gracias. Bio-origami hydrogel scaffolds composed of photocrosslinked peg bilayers. *Advanced healthcare materials*, 2(8):1142–1150, 2013.

[67] B. Johnson, J. Bauer, D. J. Niedermaier, W. Crone, and D. Beebe. Experimental techniques for mechanical characterization of hydrogels at the microscale. *Experimental mechanics*, 44(1):21–28, 2004.

[68] J. Jorgen Bergström and M. C. Boyce. Constitutive modeling of the large strain time-dependent behavior of elastomers. *Journal of the Mechanics and Physics of Solids*, 46(5):931–954, 1998.

[69] S. Juodkazis, N. Mukai, R. Wakaki, A. Yamaguchi, S. Matsuo, and H. Misawa. Reversible phase transitions in polymer gels induced by radiation forces. *Nature*, 408(6809):178–181, 2000.

[70] Z. S. Kean, J. L. Hawk, S. Lin, X. Zhao, R. P. Sijbesma, and S. L. Craig. Increasing the maximum achievable strain of a covalent polymer gel through the addition of mechanically invisible cross-links. *Advanced Materials*, 26(34):6013–6018, 2014.

[71] C. Keplinger, J.-Y. Sun, C. C. Foo, P. Rothemund, G. M. Whitesides, and Z. Suo. Stretchable, transparent, ionic conductors. *Science*, 341(6149):984–987, 2013.

[72] B. Keshavarz, T. Divoux, S. Manneville, and G. H. McKinley. Nonlinear viscoelasticity and generalized failure criterion for polymer gels. *ACS Macro Letters*, 6(7):663–667, 2017.

[73] A. S. Khan and O. Lopez-Pamies. Time and temperature dependent response and relaxation of a soft polymer. *International Journal of Plasticity*, 18(10):1359–1372, 2002.

[74] A. S. Khan, O. Lopez-Pamies, and R. Kazmi. Thermo-mechanical large deformation response and constitutive modeling of viscoelastic polymers over a wide range of strain rates and temperatures. *International Journal of Plasticity*, 22(4):581–601, 2006.

[75] C.-C. Kim, H.-H. Lee, K. H. Oh, and J.-Y. Sun. Highly stretchable, transparent ionic touch panel. *Science*, 353(6300):682–687, 2016.

[76] M. Kleverlaan, R. H. van Noort, I. Jones, et al. Deployment of swelling elastomer packers in shell e&p. In *SPE/IADC Drilling Conference*. Society of Petroleum Engineers, 2005.

[77] D. Klinger and K. Landfester. Photo-sensitive pmma microgels: light-triggered swelling and degradation. *Soft Matter*, 7(4):1426–1440, 2011.

[78] O. Kuksenok and A. C. Balazs. Modeling the photoinduced reconfiguration and directed motion of polymer gels. *Advanced Functional Materials*, 23(36):4601–4610, 2013.

[79] K. Kumar, C. Knie, D. Bléger, M. A. Peletier, H. Friedrich, S. Hecht, D. J. Broer, M. G. Debije, and A. P. Schenning. A chaotic self-oscillating sunlight-driven polymer actuator. *Nature communications*, 7(1):1–8, 2016.

[80] C. K. Kuo and P. X. Ma. Ionically crosslinked alginate hydrogels as scaffolds for tissue engineering: Part 1. structure, gelation rate and mechanical properties. *Biomaterials*, 22(6):511–521, 2001.

[81] C. Li, A. Iscen, H. Sai, K. Sato, N. A. Sather, S. M. Chin, Z. Álvarez, L. C. Palmer, G. C. Schatz, and S. I. Stupp. Supramolecular–covalent hybrid polymers for light-activated mechanical actuation. *Nature materials*, 19(8):900–909, 2020.

[82] H. Li, G. Go, S. Y. Ko, J.-O. Park, and S. Park. Magnetic actuated ph-responsive hydrogel-based soft micro-robot for targeted drug delivery. *Smart Materials and Structures*, 25(2):027001, 2016.

[83] C. Linder, M. Tkachuk, and C. Miehe. A micromechanically motivated diffusion-based transient network model and its incorporation into finite rubber viscoelasticity. *Journal of the Mechanics and Physics of Solids*, 59(10):2134–2156, 2011.

[84] J. Liu, J. Nie, Y. Zhao, and Y. He. Preparation and properties of different photoresponsive hydrogels modulated with uv and visible light irradiation. *Journal of Photochemistry and Photobiology A: Chemistry*, 211(1):20–25, 2010.

[85] M. Liu, X. Zeng, C. Ma, H. Yi, Z. Ali, X. Mou, S. Li, Y. Deng, and N. He. Injectable hydrogels for cartilage and bone tissue engineering. *Bone research*, 5:17014, 2017.

[86] K. Loeffel and L. Anand. A chemo-thermo-mechanically coupled theory for elastic-viscoplastic deformation, diffusion, and volumetric swelling due to a chemical reaction. *International Journal of Plasticity*, 27(9):1409–1431, 2011.

[87] K. Loeffel, L. Anand, and Z. M. Gasem. On modeling the oxidation of high-temperature alloys. *Acta Materialia*, 61(2):399–424, 2013.

[88] K. N. Long, T. F. Scott, H. J. Qi, C. N. Bowman, and M. L. Dunn. Photomechanics of light-activated polymers. *Journal of the Mechanics and Physics of Solids*, 57(7):1103–1121, 2009.

[89] R. Long, H. J. Qi, and M. L. Dunn. Thermodynamics and mechanics of photochemically reacting polymers. *Journal of the Mechanics and Physics of Solids*, 61(11):2212–2239, 2013.

[90] A. Lucantonio, P. Nardinocchi, and L. Teresi. Transient analysis of swelling-induced large deformations in polymer gels. *Journal of the Mechanics and Physics of Solids*, 61(1):205–218, 2013.

[91] M. Lutolf and J. Hubbell. Synthetic biomaterials as instructive extracellular microenvironments for morphogenesis in tissue engineering. *Nature biotechnology*, 23(1):47, 2005.

[92] I. A. Marozas, J. J. Cooper-White, and K. S. Anseth. Photo-induced viscoelasticity in cytocompatible hydrogel substrates. *New Journal of Physics*, 21(4):045004, 2019.

[93] C. Miehe and S. Göktepe. A micro–macro approach to rubber-like materials. part ii: The micro-sphere model of finite rubber viscoelasticity. *Journal of the Mechanics and Physics of Solids*, 53(10):2231–2258, 2005.

[94] S. Nam, K. H. Hu, M. J. Butte, and O. Chaudhuri. Strain-enhanced stress relaxation impacts nonlinear elasticity in collagen gels. *Proceedings of the National Academy of Sciences*, 113(20):5492–5497, 2016.

[95] P. Nardinocchi, M. Pezzulla, and L. Teresi. Anisotropic swelling of thin gel sheets. *Soft matter*, 11(8):1492–1499, 2015.

[96] P. Nardinocchi and L. Teresi. Actuation performances of anisotropic gels. *Journal of Applied Physics*, 120(21):215107, 2016.

[97] T. Nguyen, R. Jones, and B. Boyce. A nonlinear anisotropic viscoelastic model for the tensile behavior of the corneal stroma. *Journal of biomechanical engineering*, 130(4):041020, 2008.

[98] T. D. Nguyen, R. Jones, and B. Boyce. Modeling the anisotropic finite-deformation viscoelastic behavior of soft fiber-reinforced composites. *International Journal of Solids and Structures*, 44(25-26):8366–8389, 2007.

[99] T. D. Nguyen, H. J. Qi, F. Castro, and K. N. Long. A thermoviscoelastic model for amorphous shape memory polymers: incorporating structural and stress relaxation. *Journal of the Mechanics and Physics of Solids*, 56(9):2792–2814, 2008.

[100] D. Okumura, A. Kondo, and N. Ohno. Using two scaling exponents to describe the mechanical properties of swollen elastomers. *Journal of the Mechanics and Physics of Solids*, 90:61–76, 2016.

[101] Y. Osada and D. E. De Rossi. *Polymer sensors and actuators*. Springer Science & Business Media, 2013.

[102] G. Oster and N.-L. Yang. Photopolymerization of vinyl monomers. *Chemical Reviews*, 68(2):125–151, 1968.

[103] M. Otake, Y. Kagami, M. Inaba, and H. Inoue. Motion design of a starfish-shaped gel robot made of electro-active polymer gel. *Robotics and Autonomous Systems*, 40(2-3):185–191, 2002.

[104] Y. Pan and Z. Zhong. A nonlinear constitutive model of unidirectional natural fiber reinforced composites considering moisture absorption. *Journal of the Mechanics and Physics of Solids*, 69:132–142, 2014.

[105] Y. Partom and I. Schanin. Modeling nonlinear viscoelastic response. *Polymer Engineering & Science*, 23(15):849–859, 1983.

[106] J. K. Pijanka, B. Coudrillier, K. Ziegler, T. Sorensen, K. M. Meek, T. D. Nguyen, H. A. Quigley, and C. Boote. Quantitative mapping of collagen fiber orientation in non-glaucoma and glaucoma posterior human sclerae. *Investigative ophthalmology & visual science*, 53(9):5258–5270, 2012.

[107] D. J. Plazek. Temperature dependence of the viscoelastic behavior of polystyrene. *The Journal of Physical Chemistry*, 69(10):3480–3487, 1965.

[108] D. J. Plazek. The temperature dependence of the viscoelastic behavior of poly (vinyl acetate). *Polymer Journal*, 12(1):43, 1980.

[109] W. Rasband. *ImageJ*. U. S. National Institutes of Health, Bethesda, MD, 1997-2018.

[110] S. Reese. A micromechanically motivated material model for the thermo-viscoelastic material behaviour of rubber-like polymers. *International Journal of Plasticity*, 19(7):909–940, 2003.

[111] S. Reese and S. Govindjee. A theory of finite viscoelasticity and numerical aspects. *International journal of solids and structures*, 35(26-27):3455–3482, 1998.

[112] A. Rivaton and J. Gardette. Photodegradation of polyethersulfone and polysulfone. *Polymer degradation and stability*, 66(3):385–403, 1999.

[113] R. Rizzieri, F. Baker, and A. Donald. A study of the large strain deformation and failure behaviour of mixed biopolymer gels via in situ esem. *Polymer*, 44(19):5927–5935, 2003.

[114] K. Ronaldson-Bouchard, S. P. Ma, K. Yeager, T. Chen, L. Song, D. Sirabella, K. Morikawa, D. Teles, M. Yazawa, and G. Vunjak-Novakovic. Advanced maturation of human cardiac tissue grown from pluripotent stem cells. *Nature*, 556(7700):239, 2018.

[115] J. Ruchmann, S. Fouilloux, and C. Tribet. Light-responsive hydrophobic association of surfactants with azobenzene-modified polymers. *Soft Matter*, 4(10):2098–2108, 2008.

[116] J. Ryu, M. D'Amato, X. Cui, K. N. Long, H. Jerry Qi, and M. L. Dunn. Photo-origami — bending and folding polymers with light. *Applied Physics Letters*, 100(16):161908, 2012.

[117] T. Sain, K. Loeffel, and S. Chester. A thermo–chemo–mechanically coupled constitutive model for curing of glassy polymers. *Journal of the Mechanics and Physics of Solids*, 116:267–289, 2018.

[118] T. Sakai, H. Murayama, S. Nagano, Y. Takeoka, M. Kidowaki, K. Ito, and T. Seki. Photoresponsive slide-ring gel. *Advanced Materials*, 19(15):2023–2025, 2007.

[119] S. Schimka, N. Lomadze, M. Rabe, A. Kopyshev, M. Lehmann, R. von Klitzing, A. M. Rumyantsev, E. Y. Kramarenko, and S. Santer. Photosensitive microgels containing azobenzene surfactants of different charges. *Physical Chemistry Chemical Physics*, 19(1):108–117, 2017.

[120] R. D. Scurlock, B. Wang, P. R. Ogilby, J. R. Sheats, and R. L. Clough. Singlet oxygen as a reactive intermediate in the photodegradation of an electroluminescent polymer. *Journal of the American Chemical Society*, 117(41):10194–10202, 1995.

[121] T. Seki, M. Sakuragi, Y. Kawanishi, T. Tamaki, R. Fukuda, K. Ichimura, and Y. Suzuki. " command surfaces" of langmuir-blodgett films. photoregulations of liquid crystal alignment by molecularly tailored surface azobenzene layers. *Langmuir*, 9(1):211–218, 1993.

[122] J. Smart and J. Williams. A comparison of single-integral non-linear viscoelasticity theories. *Journal of the Mechanics and Physics of Solids*, 20(5):313–324, 1972.

[123] S. Sugiura, K. Sumaru, K. Ohi, K. Hiroki, T. Takagi, and T. Kanamori. Photoresponsive polymer gel microvalves controlled by local light irradiation. *Sensors and Actuators A: Physical*, 140(2):176–184, 2007.

[124] K. Sumaru, K. Ohi, T. Takagi, T. Kanamori, and T. Shinbo. Photoresponsive properties of poly (n-isopropylacrylamide) hydrogel partly modified with spirobenzopyran. *Langmuir*, 22(9):4353–4356, 2006.

[125] Y. Takashima, S. Hatanaka, M. Otsubo, M. Nakahata, T. Kakuta, A. Hashidzume, H. Yamaguchi, and A. Harada. Expansion–contraction of photoresponsive artificial muscle regulated by host–guest interactions. *Nature communications*, 3(1):1–8, 2012.

[126] T. Tanaka and D. J. Fillmore. Kinetics of swelling of gels. *The Journal of Chemical Physics*, 70(3):1214–1218, 1979.

[127] W. Toh, T. Y. Ng, J. Hu, and Z. Liu. Mechanics of inhomogeneous large deformation of photo-thermal sensitive hydrogels. *International Journal of Solids and Structures*, 51(25-26):4440–4451, 2014.

[128] H. H. Tønnesen and J. Karlsen. Alginate in drug delivery systems. *Drug development and industrial pharmacy*, 28(6):621–630, 2002.

[129] K. Urayama, K. Yokoyama, and S. Kohjiya. Viscoelastic relaxation of guest linear poly (dimethylsiloxane) in end-linked poly (dimethylsiloxane) networks. *Macromolecules*, 34(13):4513–4518, 2001.

[130] K. Valanis. Thermodynamics of large viscoelastic deformations. *Journal of Mathematics and Physics*, 45(1-4):197–212, 1966.

[131] A. Vinogradov and F. Holloway. Electro-mechanical properties of the piezoelectric polymer pvdf. *Ferroelectrics*, 226(1):169–181, 1999.

[132] D. Wang and S. Wu. Red-light-responsive supramolecular valves for photocontrolled drug release from mesoporous nanoparticles. *Langmuir*, 32(2):632–636, 2016.

[133] S. Wang, M. Decker, D. L. Henann, and S. A. Chester. Modeling of dielectric viscoelastomers with application to electromechanical instabilities. *Journal of the Mechanics and Physics of Solids*, 95:213–229, 2016.

[134] X. Wang and W. Hong. A visco-poroelastic theory for polymeric gels. *Proceedings of the Royal Society A: Mathematical, Physical and Engineering Sciences*, 468(2148):3824–3841, 2012.

[135] R. E. Webber, C. Creton, H. R. Brown, and J. P. Gong. Large strain hysteresis and mullins effect of tough double-network hydrogels. *Macromolecules*, 40(8):2919–2927, 2007.

[136] M. Wehner, R. L. Truby, D. J. Fitzgerald, B. Mosadegh, G. M. Whitesides, J. A. Lewis, and R. J. Wood. An integrated design and fabrication strategy for entirely soft, autonomous robots. *Nature*, 536(7617):451, 2016.

[137] J. A. Weiss, B. N. Maker, and S. Govindjee. Finite element implementation of incompressible, transversely isotropic hyperelasticity. *Computer methods in applied mechanics and engineering*, 135(1-2):107–128, 1996.

[138] M. L. Williams, R. F. Landel, and J. D. Ferry. The temperature dependence of relaxation mechanisms in amorphous polymers and other glass-forming liquids. *Journal of the American Chemical society*, 77(14):3701–3707, 1955.

[139] S. Woerly, V. D. Doan, F. Evans-Martin, C. G. Paramore, and J. D. Peduzzi. Spinal cord reconstruction using neurogel™ implants and functional recovery after chronic injury. *Journal of neuroscience research*, 66(6):1187–1197, 2001.

[140] J. Xie, J. B. McGovern, R. Patel, W. Kim, S. Dutt, and A. D. Mazzeo. Elastomeric actuators on airfoils for aerodynamic control of lift and drag. *Advanced Engineering Materials*, 17(7):951–960, 2015.

[141] B. Yohsuke, K. Urayama, T. Takigawa, and K. Ito. Biaxial strain testing of extremely soft polymer gels. *Soft Matter*, 7(6):2632–2638, 2011.

[142] A. York, J. Dunn, and S. Seelecke. Experimental characterization of the hysteretic and rate-dependent electromechanical behavior of dielectric electro-active polymer actuators. *Smart Materials and Structures*, 19(9):094014, 2010.

[143] E. Yousif and R. Haddad. Photodegradation and photostabilization of polymers, especially polystyrene. *SpringerPlus*, 2(1):398, 2013.

[144] V. Zamani and T. J. Pence. Swelling, inflation, and a swelling-burst instability in hyperelastic spherical shells. *International Journal of Solids and Structures*, 125:134–149, 2017.

[145] S. Zhang, J. Ermann, M. D. Succi, A. Zhou, M. J. Hamilton, B. Cao, J. R. Korzenik, J. N. Glickman, P. K. Vemula, L. H. Glimcher, et al. An inflammation-targeting hydrogel for local drug delivery in inflammatory bowel disease. *Science translational medicine*, 7(300):300ra128–300ra128, 2015.

[146] X. Zhao, N. Huebsch, D. J. Mooney, and Z. Suo. Stress-relaxation behavior in gels with ionic and covalent crosslinks. *Journal of applied physics*, 107(6):063509, 2010.

[147] W. J. Zheng, N. An, J. H. Yang, J. Zhou, and Y. M. Chen. Tough al-alginate/poly (n-isopropylacrylamide) hydrogel with tunable lcst for soft robotics. *ACS applied materials & interfaces*, 7(3):1758–1764, 2015.